



The
University
Of
Sheffield.

Numerical study of MEMS-Based vaporizing liquid microthruster for CubeSats

Abdulla Alnajim

Supervisors: Dr. Andrew Nowakowski and Prof. Yang Zhang

A thesis submitted in partial fulfilment of the requirements for the degree
of Doctor of Philosophy

The University of Sheffield
Department of Mechanical Engineering

October 2021

Declaration

I, the author, confirm that the Thesis is my work. I am aware of the University's Guidance on the Use of Unfair Means (www.sheffield.ac.uk/ssid/unfair-means). This work has not previously been presented for an award at this or any other university.

Name:

Abdulla Mohammed Alnajim

Signature:



Date:

26 October 2021

ABSTRACT

In the last decade, the interest in CubeSat had been increased dramatically. The low deployment cost and the capability to operate in low Earth orbit enable it to become one of the most attractive tools for different space missions such as remote sensing and communications. However, the information about the technology of the CubeSat in terms of the design and the propulsion system is still limited or characterized as classified data. The focus of this work is mainly on the enhancement of the performance of the vaporizing liquid microthruster (VLM) propulsion system of a CubeSat.

The development in propulsion systems' miniaturization has generated a proliferation entailing both nano- and microsatellite designs. Consequently, the microelectromechanical systems (MEMS) technology has diversified into various applications. Recently, MEMS have been applied in the domain of micropropulsion for miniaturized satellites. The VLM is amongst several MEMS microthrusters which is established newly, has gained research attention for its capability to produce continuously variable thrust in the micronewton (μN) to millinewton (mN) range.

In this thesis, 3D model simulations were conducted to numerically investigate the fluid flow behaviour of MEMS-VLM thruster with the aid of the Computational Fluid Dynamics (CFD) technique. The computational domain consists of an inlet channel, distributor, microchannels, chamber and in-plane converging-diverging (C-D) nozzle. The geometry's modification aims to achieve maximum thrust force by controlling the VLM chamber heating power at a constant inlet propellant flow rate. The computational simulations of the proposed design were performed for two phases: subsonic section (inlet-distributor-microchannel-chamber) and supersonic section (planar convergent-divergent micronozzle). The numerical results demonstrate a 38% increase in the thrust force and 22% decrease in the heating power compared to the design proposed by Kundu et al. [Pijus Kundu et al. 2012 J. Micromech. Microeng. 22 025016].

In conclusion, the geometrical modification remarkably increases the underlying

thrust with comparatively low input power. The proposed VLM modification can yield up to 1.38 mN thrust and a specific impulse of 70 s by utilizing 2 W heating power at a $2mg.s^{-1}$ water flow rate, which is within the capability of the CubeSat power budget and fuel amount. Moreover, the current design could reduce the possibility of propellant pumps failure that resulted from the boiling of the water within the inlet part of the VLM, and hence reduce the thrust instability. Finally, a comparative evaluation with other published VLM research shows that the current design can produce relatively more thrust force by utilizing less input power.

ACKNOWLEDGEMENT

I want to express my most profound appreciation to my superior, Dr Andrew Nowakowski, who has the personality and substance of a genius. He has consistently expressed a sense of adventure in the study and scholarship and a passion for teaching. This dissertation would not have been practicable without his professional advice, continuous encouragement and close oversight. Also, I would like to thank Dr Yang Zhang (my second supervisor) for his encouragement and support during this study and work. I want to express my gratitude and appreciation for H.H.Dr. Turki Bin Saud Bin Mohammed Al Saud, whose encouragement has been invaluable throughout my study. I am also grateful to Dr Yaser H. Alahmadi for his valuable discussions. I am particularly grateful for the assistance given by my family and colleagues for their cooperation and encouragement, which helped me throughout my research. Finally, special thanks to the University of Sheffield for offering me a place at the university.

Nomenclature

A_e	Exit area (m^2)
A_r	Argon
A_t	Throat area (m^2)
C_p	Heat capacity at constant pressure (J/K)
C_v	Heat capacity at constant volume (J/K)
F	Thrust (mN)
g_0	The standard gravitational acceleration ($m.s^2$)
H_v	Water vapor enthalpy (J/mol)
H_l	Liquid water enthalpy (J/mol)
H_e	Helium
H_2	Hydrogen
I	Impulse bit (mN.s)
I_{sp}	Specific impulse (s)
k	Thermal conductivity (W/mK)
Kn	Knudsen number
M_{prop}	Molar mass of the propellant
M_e	Flow rate ($kg.s^{-1}$)
mN	Millinewton

\dot{m}	Mass flow rate ($mg.s^{-1}$)
P_a	Ambient pressure (Pa)
P_c	Chamber pressure (Pa)
P_e	Exit pressure (Pa)
P	Static pressure (Pa)
Q	The power (W)
Q_{el}	The electrical power consumption (W)
Q_{evap}	The power consumed to evaporate the flow (W)
$Q_{\Delta T}$	The energy added to increase the flow temperature every second (W)
R	Gas constant (kJ/kg.K)
Re	Throat Reynolds number
R_t	Throat radius (m)
T	Temperature (K)
T	Static temperature (K)
T_e	Exit temperature (K)
T_c	Chamber temperature (K)

Abbreviations

AC	Alternating current
CGM	Cold gas microthruster
C-D	Conversion-diversion
CFD	Computational fluid dynamics
DSMC	Direct Simulation Monte-Carlo
FMMR	Free molecule microresistojets
HTCC	High-temperature co-fired ceramic
HPC	High-performance computing
IAPWS	International association for the properties of water and steam
JPL	Jet propulsion laboratory
LPM	Low-pressure microresistojet
LTCC	Low-Temperature co-fired ceramic
LP	Liquid propellant
MEMS	Microelectromechanical systems
MET	Microwave electrothermal thrusters
PCB	Printed circuit board
PPT	Micropulse plasma thrusters
PTFE	Poly-tetrafluoro ethylene

RF	Radio frequency
RFET	Radio frequency electrothermal thrusters
SFL	Space Flight Laboratory
SPM	Solid propellant microthruster
SCCM	Standard cubic centimeter per minute
SCCS	Standard cubic centimetres per second
SSCS	Standard cubic centimetres per minute
SST	Shear stress transport
Ti	Titanium
U	Units
UTIAS	University of Toronto Institute for Aerospace Studies
VLM	Vaporizing liquid microthruster

Greek Symbols

γ	Specific heat ratio of the propellant
λ	Molecular mean free path
Γ	The Vandekerckhove function
ρ	Fluid density (kg/m^3)
η	Efficiency
μN	Micronewton

v_l	Limit exhaust velocity ($m.s^{-1}$)
v_e	Exit vapour velocity ($m.s^{-1}$)
v_e	Exhaust velocity ($m.s^{-1}$)
$\eta_{F.P}$	The thrust efficiency
η_{el}	The electrical efficiency
η_{th}	The thermal efficiency

Subscripts

e	Exit
g	Gas
l	Liquid
n	Nozzle
t	Throat
w	Wall

Contents

Contents	x
List of Figures	xiv
List of Tables	xxi
1 Introduction	1
1.1 Background	1
1.2 Aims and Objectives	3
2 Literature Review	5
2.1 CubeSat Requirements for Propulsion System	5
2.2 Propulsion Requirements for CubeSat Missions	6
2.3 Types of MEMS Microthruster	7
2.3.1 Chemical MEMS Microthruster	8
2.3.1.1 Solid Propellant Microthruster (SPM)	8
2.3.1.2 Liquid Propellant Microthruster (LP)	9

2.3.2	Cold Gas Microthrusters (CGM)	10
2.3.3	Electric MEMS Microthruster	12
2.3.3.1	Plasma Microthruster	13
2.3.3.2	Colloid Microthruster	15
2.3.3.3	Electrospray Microthruster	16
2.3.3.4	Resistojets Microthruster	17
3	The Vaporizing Liquid Microthruster (VLM)	29
3.1	Concept of Vaporizing Liquid Microthruster	29
3.2	Performance of Vaporizing Liquid Microthruster	33
3.3	Description of VLM Design	36
3.4	VLM Physical Processes	40
3.5	VLM Optimization Technique	41
3.5.1	Supersonic Region (Convergent-Divergent Nozzle)	41
3.5.2	Subsonic Region (Inlet-Distributor-Microchannels-Chamber)	42
3.6	Computational Fluid Dynamics Methods of Flows Simulation	43
3.6.1	CFD Models	43
3.6.1.1	Single-Phase Supersonic Models	43
3.6.1.2	Multi-Phase Subsonic Models	44
3.6.2	CFD Codes	44

3.6.3	Computational Resources	45
4	Numerical Implementation and Simulation Setup	46
4.1	Methodology of the VLM Simulation	46
4.2	Supersonic Region Simulation	46
4.2.1	Governing Equations	46
4.2.2	Modification of the Geometry of the VLM Supersonic Region	50
4.2.3	Mesh of the VLM Supersonic Region	51
4.2.4	CFD Model Setup of the VLM Supersonic Region	52
4.3	Subsonic Region Simulation	54
4.3.1	Governing Equations	54
4.3.2	Modification of the Geometry of the VLM Subsonic Region	56
4.3.3	Mesh of the VLM Subsonic Region	59
4.3.4	CFD model Setup of the VLM Subsonic Region	61
5	Results and Discussions	63
5.1	Results of the VLM Supersonic Region Simulation	63
5.2	Analyzing of the VLM Supersonic Region Simulation	75
5.3	Results of the VLM Subsonic Region Simulation	76
5.4	Analyzing of the VLM Subsonic Region Simulation	84
5.5	Comparison of the Various Microthruster Parameters with Optimized VLM	86

6	Conclusion and Future Work	88
7	Appendix A (More Simulation Results of the VLM Supersonic Region)	100
8	Appendix B (More Simulation Results of the VLM Subsonic Region)	117

List of Figures

- 1.1 CubeSat [1]. 1
- 1.2 Global Nanosatellite and Microsatellite Market, by regions, 2020 to 2027 [2]. 2
- 2.1 Types of MEMS microthruster. 7
- 2.2 An example of a solid microthruster propellant [3]. 8
- 2.3 Schematic view of (a) planar and (b) vertical design of the thruster [4]. . . 9
- 2.4 An example of liquid propellant microthruster [4]. 10
- 2.5 Example of cold gas microthruster [5]. 11
- 2.6 Microwave electrothermal thrusters (MET) schematic diagram [6]. 14
- 2.7 Schematic of the Coaxial Pulsed Plasma Microthruster [7]. 15
- 2.8 Colloid Microthruster Schematic Diagram designed by Xiong [8]. 16
- 2.9 Schematic of an electrospray microthruster [9]. 17
- 2.10 VLM system showing: (1) a tank; (2) a solenoid valve; (3) a thruster;
 m_1, m_2, m_3 are the mass flow rate [10]. 18

2.11	The cross section of the LPM indicates the parts of the thruster; the flow is in the direction indicated by the red arrow [10].	19
2.12	JPL Vaporizing Liquid Microthruster (VLM)[11].	20
2.13	Comparison between two different designs: In-plane design of thrust (left) and out-of-plane design of thrust (right) [4].	21
2.14	Schematic view of an internal microheater vaporizing liquid microthruster (VLM) modeled by [12].	23
2.15	Cross-sectional view of the VLM [13].	23
2.16	A diagram of two microthrusters. (a) the side exit of the nozzle and (b) the top exit of the nozzle [4].	24
2.17	The VLM chip consists of a Pyrex glass and a silicon: (a) The cross-section of one channel, (b) the picture of the VLM with an outlet width of 1000 μm [14].	25
2.18	3D schematic view of the complete MEMS-VLM microthruster sandwiched between top and bottom microheaters [4].	26
2.19	Thrust estimation configuration diagram using a semi-microbalance [15].	26
2.20	Schematic overview of the various designs for each section of the VLM [16].	27
2.21	Schematic of the work process of the VLM [17].	28
3.1	Illustration of the resistojet concept [18].	29
3.2	Sketch of the VLM.	36
4.1	Top and side view image of the original CAD model of supersonic nozzle (V1).	51

4.2	Lateral view of mesh fragment of supersonic region.	52
4.3	Boundary conditions for simulation of supersonic part of VLM.	53
4.4	First concept model of the VLM subsonic region.	56
4.5	Second concept model of the VLM subsonic region.	57
4.6	Third concept model of the VLM subsonic region.	57
4.7	Forth concept model of the VLM subsonic region.	58
4.8	Top and side view of schematic diagram of the optimized VLM thruster (dimension in mm).	59
4.9	Top view of mesh fragment of subsonic region at the inlet.	60
4.10	Top view of mesh fragment of subsonic region at microchannels outlet.	60
4.11	Lateral view of mesh fragment of subsonic region at nozzle exit.	60
4.12	Boundary conditions locations for subsonic simulation.	61
5.1	Top view image of 1st modification model of supersonic nozzle (V2).	63
5.2	Top view image of 2nd modification model of supersonic nozzle (V3).	64
5.3	Top view image of 3rd modification model of supersonic nozzle (V4).	64
5.4	Top view image of 4th modification model of supersonic nozzle (V5).	65
5.5	Top view image of 5th modification model of supersonic nozzle (V6).	65
5.6	Top view image of 6th modification model of supersonic nozzle (V7).	66
5.7	Top view image of 7th modification model of supersonic nozzle (V8).	66

5.8	Top view image of 8th modification model of supersonic nozzle (V9).	67
5.9	Top view image of 9th modification model of supersonic nozzle (V10).	67
5.10	Top view image of 10th modification model, the most optimal geometry of supersonic nozzle (V11).	68
5.11	Absolute pressure distribution into thruster of supersonic model.	71
5.12	Absolute pressure distribution along thruster x-axis.	71
5.13	Total pressure distribution into thruster of supersonic model.	72
5.14	Fluid velocity distribution into thruster of supersonic model.	72
5.15	Fluid Mach number distribution into thruster of supersonic model.	73
5.16	Mach number along nozzle x-axis.	73
5.17	Temperature distribution into thruster of supersonic model.	74
5.18	Density distribution into thruster of supersonic model.	74
5.19	Thruster, steam volume fraction of subsonic model.	78
5.20	Steam volume fraction into thruster of subsonic model.	79
5.21	Steam volume fraction, zoom-in into the middle of microchannel region.	79
5.22	Steam volume fraction, into the chamber region.	80
5.23	Chamber outlet area, averaged steam volume fraction	80
5.24	Total pressure distribution into thruster of subsonic model.	81
5.25	Thruster, inlet and outlet average total pressure.	81
5.26	Absolute pressure distribution into thruster of subsonic model.	82

5.27	Velocity distribution into thruster of subsonic model.	82
5.28	Silicon temperature of subsonic model.	83
5.29	Water temperature distribution into thruster of subsonic model.	83
7.1	Geometry code V1, a. Mach number; b. absolute pressure; c. total pressure; d, temperature; e. density; f. velocity.	104
7.2	Geometry code V2, a. Mach number; b. absolute pressure; c. total pressure; d, temperature; e. density; f. velocity.	105
7.3	Geometry code V3, a. Mach number; b. absolute pressure; c. total pressure; d, temperature; e. density; f. velocity.	106
7.4	Geometry code V4, a. Mach number; b. absolute pressure; c. total pressure; d, temperature; e. density; f. velocity.	107
7.5	Geometry code V5, a. Mach number; b. absolute pressure; c. total pressure; d, temperature; e. density; f. velocity.	108
7.6	Geometry code V6, a. Mach number; b. absolute pressure; c. total pressure; d, temperature; e. density; f. velocity.	109
7.7	Geometry code V7, a. Mach number; b. absolute pressure; c. total pressure; d, temperature; e. density; f. velocity.	110
7.8	Geometry code V8, a. Mach number; b. absolute pressure; c. total pressure; d, temperature; e. density; f. velocity.	111
7.9	Geometry code V9, a. Mach number; b. absolute pressure; c. total pressure; d, temperature; e. density; f. velocity.	112
7.10	Geometry code V10, a. Mach number; b. absolute pressure; c. total pressure; d, temperature; e. density; f. velocity.	113

7.11	Geometry code V11, a. Mach number; b. absolute pressure; c. total pressure; d, temperature; e. density; f. velocity.	114
7.12	Geometry code V11.1, a. Mach number; b. absolute pressure; c. total pressure; d, temperature; e. density; f. velocity.	115
7.13	Geometry code V12, a. Mach number; b. absolute pressure; c. total pressure; d, temperature; e. density; f. velocity.	116
8.1	Absolute pressure distribution into thruster.	118
8.2	Total pressure distribution into thruster.	118
8.3	Steam temperature distribution into thruster.	119
8.4	Steam volume fraction into thruster.	119
8.5	Steam volume fraction, into chamber region.	120
8.6	Steam volume fraction Zoom in, into the middle of microchannel region.	120
8.7	Water volume fraction distribution into thruster.	121
8.8	Water temperature distribution into thruster.	121
8.9	Steam velocity distribution into thruster.	122
8.10	Silicon temperature distribution into thruster.	122
8.11	Total pressure distribution into thruster.	123
8.12	Steam volume fraction into thruster.	124
8.13	Zoom in of Steam volume fraction into middle of microchannels region.	124
8.14	Steam volume fraction into the chamber region.	125

8.15	Water volume fraction distribution into the thruster.	125
8.16	Water temperature distribution into thruster.	126
8.17	Steam velocity distribution into thruster.	126
8.18	Silicon temperature distribution into thruster.	127

List of Tables

- 2.1 Requirements of propulsion for nanosatellites for an extended range of missions [19]. 6

- 4.1 The geometrical dimensions of the thruster subsonic region. 59

- 5.1 The VLM supersonic regions geometrical dimensions. 69
- 5.2 Numerical data of the nozzle simulation. 70
- 5.3 Numerical data of the nozzle simulation at chamber inlet. 70
- 5.4 Numerical data of the nozzle simulation at nozzle outlet. 70
- 5.5 Numerical data of the VLM subsonic model simulation at heat power 2 W. 78
- 5.6 Comparison of the various microthruster parameters. 87

- 7.1 Numerical data of the nozzle simulation. 101
- 7.2 Numerical data of the nozzle simulation at chamber inlet. 102
- 7.3 Numerical data of the nozzle simulation at nozzle outlet. 103

- 8.1 Numerical data of the VLM subsonic model simulation at heat power 2.3 W. 117

8.2 Numerical data of the VLM subsonic model simulation at heat power 3.6 W.123

1 Introduction

1.1 Background

The miniaturized CubeSats constitutes an interesting scientific research subject in many research institutions around the world. Miniature space technologies, such as CubeSats shown in Figure 1.1 below, are revolutionizing space exploration by offering cheap and reliable spacecraft [20]. CubeSats have standard dimensions of 10 cm x 10 cm x 10 cm (Unit or "U"). They are available in sizes of 1U, 2U, 3U, and 6U, and normally weight less than 1.33 kg (3 lbs) per U. Growing interest in microsatellites, as shown in Figure 1.2 below, presents the need for CubeSats to have a functional propulsion system to help in controlling the attitude, drag compensation, orbit adjustment, station keeping, and maintenance of the devices. Micropropulsion systems with the capacity to deliver impulse bits in the range of $10 \times 10^{-6} \text{ N s}$ and a few micro-millinewtons of thrust would be sufficient for such small devices [21]. Given their small size and mass, such micropropulsion systems can be essential for microspacecraft attitude control [22].



Figure 1.1: CubeSat [1].

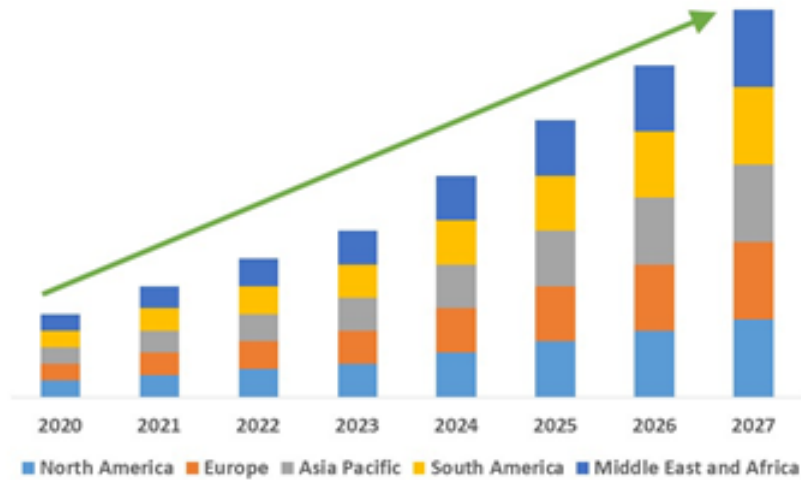


Figure 1.2: Global Nanosatellite and Microsatellite Market, by regions, 2020 to 2027 [2].

Notably, microelectromechanical systems (MEMS) technology is crucial in the development of micropropulsion systems. MEMS technology uses silicon-based fabrications to make machine systems. The term MEMS is sometimes used to refer to any microfabrication [23], such as the high aspect ratio micromachining, which replaces the silicon with structural components of electrochemical and mechanical systems. This technology enables the fabrication of micron-sized devices into precise shapes [24]. Accordingly, the technology is suitable for the fabrication of miniature, lightweight systems needed on the CubeSats.

Since knowledge of developing microthrusters continues to evolve, experts can explore the potential of MEMS technology in this area. In the same regard, this thesis examines some of the designs, performance, and innovations available in the use of MEMS technology to develop microthrusters, such as Free Molecule Microresistojets (FMMR), electrospray microthrusters, cold gas microthruster (CGM), colloid microthrusters, and plasma microthrusters, which will be briefly introduced in this present work.

This study seeks to establish modelling concepts for developing a propulsion system that would enable micro spacecraft to manoeuvre, attitude and position control. A

feasible alternative for the CubeSats is the Vaporizing Liquid Microthruster (VLM). The working principle of the VLM involves the use of resistance-based heaters, which vaporize the propellant and project it through nozzles to propel a device in space. As such, this thruster is designed with a heating system attached to the device. The device consumes low quantities of power, yet it can propel a device at supersonic speeds. Hence it matches the qualities needed on a CubeSat device.

1.2 Aims and Objectives

Innovations to reduce the costs of executing space missions led to the development of CubeSats. Over the last 15 years, these devices have conducted several low Earth orbit missions for different purposes, i.e., space research and technology, Earth observation, and communication. At present, there are several research attempts aimed at improving these devices to perform interplanetary missions and fly to the Moon, Mars, and Jupiter. For example, NASA launched two MarCO CubeSats which became the first CubeSats to leave Earth orbit in May 2018, on their way to Mars. The small size of the CubeSat makes it a challenging task to design a micro-scale propulsion system. Various research groups proposed different propulsion systems that meet the requirements to run the CubeSat successfully. Nevertheless, the missions of the existing CubeSats are limited due to the low efficiency of the propulsion system. However, the emerging of the micro propulsion system such as (MEMS) offers promising potential for improvement in the next generations of the micro-spacecraft.

Since 2018, MEMS technology has grown noticeably, with diverse applications. The VLM is among the primary MEMS applications developed in the micropropulsion of miniaturized satellites. The MEMS-VLM accruing to small spacecraft is very interesting, following the substantial capability of yielding high thrust levels with minimal power consumption. Therefore, numerical simulation of supersonic VLM micro thruster flows is of great importance to understand the physical properties of the fluid flow and its

behaviour since experiments are complex at micro scales.

The aim of this thesis is twofold:

1) To numerically investigate the fluid flow behaviour inside the MEMS-VLM thruster proposed by Kundu et al. [15].

2) Enhancing the thrust stability and avoiding the boiling phenomena in the inlet section of the thruster, which improves the attitude precision control, compensates for drag and manoeuvre of the CubeSat in orbit.

In order to achieve this aim, the following approach has been followed:

1. A 3D model simulation will be conducted to numerically investigate the fluid flow behaviour of MEMS-VLM thruster using the computational fluid dynamics (CFD) technique.
2. The numerical simulation approach will be divided into two independent stages:
 - a) Multi-phase (water-steam) simulation for subsonic section (Inlet-Distributor-Microchannel-Chamber).
 - b) Single-phase simulation (steam) for supersonic section, in-plane (Convergent-Divergent nozzle).
3. The geometry design will be modified to increase the thruster performance, efficiency, stability and avoid propellant boiling in the inlet section of the thruster.
4. Optimized subsonic and supersonic geometry sections of the MEMS-VLM thruster will be docked to obtain the required amount of heat power that should be added to the liquid to produce the required thrust.

2 Literature Review

2.1 CubeSat Requirements for Propulsion System

Developing a CubeSat propulsion system is still in its early stages, making it an attractive scientific research topic in many research institutions worldwide. Although a few successful flights have been recorded so far, it primarily involves mechanical and electrical challenges. The Canadian Advanced Nanosatellite experiment-2 (CanX-2) was the first CubeSat to set off for a space mission which is equipped with a propulsion system [25]. The mission was coordinated by the Institute for Aerospace Studies-Space Flight Laboratory (UTIAS-SFL) at the University of Toronto. The CanX-2 was equipped with a Nanosatellite Propulsion System (NANOPS), consisting of a cold gas thrusters system powered with liquid fuel. The propellant used in this NANOPS was sulphur hexafluoride at high storage density to attain a mass of less than half a kilogram. The NANOPS was built to generate a thrust power between 50 and 100 mN with a specific impulse in the range of 500-1000 s; this produces a total velocity increment Δv of more than $35 \text{ m}\cdot\text{s}^{-1}$. However, during the formation flight mission, the propulsion system was set at a maximum thrust of 35 mN with a specific impulse averaging 46.7 s. The minimum impulse bit was in the range of 0.07 mNs and 0.15 mNs, which require a velocity increment Δv of $2 \text{ m}\cdot\text{s}^{-1}$. Other experts suggest a velocity increment of about $12.4 \text{ m}\cdot\text{s}^{-1}$ during the formation flight mission to produce a specific impulse of about 90 s [26]. The success of the CanX-2 in using the NANOPS to control attitude and manoeuvres made it the prototype on which other experiments would be scaled and advanced.

2.2 Propulsion Requirements for CubeSat Missions

Due to the different applications of the CubeSat, the propulsion system must operate in different situations to control and direct the CubeSat, allowing it to carry out various operations. A nanosatellite should potentially perform several manoeuvres, similar to conventional satellites, thus expanding its capabilities and applications. According to Perez *et al.* [19], it would be essential for the propulsion system to drive the CubeSats Δv range between 1 and 100 $m.s^{-1}$. Other suggestions of the propulsion system requirements are summarized in Table 2.1.

Table 2.1: Requirements of propulsion for nanosatellites for an extended range of missions [19].

Parameter description	Nanosatellite propulsion requirements
Thrust level range, mN	1 - 1000
Microthruster wet mass, kg	3
Microthruster power consumption, W	10
Microthruster volume, m^3	0.0008 - 0.009743
Microthruster lifetime, $years$	2 - 5
Number of microthruster per nanosatellite	1 - 12
Minimum impulse bit, mNs	0.1 - 100

Considering the small size of CubeSats, the major constraint for this propulsion system is the ability to store the propulsion resources on such a small device and deliver enough Δv for the mission flights. CubeSats that would require higher Δv and a lower thrust would need efficient electric propulsion to perform longer and more reliant orbital manoeuvres. Furthermore, some flight situations require impulsive orbital manoeuvres, which are well suited for chemical propulsion systems even though they produce lower Δv [19].

2.3 Types of MEMS Microthruster

Throughout this study, micropropulsion refers to any system capable of producing several micro or millinewtons of thrust that can facilitate the flight functions of a nanosatellite or a picosatellite as defined by its mass, size, and power. In the field of micropropulsion for micro-nano satellites, the microfabrication technology of MEMS has been successfully used. In the past few years, several forms of micropropulsion systems based on MEMS technology have been investigated. As shown in Figure 2.1 below, it is possible to loosely categorize the key microthrusters researched by several groups according to the driving method they adopted.

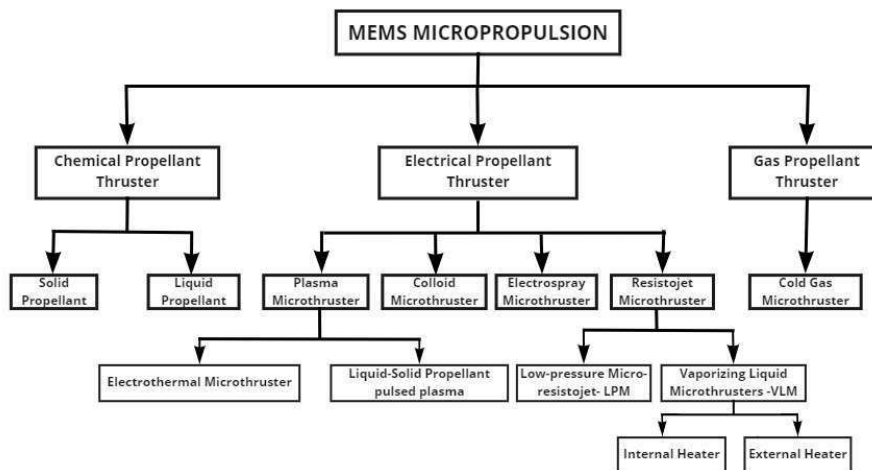


Figure 2.1: Types of MEMS microthruster.

These microthrusters types, which also reflect the promise of MEMS technology, are under constant development. A brief review of the current development status of the different microthrusters that can be produced using MEMS technologies is included in this study. Some types of microthrusters have received less investigation than others acquired from current studies, including cold gas microthruster, plasma microthruster, electrospray microthruster and colloid microthruster. Therefore, some microthrusters are added briefly with a representative structure.

2.3.1 Chemical MEMS Microthruster

The working principle of chemical propulsion systems depends on thermodynamics. Accordingly, these systems utilize the chemical energy in the propellants to power the accelerations and manoeuvres of the spacecraft. The power is used to eject a gaseous product of the propellant through a calibrated divergent or convergent nozzle to produce thrust. The dynamics of the chemical reaction, such as enthalpy and pressure, determine the amount of thrust produced in these systems. Evidently, chemical microthrusters have recorded the potential to execute attitude and orbital manoeuvres of low to moderate Δv , appropriate for a thrust-to-weight ratio of 0.1- 0.3 [27], which were traditionally applicable for satellite manoeuvres. However, there are ongoing concerns about safety, performance, scaling and control of temperature in their applications on nanosatellites. These systems use solid, liquid, and gaseous or mixtures of propellants.

2.3.1.1 Solid Propellant Microthruster (SPM)

The basic design prototypes for solid propellant thrusters have an ignition, combustion chamber and a nozzle, as highlighted in Figure 2.2 below. The system could be designed in a vertical or planer approach, as shown in Figure 2.3 below. As per Figure 2.3 (a), the geometry of the thruster consists of several wafers stacked in a vertical conformation. However, the planar design has all three components (combustion chamber, igniter, and nozzle) in one wafer as depicted in Figure 2.3 (b), which makes it possible to have different nozzle shapes in the desired thrusters using a single micromachining step.

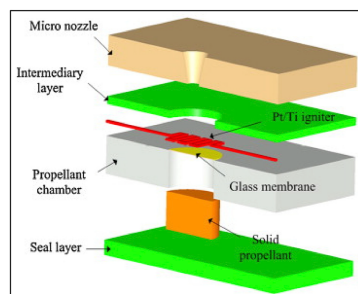


Figure 2.2: An example of a solid microthruster propellant [3].

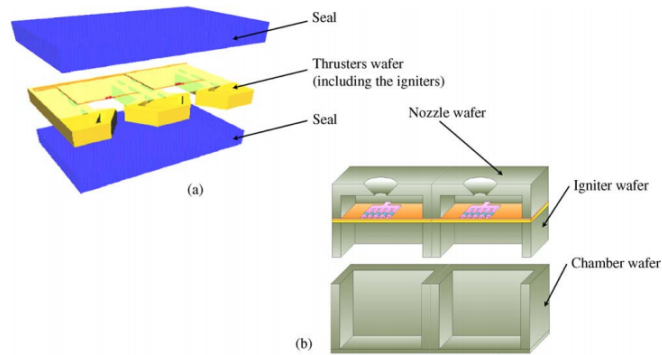


Figure 2.3: Schematic view of (a) planar and (b) vertical design of the thruster [4].

Nevertheless, when an array of thrusters is required, the vertical design is more appropriate. Conversely, the planar design would be more complicated since multiple lines of thrusters would need to be joined in stacks making 2D arrays. Furthermore, fitting the electronic components would be constrained by this dense system array. Hence, the vertical design is appropriate for a variety of thrusters.

2.3.1.2 Liquid Propellant Microthruster (LP)

Liquid propellant (LP) microthrusters use liquid propellants by implementing catalytic decomposition to produce hot gases from the fuels. The gases are forced through a nozzle to generate thrust. Primarily, gases such as hydrogen peroxide and hydrazine are preferred due to their ability to quickly decompose under a catalyst and produce hot gases. Nonetheless, alternatives, such as the use of bipropellants, store the fuel and oxidizer in separate chambers, but still following the same concept, are being considered [28]. As shown in Figure 2.4 below, the devices consist of an inlet region, a catalyst chamber and a nozzle.

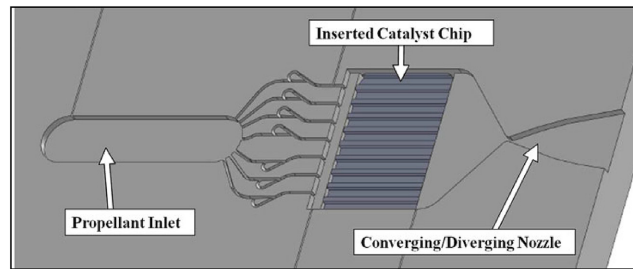


Figure 2.4: An example of liquid propellant microthruster [4].

Practically, large spacecraft have used hydrazine as an LP thruster to propel and control attitude since they can generate middle-level specific impulses. Nevertheless, this propellant presents the great design and handling challenges due to its high flammability and toxicity properties. Consequently, the cost of developing such a propulsion system on a CubeSat would be extremely high to address these underlying constraints [29].

However, hydrogen peroxide is a more feasible alternative since it requires fewer handling precautions [30], [31]. Nevertheless, it presents challenges in developing efficient catalytic systems. Currently, organic catalysts are the best alternatives for the decomposition of hydrogen peroxide, but they work slowly due to their minimized contact surface with other substances in the storage chamber. As a result, CubeSats with more extended delay missions would consume more fuel, thereby defining its inefficiencies. Further improvements are needed to find appropriate LP thrusters for nanosatellites.

The decomposition rate, which rises along with the temperature, will significantly impact the propulsion system's performance against the expected performance. Furthermore, when in contact with a catalyst bed, the high temperature created by the decomposition of the propellants causes thermal control problems for nanosatellites [27].

2.3.2 Cold Gas Microthrusters (CGM)

Cold gas micropropulsion is based on the controlled ejection of a pressured gas, which can be stored in gas, liquid, or solid phase, via a nozzle at a high enough velocity to

generate thrust. It is one of the simplest propulsion systems since it primarily consists of a propellant storage tank and nozzle. This simplicity reduces the power needs of the thrusters and enables miniaturizing.

It is feasible to scale down these systems and create a micropropulsion device for a CubeSat. Figure 2.5 presents one of the cold gas micropropellant prototypes suitable for a CubeSat; its development and operations appear simple. This prototype has an integrated circuit to communicate with the satellite bus interface, yet it is packed to fit sizes of 1U, and lower [32], [33]. Accordingly, the remaining challenge is to introduce control valves and integrated sensors.

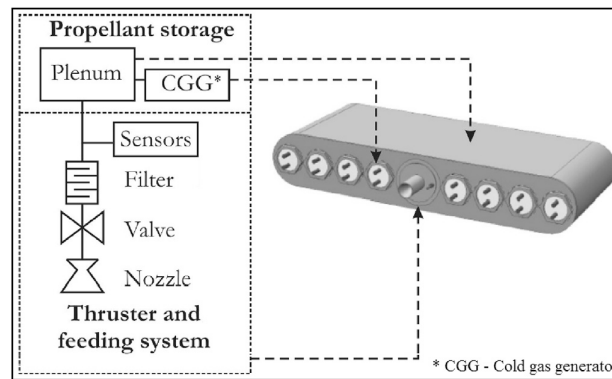


Figure 2.5: Example of cold gas microthruster [5].

Although this CGM system appears feasible, it has flaws. First, these systems are prone to leakages due to the various microscopic contaminants of the space missions, which affect the integrity of the seals. It worsens when the missions are delayed for long periods, as is the case with CubeSats, where significant quantities of the propellants are lost before the mission begins. Consequently, the design of these systems necessitates adjustments to address this risk. It worsens when the missions are delayed for long periods, as is the case with CubeSats, where significant quantities of the propellants are lost before the mission begins.

Acceptable systems, such as the one shown in Figure 2.5, have low leakages in the range of 10^{-5} sccs⁻¹ (standard cubic centimetres per second) [32]. Second, the

propulsion thrust of the system decreases over time during manoeuvres as the pressure of the propellants decreases. These flaws result in constraints for long missions, which could take considerably longer.

CGM systems' designs could vary due to the type of propellant and storage mechanism of the device. Gas propellants are the simplest, and they use pressurized inert gases. Liquid propellants are slightly complex, but they carry more propellants in their liquid form than the gas types. Solid propellants, however, are ignited in the storage tank to produce specific quantities of gaseous products for propulsion. Nevertheless, constraints of the solid propellants include aspects of ignition efficiency and control.

Inert gases are the preferred products due to safety concerns over active gases. Notably, suitable propellants should have high-density I_{sp} (specific impulse-unit volume) to last longer on the spacecraft. Storage pressure of the propellants also presents a safety concern, although it could remain safe if kept at low pressure. These factors are compounded with the availability and toxicity of the propellants that influence the cost of designing these micropropulsion systems. Moreover, propellants that are environmentally friendly have achieved much success in increasing safety and lowering the costs of producing such micropropulsion designs.

2.3.3 Electric MEMS Microthruster

The working principle of an electric propulsion system involves the use of energy from an electric source to ionize and accelerate the propellant to produce thrust [34]. A specialized design subunit processes the energy to produce thrust. The thrust produced is influenced to input power by the equation $F = P_{in}(2\eta/v_e)$, where P_{in} is the input power, η is the power translation proficiency, and v_e is the propellant exit velocity.

Power is a major limiting factor of this system. Microsatellites produce little electric energy and would consequently generate low thrust in such propulsion systems. However, the propellant utilization gives these systems extensive thrusting time and

good impulse. The electric MEMS microthrusters can be classified further into Plasma Microthruster, Colloid Microthruster, Electrospray Microthruster and Resistojets Microthruster based on the method the propellant uses to accelerate out of the system.

2.3.3.1 Plasma Microthruster

Two types of plasma microthrusters are perfect for MEMS technology, the electrothermal plasma microthruster [35], [36] and the liquid-solid propellant pulsed plasma microthruster [37]. The following is a review of the characteristics of different plasma microthrusters in the field today.

1- Electrothermal Plasma Microthruster In principle, electrothermal plasma microthrusters work by discharging low-power plasma. Accordingly, the technology uses heat produced by a microwave or radio frequency (RF) to heat the propellant and generate thrust on discharging it. These electrothermal plasma microthrusters are classified as RF electrothermal thrusters (RFETs) and microwave electrothermal thrusters (METs). However, their working performance remains the same. They both require a power of less than 10 W to produce thrust in the range of mN and up to 85 s specific impulses using gaseous propellants. This technology prefers the use of gases such as A_r , H_e and H_2 for propulsion. The preferred gas is heated in the acceleration chamber to produce plasma under the influence of the charges that creates a charge exchange collision, which defines electrochemical thrusters [38]. Furthermore, electrothermal plasma microthrusters have the beneficial capabilities of producing lightweight, small volume, and cheap designs.

Takahashi *et al.* [6] used azimuthally symmetry to analyse microwave electrothermal thrusters. The microthruster had a source of microplasma, an antenna rod axis and a convergent-divergent (C-D) micronozzle, as highlighted in Figure 2.6. Inside the plasma source chamber were two electric charges, anode and cathode, which form the dielectric chamber. This chamber is covered by a dielectric envelope that enables the device to produce hot plasma at atmospheric pressures.

The Laval nozzle generates thrust by converting this pressurized, high energy plasma into kinetic energy by forcing it to flow at supersonic rates. When using Argon, the system can reach flow rates of 100 sccm (standard cubic centimetre per minute) with the microwave frequency set at about 4.0 GHz, using a power output of less than 6 W. At such conditions, the electrothermal plasma microthruster produces thrust ranging between 0.2 mN and 1.4 mN, and specific impulses range averaging between 50 s and 80 s.

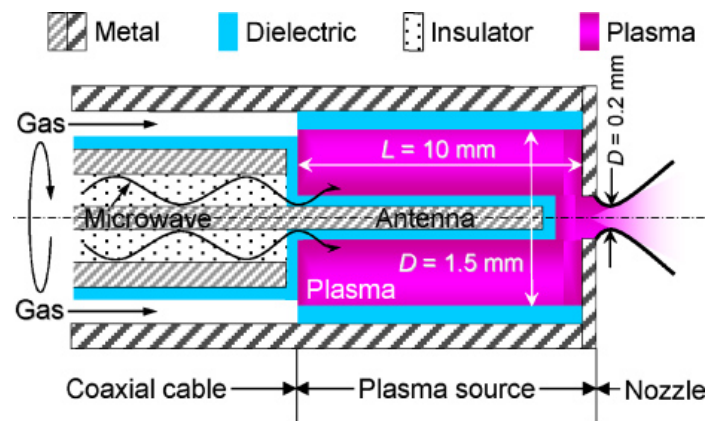


Figure 2.6: Microwave electrothermal thrusters (MET) schematic diagram [6].

2- Liquid-Solid Propellant Pulsed Plasma Microthruster A pulse plasma microthruster works on the principle of producing plasma pulses, which are small amounts of plasma discharged at high velocity using a pulse of energy discharged from the capacitor. The discharge velocity of the plasma creates thrust for the device. Accordingly, one can vary the thrust by adjusting the pulse rates. This system generates accurate thrust with the potential to release a large specific impulse in the range of 4300 s with different pulse intervals. Moreover, it has the structural advantage of developing light, small and simple prototypes that would meet the needs of a micropropulsion system.

One of the earliest designs presented by Guman *et al.* [37], used a solid propellant in mission. The propellant used in this solid-propellant pulsed plasma microthruster was poly-tetrafluoro ethylene (PTFE). The device was simple, reliable and efficient since it

only required low power for its missions. Later, as highlighted in Figure 2.7, Aoyagi *et al.* [7], improved the design by developing a prototype of a pulsed plasma microthruster consisting of a coaxial electrode with an anode, cathode and propellant igniter. Further experimentation confirmed that the diameter of the cathode and a divergent nozzle were crucial factors affecting the thrust performance of these devices. Notably, this technology could reach impulse bits in the range of 300 μNs and 800 μNs with a maximum total impulse of about 40 Ns.

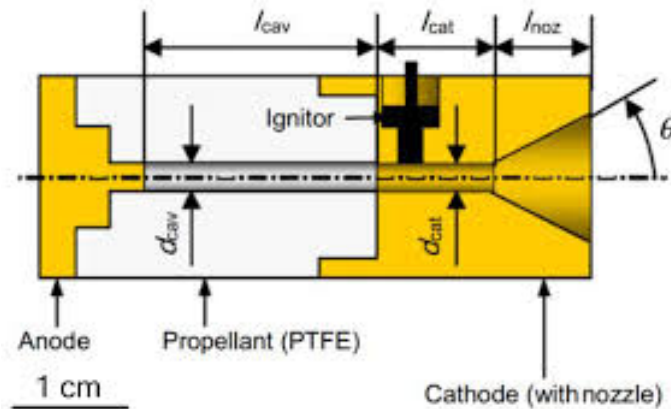


Figure 2.7: Schematic of the Coaxial Pulsed Plasma Microthruster [7].

2.3.3.2 Colloid Microthruster

The working principle of Colloid microthrusters involves charging and accelerating propellants by electrostatic atomization [39]. The system is powerful and records thrust of between 1 μN to 20 μN , and specific impulse ranging between 500 s and 1300 s. One of the core strengths of a colloid microthruster engine is its ability to produce thrust with a small fraction of Micronowton. As such, the engine allows the system to propel a wide span of missions [40].

Some of the early scholars to develop a sandwich structure colloid microthruster were Xiong *et al.* [8], as highlighted in Figure 2.8, and it was made using bulk silicon processing technology. Their prototype has a source emitter, propellant tank and an extractor. The extractor and the source emitter are separated by space. In practice, the

liquid propellant moves by capillary force from its tank to the source emitter tip passing through the microchannel. At the source emitter tip, the liquid is subjected to a strong electric field, which causes it to split into charged droplets that exit the nozzle at high velocity to produce thrust. Notably, the extractor and source emitter of this microthruster are fabricated separately in two wafers, which are bound together in the final device. This device could produce a thrust of between $1.20 \mu\text{N}$ to $4.85 \mu\text{N}$ following a voltage increase from 1400 V to 2800 V.

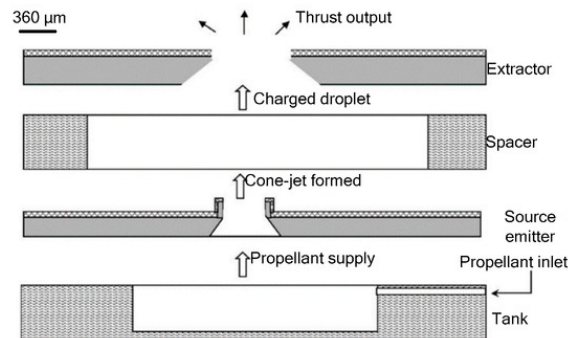


Figure 2.8: Colloid Microthruster Schematic Diagram designed by Xiong [8].

This microthruster has the benefits of producing small, varied nano-to-micronewtons thrusts, and it uses a simple power unit. The designers Xiong *et al.* [41] advanced this earlier prototype to include printed circuit board (PCB) and an integrated silicon micropump. They introduced a precision current vortex displacement sensor to adjust its electrical sensitivity to $8 \text{ mV}/\mu\text{m}$. At its best, the improved microthruster would use 3500 V to produce $2.56 \mu\text{N}$ thrust.

2.3.3.3 Electro spray Microthruster

Electrospray microthrusters are devices that generate a thrust by emitting an electrospray. Microthrusters use a Taylor cone to emit a spray of particles and create thrust [42]. This process occurs by applying an electric potential to an ionic fluid in a capillary until a voltage potential is reached, and the liquid at the capillary tip splits into single ion droplets,

which are ejected in shape forming a cone, as highlighted in Figure 2.9. Accordingly, such emitters would produce thrusts of varied nano-to-micronewtons based on the design dimensions and type of propellant used [43], [8]. Engineers cluster multiple emitters, reaching thousands, to give sufficient thrust to a satellite for the manoeuvres needed on its mission [44], [45]; sometimes, an accelerator grid is added to the design for the exit velocity of particles from the extractor to increase [46], [47].

Suitable propellants include liquid metals, ionic liquids, or a mixture of the two. These devices can work as micropropellant systems for CubeSats and PocketQubes because of the levels of thrust and specific impulse they produce. Moreover, the design approach for these thrusts allows for linear thrust changes by fabricating the appropriate number of emitters.

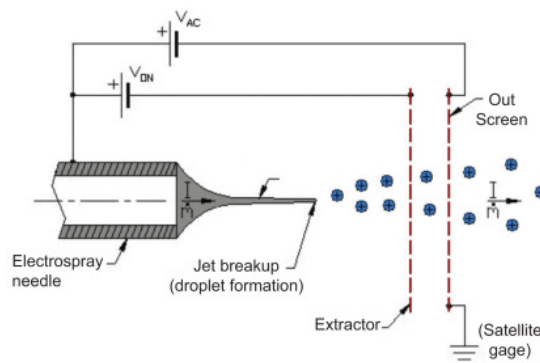


Figure 2.9: Schematic of an electrostatic microthruster [9].

2.3.3.4 Resistojets Microthruster

Resistojets microthrusters primarily work by heat exchange to heat the propellant and increase its pressure before allowing it to exit at high velocity and generate thrust. The propellant used ranges anywhere from gases, liquids to solids, but the released product is usually a gas. When the propellant used is not a gas, the energy used in heating facilitates the changes from one propellant phase to another. That is, liquids should be evaporated

while solids undergo sublimation to shift to their gaseous phases. These propellants are kept at controlled pressure and temperature conditions to facilitate the phase change process. The heat exchanger used in heating the propellants works based on resistance to generate the heat needed in the propulsion system. Conditions of pressure in the heat exchanger are also crucial in making the phase changes of the propellant efficient.

Resistojets can be classified according to the phase change processes involved in the system into Low-Pressure Microresistojet (LPM), which is also called Free Molecule Micro-resistojet (FMMR), and Vaporizing Liquid Microthruster (VLM), as shown in Figure 2.10 below. In the VLM, the propellant is expanded through adiabatic expansion and controlled to exit through a convergent-divergent nozzle. The flow of this propellant is modelled according to the Knudsen number $kn < 0.01$ of the continuum flow range [48], where the Knudsen number helps determine whether continuum mechanics formulation can be applied in a system and can be defined as the ratio of the molecular mean free path to the characteristics length as in the equation. $K_n = \lambda/L$.

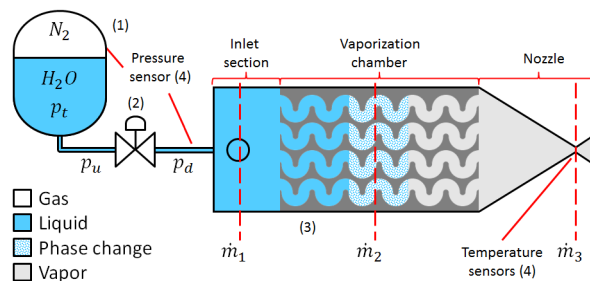


Figure 2.10: VLM system showing: (1) a tank; (2) a solenoid valve; (3) a thruster; m_1, m_2, m_3 are the mass flow rate [10].

However, other experts argue that a mathematical modelling method, such as the direct simulation Monte-Carlo (DSMC), is used as it gives more precise measurements than using the Navier-Stokes equations to analyse the flow in the exit nozzle since this region gives a high Knudsen number. Designers have analysed the prototypes using both equations to adjust their designs appropriately. However, the LPM design is modelled in a

transitional flow regime since the system works at low pressure, while its Knudsen number is usually high ($0.1 < Kn < 10$). During nozzle tests, nitrogen is the preferred propellant, while water is the best alternative during concept tests. Some micropropulsion systems use water and nitrogen as their working propellants [49].

1- Low-Pressure Microresistojet (LPM) The low-pressure microresistojet works at low pressure in the range ($0.1 < Kn < 10$), which necessitates working in the transitional flow regime. It is sometimes given the name Free Molecule Microresistojet (FMMR). As such, the gas kinetic theory is best suited for modelling and simulation of operations using this microthruster [50], [51].

The device has three major sections: an inlet, a heater chip, and a plenum, as per Figure 2.11 below. The plenum allows for low-pressure injection of the gas at pressures as low as 1000 pa. As such, the heater chip has multiple microchannels that generate heat by resistance to gain sufficient heat exchanged with the flowing particles that come into contact with these walls. Engineers consider the geometry of this heater chip mainly to ensure that the heat is efficiently transferred to the gas to functionally produce adequate thrust [52], [53]. Furthermore, to ensure efficiency in electrical consumption, the prototypes are fabricated with materials and systems that consume less electric power during heating.

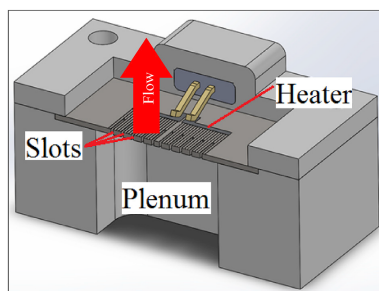


Figure 2.11: The cross section of the LPM indicates the parts of the thruster; the flow is in the direction indicated by the red arrow [10].

Moreover, designing a low-pressure microresistojet still requires precise system adjustments, despite the conceptual and numerical data confirmed in experiments. The

choice of propellant and approaches to its storage are crucial. For instance, the pressure requirements in the plenum, as provided in the design, determine the design adjustments of the tank and valve of choice. Simulations and tests of prototypes primarily use inert gases and water for their safety properties, but there remain options for other fuels, which could produce better results [49], [50], [54], [55]. Notably, this system uses a simple design approach, which is easy to scale up or down. The key is in adjusting the number and size of channels to realize the desired thrust outputs.

2- Vaporizing Liquid Microthruster (VLM) The Vaporizing Liquid Microthrusters are among the most feasible micropropulsion technologies for a CubeSat. Based on their simple designs, VLMs have been scaled down significantly and are currently being manufactured using MEMS technology, as shown in Figure 2.12 below. Accordingly, the system is built-in ceramic or silicon wafers. The structure of VLMs consists of an inlet channel through which the propellant is fed, a chamber where a heating element vaporizes the propellant, and a convergent-divergent nozzle to accelerate the gasses to supersonic velocities.

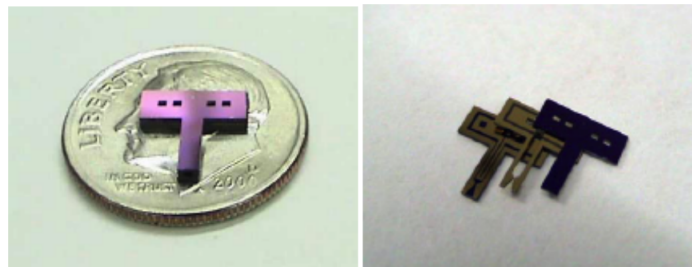


Figure 2.12: JPL Vaporizing Liquid Microthruster (VLM)[11].

Most of the works on determining the VLM characteristics have been done mainly experimentally rather than numerically. Some studies have been done on this system to numerically analyse the chamber and nozzle configurations for high output [56], [57]. Nonetheless, there remain several constraints in the optimization of the boiling chamber to ensure the excellent performance of the devices [58], [14].

The primary concern is the need to adjust the boiling chamber's energy efficiency. Much energy is required to vaporize the propellants for a spacecraft to gain thrust, yet the supply of such energy could constrain smaller crafts like the CubeSat. As such, the geometry and type of materials used on this propulsion system determine the energy efficiency of the device [56], [57], [59], [17]. Furthermore, the trade-off between safety and efficiency is equally a challenge. Propellants such as water are preferred due to their safety and storage benefits [60], but they result in crucial energy constraints for operations. The vaporization point of water is high, and substantial energy is needed to vaporize water in a VLM. Nonetheless, water vapour produces the best thrust due to its ability to produce high-velocity increment Δv per volume, which translates to a higher specific impulse that could propel the Cubesat effectively [60].

Aligning the drawbacks and benefits of such propellants is a remarkable milestone for engineers. The manufacturing process also differentiates the VLM designs applicable to propulsion devices, as highlighted in Figure 2.13. On the one hand, there is a process used to manufacture out-of-plane VLM designs. These designs tune the etching process and the wafer types together to form cavities with walls that are inclined to about 54.7° to create nozzles that are perpendicular to the wafer plane [13], [61], [12]. Other procedures, such as the Bosch process, are sometimes used in this etching step to produce more complicated shapes for the out-of-plane nozzles [62]. While this design makes the development process simple, it decreases the flexibility of the design and reduces its performance.

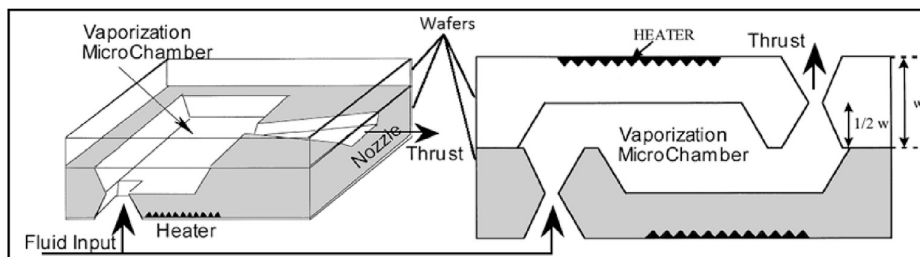


Figure 2.13: Comparison between two different designs: In-plane design of thrust (left) and out-of-plane design of thrust (right) [4].

On the other hand, the nozzle of the propellant system is etched on one of the wafer planes to take a pseudo-two-dimensional characteristic that makes the in-plane design [15], [63], [16]. Unlike the out-of-plane design, this in-plane design retains the freedom of the design prototype. However, it trades off the simplicity of the prototype in allowing for the fabrication of some modifications. The primary material for fabricating this design has been silicon, but experts perceive some prospects in the use of Low-Temperature Co-Fired Ceramic (LTCC), which is cheap and easy to manufacture [64], [65]. The existing prototypes can produce thrust in the range between 1 μN and 7 mN, and use between 1 and 10 W, although some missions could require more electrical power.

a - VLM With Internal Microheater The position of the heater in a VLM is crucial in increasing efficiency. As such, a VLM with an internal microheater has its resistance-based heater fabricated inside the vaporization chamber so that the liquid has direct contact with the heater to minimize heat loss. However, this design is problematic for engineers since fabricating an internal heater and ensuring a connection to an external wire. Mueller *et al.* [66], developed the earliest VLM using MEMS technology in 1997 .

Further studies in this area continued, and in 2000, Ye *et al.* [12], proposed a VLM that would use electric pulses to vaporize water into pressurized water vapour. This VLM prototype is highlighted in Figure 2.14 below, and it contained a propellant inlet, a microresistor, a vaporizing chamber, a micronozzle, two silicon wafers and a microchannel. These engineers fabricated an internal Titanium (Ti) heater in the vaporizing chamber with its electrical source connection on the outside. Its microthruster chip was formed by binding the bottom and top chips together using glue. Their prototype used 30 W electrical power to produce 2.9 μN thrust during its test.

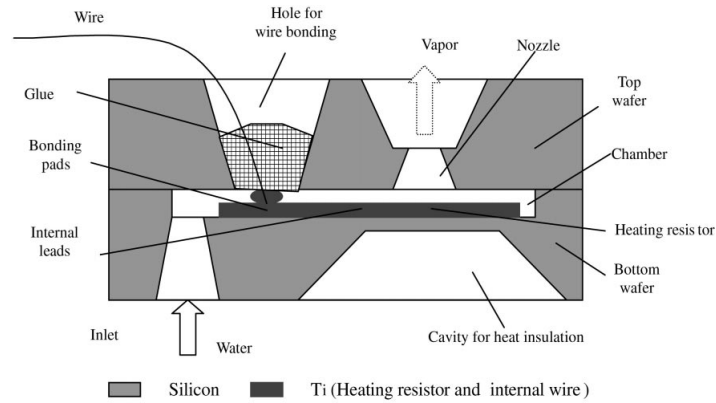


Figure 2.14: Schematic view of an internal microheater vaporizing liquid microthruster (VLM) modeled by [12].

In another experiment conducted in 2005 by Maurya *et al.* [13], used a P-diffused microheater to develop a VLM using silicon. Their design had two micromachined chips bonded together. The P-diffused heater was fabricated inside the vaporizing chamber by diffusing boron and allowing the heater to be passivated using heat grown silicon oxide at the bottom of the silicon substrate. This heater worked on the principle of resistance to produce heat. Figure 2.15 shows a cross-sectional view of the VLM. Some of the important parts included an inlet and outlet at the top and bottom of the vaporizing chamber, respectively. A P-diffused meander line resistor is located at the bottom of the vaporizing chamber, and a microchannel with a v-groove conformation also exists. The system was bound together using an adhesive. The output of this prototype produced thrust between 5 mN and 120 mN, with the flow rate reaching 1.6 ml.s^{-1} and used power in the range of 1.0W to 2.4W [13].

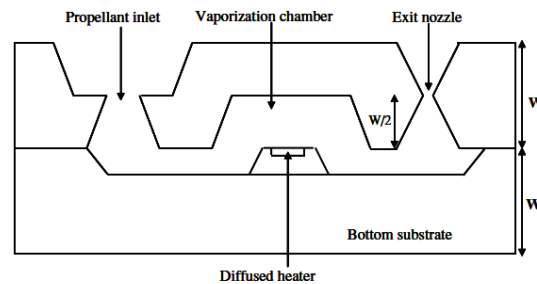


Figure 2.15: Cross-sectional view of the VLM [13].

In 2012 Karthikeyan *et al.* [65] experimented with the use of (LTCC) material in fabricating a VLM microsystem and were successful. They designed it to have a nozzle throat size of 220 μm x 200 μm . This system produced a thrust ranged from 34 mN to 68 mN, and an average specific impulse ranged from 3.4 s to 6.9 s at a flow rate of 1 $\text{mg}\cdot\text{s}^{-1}$ with an input power ranged from 7.1 W to 9.2 W.

Furthermore, in 2014 Cheah *et al.* [64], tested the use of high-temperature co-fired ceramic (HTCC) technology in scaling a MEMS level VLM. They successfully developed the system with a vaporizing chamber injector, microheater and micronozzle. Hence, other materials are promising for VLM development technologies. Although many studies have used silicon as the substrate material in developing VLMs, other microsystems have explored the potential of ceramic fabrications [67].

b - VLM With External Microheater It is not strategic to fabricate a heat-dependant system, such as a VLM, outside a spacecraft since it would lose more heat to the environment and eventually consume more power. The external VLM microheater would have more significant power needs than an internal VLM microheater. Furthermore, the fabrication of an external microheater is much simpler than an internal microheater design. Some of the earliest designers of a VLM external microheater using MEMS technology were Mukerjee *et al.* in 2000 [4]. Their design had two micronozzle structure designs, with one located on top of the device and the other on the side, as depicted in Figure 2.16 below. Accordingly, the microchambers of the side VLM micronozzle design were sealed with glass on the silicon substrate. They were sealed by bonding the wafer to a glass wafer Pyrex using the Karl Suss Anodic Bonder (SB-6).

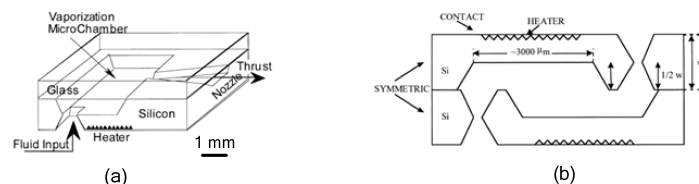


Figure 2.16: A diagram of two microthrusters. (a) the side exit of the nozzle and (b) the top exit of the nozzle [4].

Furthermore, when the VLM is in operation, a window allows the fluid flow in the microchambers to be observed. The top exit nozzle was developed by aligning two identical wafers and pressing them together to form a silicon fusion bond with no pores between them. This bond was subjected to annealing by burning it in 1000 C° of nitrogen for 10 minutes and allowing it to dry in oxygen for another 50 minutes. The device was then equipped with two microheaters on the top and bottom sides of the silicon wafers to have a complete microthruster.

In another experiment conducted in 2010 by Chen *et al.* [14], used simulations to analyse the performance of a VLM thruster. They developed a 3-D model of the VLM, which was used for the simulations. The prototype they were investigating is presented in Figure 2.17 below and, it consists of a silicon wafer and a Pyrex glass wafer with the VLM structure of two inlets and channels. The glass Pyrex 7740 wafer was strategically placed on top to serve as a top cover and had an injecting hole. It was bound to the silicon wafer using an anodic bonding method, which was annealed by using 700 V power and 450 C° temperatures for about 15 minutes. This device produced a thrust of between 1 mN and 6 mN with an outlet configuration of 1 mm by 100 μm . This evidence confirms the potential of VLM in creating a better micropropulsion system for CubeSats.

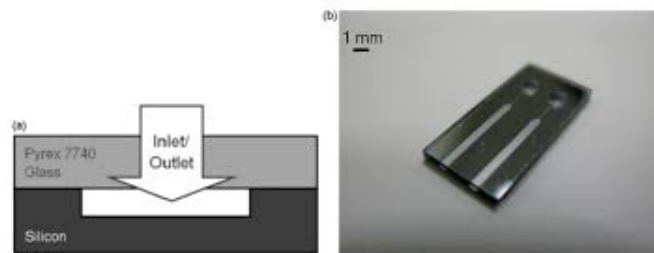


Figure 2.17: The VLM chip consists of a Pyrex glass and a silicon: (a) The cross-section of one channel, (b) the picture of the VLM with an outlet width of 1000 μm [14].

Further studies in this area continued, and in 2012 by Kundu *et al.* [15], also presented a device with microheaters on the top and bottom sides of the microchamber . In their prototype, VLMs consisting of a convergent-divergent nozzle, an inlet channel and

a microchamber were integrated into two micromachined, bonded silicon chips by adhesive glue; its 3-D outlook is highlighted in Figure 2.18 below.

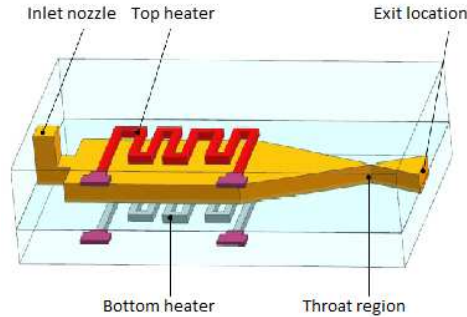


Figure 2.18: 3D schematic view of the complete MEMS-VLM microthruster sandwiched between top and bottom microheaters [4].

The scholars used the high sensitivity OHAUS Discovery Semi-micro dual Range Balance, as seen in Figure 2.19 below, to measure the thrust output of their design. They used an infrared heating bulb to overcome the effects of condensation on the balance stage, which could have affected their findings. Nonetheless, additional effects could occur due to vapour condensation if the device was left to work for long a period. Notably, their device recorded a thrust of 1 mN at $2.04 \text{ mg}\cdot\text{s}^{-1}$ flow rate, and consumed 3.6 W of power using a $130 \text{ }\mu\text{m} \times 100 \text{ }\mu\text{m}$ microthroat.

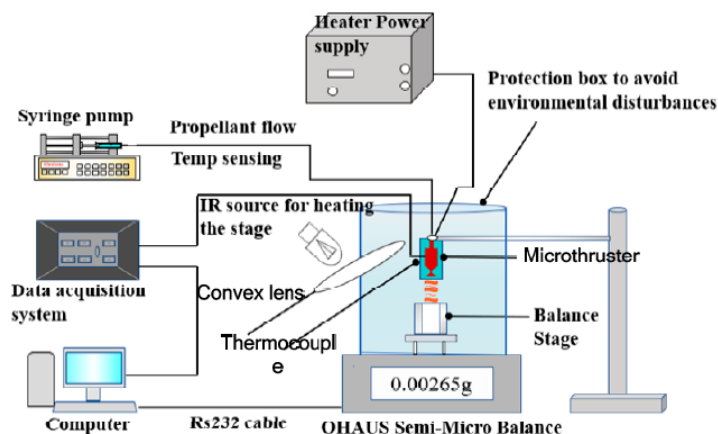


Figure 2.19: Thrust estimation configuration diagram using a semi-microbalance [15].

For the VLM system, the microheater, micronozzles, and vaporizing chambers affect the device's performance. The various sections of a micro thruster are configured to produce specific outputs in each chamber and determine the device's overall output. Primarily, these sections are designed to increase the efficiency and throughput of the microdevice.

Moreover, in 2018 a study by Silva *et al.* [16] analysed two microheater designs, three nozzle designs, and four microchannel designs using simulations to detail the output of different scenarios as depicted in Figure 2.20 below. For example, the ratio of long, wide, and bell nozzles between the exit area and throat area is 11, 17, and 11, respectively. In the same respect, the long nozzle produced a thrust of between 0.7 mN and 3.79 mN with a specific impulse of between 105 s and 113 s. The wide nozzle produced a higher thrust of between 0.77 mN and 3.86 mN, and its specific impulse was between 107 s and 115 s. Thus, these variations are crucial in developing prototypes of VLM devices applicable on CubeSats.

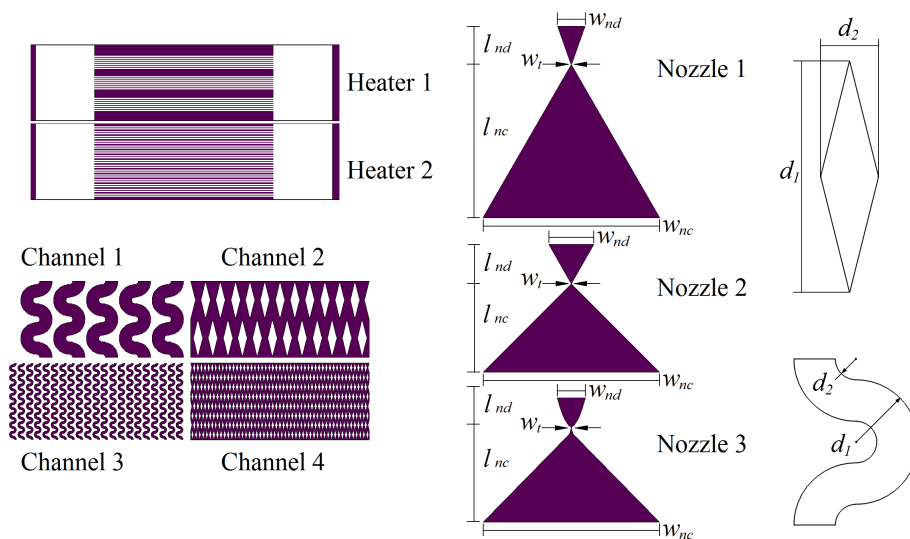


Figure 2.20: Schematic overview of the various designs for each section of the VLM [16].

In 2020 Bendong Liu *et al.* [17], presents a research paper, a new tubular vaporising liquid microthruster (VLM) with induction heating, as seen in Figure 2.21 below. A microheater core, an excitation coil, a vaporising chamber, a nozzle, and a

microchannel are all integrated into a glass tube with an outer diameter of 3 mm and a length of 18 mm. Experiments are used to determine the temperature of the microheater core, and an appropriate AC frequency for the VLM is chosen based on the results. In his experiment, vaporisation of water-propellant feeding was demonstrated with various flow rates ranging from 0.1 ml.min^{-1} to 0.3 ml.min^{-1} , resulting in a maximum thrust force of $680 \mu\text{N}$ at the 0.3 ml.min^{-1} propellant consumption rate. As compared to other VLMs, his has no physical relation between the microheater core and the power supply, allowing it to operate with higher input power, produce more heat energy, and generate a higher thrust force.

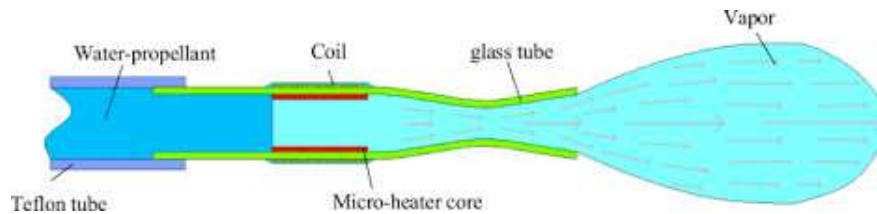


Figure 2.21: Schematic of the work process of the VLM [17].

3 The Vaporizing Liquid Microthruster (VLM)

3.1 Concept of Vaporizing Liquid Microthruster

The thrust that propels a CubeSat at high velocity is produced by a hot gas when released through the convergent-divergent nozzle of a microthruster at high pressure. To facilitate this function, the microthruster stores an electric resource and a propellant onboard, as highlighted in Figure 3.1 below.

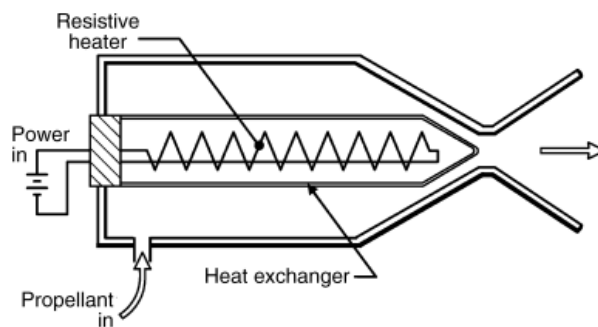


Figure 3.1: Illustration of the resistojet concept [18].

Typically, the electric power is produced from solar panels on the surface of the CubeSat, which capture the solar energy, storing it in batteries. The propellant is stored in tanks on the device. Equation (3.1) highlights the important performance metrics involved in this process of producing thrust [19].

$$\eta_{F.P} = \frac{F \cdot g_0 \cdot I_{sp}}{2} \quad (3.1)$$

where:

- $\eta_{F.P}$ is the thrust efficiency, defined as the ratio of jet power to input power.
- F is the thrust input force N.
- g_0 is the standard gravitational acceleration at sea-level, approximately $9.81m.s^{-2}$.
- I_{sp} is the vacuum specific impulse of the thruster in (s).

The propellant is not the primary energy source as it is with other systems, like rockets. Instead, it produces thrust when the pressurized gas exits through a valve at high velocity. Storage tanks for the propellant and a source of electrical energy are stored onboard as payload. Propellants are compressed in propellant tanks, while electric power is produced from solar panels attached to the spacecraft and stored in batteries on board.

Equation highlights how different parameters of this system are linked to the performance of VLMS. This equation relates the thrust to the power consumption generation and qualities of propellant consumption (F and I_{sp} , respectively). It indicates that either more fuel, lower I_{sp} (i.e. higher propellant consumption), or higher efficiency are needed to achieve a specified amount of thrust.

In general, the vacuum specific impulse I_{sp} is the most relevant output quality for space propulsion systems. The theoretical limit of I_{sp} is found in [68] by integrating the Equation (3.2) and Equation (3.3).

$$v_L = \sqrt{2 \frac{\gamma}{\gamma - 1} \cdot \frac{R_A}{M_{Prop}} \cdot T_c} \quad (3.2)$$

$$I_{sp} = \frac{v_e}{g_0} \quad (3.3)$$

where:

- v_L is the limit exhaust velocity, for perfect adiabatic expansion in vacuum [$m.s^{-1}$].
- γ is the specific heat ratio of the propellant.
- R_A is the universal gas constant, equal to $8.314 [J.mol^{-1}.K^{-1}]$.
- M_{prop} is the molar mass of the propellant in [$kg.mol^{-1}$].
- T_c is the chamber temperature in [K].
- v_e is the exhaust velocity in [$m.s^{-1}$].

I_{sp} increases with propellant temperature with an ideal nozzle and decreases with molar mass and specific heat ratio as shown in the equations (3.4) and (3.5) . The thrust is extracted from:

$$F = \dot{m} \cdot g_0 \cdot I_{sp} \quad (3.4)$$

$$\dot{m} = \frac{\Gamma \cdot P_c \cdot A_t}{\sqrt{\frac{R_A}{M_{prop}} \cdot T_c}} \quad (3.5)$$

where:

- \dot{m} is the propellant mass flow in [$kg.s^{-1}$].
- Γ is the Vandekerckhove function (a propellant property).
- P_c is the chamber pressure in [Pa].
- A_t is throat area [m^2].

Notably, considering an ideal system, it is evident that the specific impulse is affected by the chamber's temperature when the pressure is kept constant. However, the thrust of a CubeSat system is affected by the system's pressure when the temperature remains constant. The performance of a vaporizing liquid microthruster can be evaluated as follows. On the one hand, the effect of temperature on its performance is determined by assessing the performance of the heating chamber. On the other hand, the effect of pressure is assessed by investigating the performance of the nozzle.

The primary task of the heating chamber in a vaporizing liquid microthruster is to vaporize the propellant as it flows. Furthermore, it should increase the temperature of the vapour to the desired chamber requirements. Accordingly, it should possess the potential to achieve these heating expectations efficiently. These efficiency metrics are detailed as follows:

$$\eta_{chamber} = \frac{Q_{\Delta T}}{Q_{el}} = \eta_{th} \cdot \eta_{el} \quad (3.6)$$

$$\eta_{th} = \frac{Q_{\Delta T}}{Q_{\Delta T} + Q_{evap}} \quad (3.7)$$

$$\eta_{el} = \frac{Q_{\Delta T} + Q_{evap}}{Q_{el}} \quad (3.8)$$

where:

- $Q_{\Delta T}$ is the energy added to increase the flow temperature every second [W].
- Q_{el} is the electrical power consumption in [W].
- η_{th} is the thermal efficiency.
- η_{el} is the electrical efficiency.
- Q_{evap} is the power consumed to evaporate the flow in [W].

Note that Q_{evap} is set for a given flow rate. At extremely high T_c efficiency will be decreased at T_c growth due to high losses through the side-wall. The function of the nozzle is to convert the thermal energy stored in the propellant into kinetic energy, generating thrust. The I_{sp} efficiency Equation (3.9) is one way to define the quality of the nozzle:

$$\eta_{I_{sp}} = \frac{I_{sp,real}}{I_{sp,ideal}} \quad (3.9)$$

One of the most common causes of VLM failure, as reported in [69], [70], and others, is a phenomenon known as sputtering. When the flow is not totally vaporised and liquid droplets remain in the nozzle flow, sputtering occurs.

3.2 Performance of Vaporizing Liquid Microthruster

Although microthrusters are particularly small, the assessment of their performance can be similar to that of normal-sized propulsion systems. It is however, crucial to note that the assumptions used in such formulations are partly different for micropropulsion systems since negligible forces in the normal-sized propulsion systems, such as friction, have a significant impact on micropropulsion devices. Therefore, the equations [71] applied in the analysis of the performance of such micropropulsion devices are highlighted below. The essential parameters in these equations used for micropropulsion systems are thrust and specific impulse. Thrust (F) defines the force produced by the gas as it accelerates and exits the nozzle, as highlighted in Equation (3.10).

$$F = \dot{m}v_e + (P_e - P_a)A_e \quad (3.10)$$

where v_e is the exhaust velocity ($m.s^{-1}$), P_e and P_a are the exit and ambient pressures (Pa), and A_e is the area of nozzle exit (m^2). It is possible to calculate the exhaust velocity by (3.11).

$$v_e = M_e \sqrt{\gamma R_s T_e} \quad (3.11)$$

where M_e is the exit Mach number, γ is the specific heat ratio that is equal to $\gamma = C_p/C_v$, where C_p = heat capacity at constant pressure, C_v = heat capacity at constant volume, T_e is the exit temperature, and R_s is the specific gas constant.

As a function of the chamber (stagnation) pressure and temperature (P_c and T_c) and the area of the throat, the mass flow rate can be written as:

$$\dot{m} = \frac{A_t P_c}{\sqrt{T_c}} \sqrt{\frac{\gamma}{R_s} \left(\frac{2}{\gamma+1}\right)^{\frac{\gamma+1}{\gamma-1}}} \quad (3.12)$$

For calculating the Mach number, temperature and pressure at the exit, the equations (3.13) to (3.15) are used.

$$\frac{A_e}{A_t} = \left(\frac{\gamma+1}{2}\right)^{-\frac{\gamma+1}{2(\gamma-1)}} M_e^{-1} \left(1 + \frac{\gamma-1}{2} M_e^2\right)^{\frac{\gamma+1}{2(\gamma-1)}} \quad (3.13)$$

$$T_e = T_c \left(1 + \frac{\gamma-1}{2} M_e^2\right)^{-1} \quad (3.14)$$

$$P_e = P_c \left(1 + \frac{\gamma-1}{2} M_e^2\right)^{\frac{-\gamma}{\gamma-1}} \quad (3.15)$$

The I_{sp} specific impulse is a measure of efficiency with respect to propellant consumption.

$$I_{sp} = \frac{F}{\dot{m}g} \quad (3.16)$$

Since the unit is stated in seconds, it does not reflect a time factor but a thrust measure per unit of propellant weight and should be as high as possible for the maximum efficiency of propellant consumption.

The conditions of the mechanical characterization of the microthruster can be given using equations (3.10) and (3.16) to estimate the thruster performance. So, the more outlet velocity with constant mass flow rate, the more thrust and efficiency of the thruster obtained. For this reason, the optimization of the VLM is based on the maximization of the average outlet velocity into the outlet nozzle.

The Q power required to heat up and vaporize the liquid from initial temperature to boiling point and overheating of the gas to the temperature higher than the saturation temperature of the liquid is determined according to the following equation:

$$Q = \dot{m}\Delta H \quad (3.17)$$

where:

$\Delta H = H_V - H_L$, H_V is gas enthalpy and H_L is liquid enthalpy.

These equations are used to calculate the efficiency and functionality of the heating chamber. The heating chamber is the section of the microthruster in which the propellant is vaporized and heated to the desired temperature.

3.3 Description of VLM Design

The concept of the VLM design is based on the construction of the thruster from the brick of silicon. The primary technological operations of silicon VLM construction are:

1. Production of bottom silicon brick.
2. Etching of the silicon and creating of channels inside of the silicon brick.
3. Production of top silicon brick.
4. Plasma deposition of the electric heater on the chamber side-walls.
5. Connection of bottom and top silicon bricks with each other.
6. Installation of inlet nozzle.
7. Connection of electric wires to the electric heater.

These technological operations allow a channel with a complex shape to be created inside silicon. Discussion of the main components of the VLM, as highlighted in Figure 3.2 below, now follows.

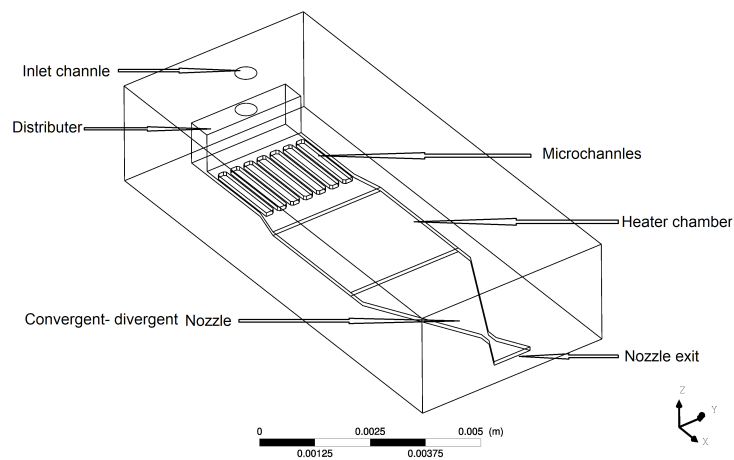


Figure 3.2: Sketch of the VLM.

Inlet channel:

Inlet nozzle is designed like a circular pipe to have at the same time maximum possible diameter to reduce pressure drop and minimum possible diameter to increase flow velocity, prevent boiling into the inlet section and stabilize the flow. After the inlet orifice, the flow comes into the distributor section. The angle between the orifice and longitudinal axis of the VLM was selected equal to 90° . Issues of fluid flow, such as viscosity, surface tension, the surface to volume ratio, and fluid resistance, among others, are crucial in a microscale system since they could result in constraints such as blockages and slow delivery of the propellant if the configurations have not precisely considered these fluid flow characteristics [72]. As such, the Reynolds number Re in microchannels is much smaller than the critical Re number. That is why the flow will be laminar, which is efficient.

Distributor:

The design of the distributor is equally essential in a micropropulsion system. The distributor uniformly distributes the liquid from the inlet section to the array of microchannels. Boiling of water in this section is highly accrued, so that this section is designed to have a lower temperature than the saturation temperature of the water, as little as possible and to avoid sharp edges between the distributor and microchannel inlet.

Microchannels:

The geometry of microchannels considers many parameters. Some of the considerations made in the straight channels include the ability to predict the thermal efficiency and pressure drop, simplicity of the system, and ability to minimize thermal losses to the environment [73]. Eight parallel rectangular microchannels were selected. Microchannels are spaced apart and have bevel edges at the entrance and exit. The length of the microchannels has to be long enough to reduce the temperature of the silicon brick at the inlet section up to a temperature lower than the saturation temperature of the liquid to ensure the enhancement of the heat transfer coefficients, control of the instabilities caused by flow boiling, and reduce the pressure loss in the system. However, when water came

into contact with the junction of square inlet and microchannels, where there were sharp corners, taints, or an insoluble gas bubble, boiling became usually easier [58]. Nevertheless, several geometry modifications have been considered to reduce the flow boiling instabilities.

Heater chamber:

This VLM system uses the heating chamber described in [15]. The heaters in this chamber are equally essential. The chamber adopts two heaters instead of one, which facilitates rapid and uniform heating of the liquid propellant. A well-developed heat exchange surface between liquid and VLM side-wall was created to obtain well-heated gas without droplets. However, the location of the heating chamber on the present system was modified. It is not in the top and bottom of the microchannels section. It is after the microchannels section to stabilize the flow and increase the heat transfer area, which enables the flow to reach boiling point in the middle of microchannels, allowing gradual and controlled vaporization of the propellant reaching superheated gaseous propellant in the chamber region, raising specific impulse and power efficiency. This adjustment was adopted to gain the advantages of length in the heating chamber, which is essential in designing a system with significantly lower flow velocities and requires a highly laminar flow.

Convergent-Divergent Nozzle:

At the very tip of the microthruster, there is a nozzle that completes the function of releasing the propellant to generate thrust. This nozzle is designed with special considerations of its geometry to ensure that it works appropriately. The design should involve calculations of the throat to provide a maximum speed of the propellant exiting, thereby guaranteeing the maximum thrust possible. In addition to the geometry shape, the performance of this microsystem nozzle is influenced by the size of the nozzle. The functional requirement of this system to produce thrust in the range of just a few mN necessitates proper modification of its boundary layers and modifications to address the roughness of the nozzle to achieve precise performance.

The perceived constraints in fabricating the appropriate nozzle for this micro-propeller system led to an in-plane supersonic nozzle. The nozzle resembles the De-Laval supersonic nozzle, which is configured with a cross-sectional area that changes smoothly and uniformly across the axis of the nozzle. Accordingly, the geometry of the nozzle should be designed in a manner that produces straight side walls to produce a coincidence angle between the nozzle axis and the sidewall. According to Van Wees, increasing the nozzle Reynolds number over 2000 will almost likely result in a considerable boost in performance. Increasing the nozzle Reynolds number can be done by raising either chamber pressure or throat area, both of which enhance mass flow.

The throat of this nozzle is sized in a ratio that facilitates supersonic velocity of the propellant at a relatively low chamber pressure. Therefore, when the superheated propellant gas in the heating chamber hits the nozzle, its kinetic energy forces it down the nozzle throat at supersonic velocities to produce the optimal thrust as it exits the system. Notably, the throat length is about 50 μm long to facilitate proper fabrication. According to [74], the optimal nozzle convergence angle is 28° .

The divergent angle of the nozzle is equally essential in the performance optimization of a convergent-divergent nozzle. The present design adopted a semi divergence angle of 23° , which was ideal in reducing the viscous losses linked to the increasing sizes of the boundary layer to the planar walls, a condition with a negative consequence on the performance of the micronozzle due to the increasing length of the divergent section [75].

The adiabatic expansion of the exiting gas poses another constraint for the nozzle exit. Pijus Kundu *et al.* [15], noted that, for nozzle area ratios (A_r) ranging from 5 to 9, proper adiabatic expansion of superheated steam without ice formation at the nozzle exit is possible. Moreover, water as the propellant of choice presented the challenge of condensation at the nozzle exhaust.

3.4 VLM Physical Processes

Within the VLM, the electrical energy must be converted into the thrust force. To do this, the heat carrier (water) needs to be converted to steam and accelerated as fast as possible to increase the thrust force and efficiency of the device. The VLM is divided into four different sections that were described in Section 3.3. First is the inlet section (Inlet channel-distributor), where the heat carrier flow (in liquid phase) should be distributed between microchannels. In this part of the thruster, some pressure drop and heating of the water occurred. Those physical processes will be discussed.

The second section is the microchannels, and these work like steam generators. On the inlet part of the microchannels is an economiser region, which is located where the liquid heat carrier is heated up to the saturation temperature of the liquid. Later the boiling of the liquid is observed at an almost constant temperature. It is preferable that the boiling of the water will be observed somewhere in the middle of the microchannels. On the outlet of the microchannels, a region is observed where the steam overheats over the saturation temperature of the water. At the microchannel outlet, only a gas phase (heat carrier) is present, and there is no liquid phase.

The third section is the heater chamber section, where the flow comes from the microchannels region and overheated to superheated steam at the nozzle inlet.

The fourth section is the in-plane supersonic (converged-diverged) nozzle, where the flow from the chamber is accelerated even more, up to supersonic velocities. Accelerated steam exits from the nozzle and produces thrust force converting the electrical energy to a thrust force into the VLM. Each section's component efficiency the VLM's should be improved To enhance the VLM's efficiency. Keeping the pressure drop as low as possible is critical to avoid flow separation from the walls and to maximise heat transfer between the heat carrier and the thruster side-wall. Furthermore, optimising the shape of the outlet nozzle is vital to maximising the flow's overall output impulse.

3.5 VLM Optimization Technique

The concept sketch of the VLM design is presented in Figure 3.2. It is not the best possible design and should be optimized. The better way to start the optimization of the device is from the most crucial part, the outlet nozzle that produces the thrust force. To ensure proper flow (dry, overheated steam) for the VLM's supersonic section, the inlet (subsonic) part of the VLM has to be optimized too. The optimization process was performed at a fixed mass flow rate of the fluid carrier through the VLM. Optimization techniques of the supersonic and subsonic parts of the VLM are presented in sections 3.5.1 and 3.5.2 correspondingly below.

3.5.1 Supersonic Region (Convergent-Divergent Nozzle)

During optimisation of the supersonic region of the VLM, the requirement was to maximise the output impulse of the steam. First, the most appropriate shape of the supersonic nozzle must be designed. Due to manufacturing limitations, an in-plane supersonic nozzle was used. Similar to the De Laval supersonic nozzle, conditions must be created where the cross-section area of the nozzle changes smoothly and uniformly along the nozzle axis. So that, the shape of the nozzle side-wall should be created as a straight line with some incident angle between the side-wall and nozzle axis. The flow was observed at the speed of sound in the throat area. The throat area was designed as a short rectangular tube with curves to the diverge and converge areas of the nozzle to stabilise the flow in the throat area.

The divergence degree, length and size of the throat part were optimised in a series of optimisation simulations. The convergence angle was taken equal to 28° according to [30], as one of the most optimal. Results of these simulations and the most optimal shape of the outlet nozzle are presented in chapter 5.

The technique of the outlet nozzle shape optimisation is based on the maximisation

of the outlet impulse. More than 20 numerical simulations have been performed to optimise the outlet nozzle. With every simulation during the optimisation process, some changes and morphing were added into the shape of the outlet nozzle to increase the thrust compared to previous simulations. As a result of the outlet nozzle optimisation, the most optimal flow parameters were obtained on the chamber inlet of the VLM that a subsonic part of the device should produce.

3.5.2 Subsonic Region (Inlet-Distributor-Microchannels-Chamber)

During optimisation of the subsonic region, it was necessary to prevent the heat carrier from boiling into the region before the microchannels, maximise the heat transfer between the silicon and heat carrier and obtain appropriate flow parameters to ensure the supersonic part works well with the optimum mode of the flow.

The optimisation process was produced by using numerical methods via CFD code ANSYS-CFX. As the simulation process of the multi-phase flow with complex geometry is very computationally intensive, automatic optimisation methods were not appropriate.

The optimisation was based on the following principles: to reduce the temperature of the silicon in the inlet section of VLM, it is requested to create silicon layer thinner and longer; to prevent boiling process into the inlet section of VLM, it is requested to decrease the volume of fluid into the inlet section, remove unwanted vortices, increase flow velocity; to intensify boiling process inside of the microchannels, it is requested to increase the number of the channels and reduce the flow velocity. Using these ideas, a series of simulations were produced where all parameters were changed as per the details above. The results of the subsonic region optimisation are presented in chapter 5.

3.6 Computational Fluid Dynamics Methods of Flows Simulation

This section presents a brief review of modern CFD methods, codes and computational resources that are used in this work.

3.6.1 CFD Models

The main research aim of this work can be achieved by using different, well-developed numerical methods. Most of them are developed to simulate a single-phase medium with subsonic velocities. However, this work seeks to simulate multi-phase flow with supersonic velocities. This type of task is similar to oil-gas, automotive and energy industries tasks. The task of VLM optimization has been solved numerically in two steps iteratively. First was the simulation of supersonic steam flow that was an outlet to a vacuum. This type of task required simulation of a single-phase flow with supersonic velocities. The second step was the simulation of the phase change process with subsonic velocities in the VLM. This task required a multi-phase model that works well with subsonic velocities with a subcritical liquid-gas model (water-steam). These types of simulations may be computed using different CFD models. A brief review of the main models is presented in sections (3.6.1.1) and (3.6.1.2).

3.6.1.1 Single-Phase Supersonic Models

Modern CFD codes have well-tested supersonic models that work with RANS models. This work seeks to simulate supersonic steam flow at the outlet nozzle. A standard supersonic model is implemented into ANSYS-CFX in parallel, with a $k-\omega$ SST model was used.

3.6.1.2 Multi-Phase Subsonic Models

A RANS model was used in this work to simulate the subsonic part of a VLM with a phase change model because it has been well-developed and uses CFD code ANSYS-CFX. A multi-phase simulation is required to add some models for the phase interaction. For phase separation, ANSYS-CFX developed homogeneous and heterogeneous models. All phases are distributed in all simulated domains with some volume fraction in the homogeneous model. Two different approaches can be used for the heterogeneous model.

The first is a free surface model where surface tension is modelled. The second one is the MUSIG model, where the bubbles are divided into groups of bubbles that are widespread in the computed domain. The MUSIG model is statistical and high performance. The free surface model is numerically complex and accurate in representing bubble behaviour.

In ANSYS-CFX, additional models are used for phase change. A boiling model with standard parameters that show promising results in test simulations was used. A homogeneous multi-phase model was used in this work, with boiling phase change as one of the most numerically simple.

3.6.2 CFD Codes

Currently, hundreds of freeware and commercial solver codes, pre-post processors, visualizations, grid generation codes and system codes for CFD applications have been developed (a shortlist of CFD codes is presented at [76]). The most well-known and widely used freeware code is OpenFOAM, which has been developing since 2004 but still has limitations in pre-processing, post-processing and CFD models.

The most popular CFD codes for engineering applications are commercial ones. Widely used commercial CFD codes include ANSYS-CFX, ANSYS-Fluent, Siemens Simcenter Star-CCM+, COMSOL Multiphysics, and PHOENICS. In the range of commercial

CFD codes, leaders are ANSYS and Siemens products. Both allow researchers to simulate a wide range of multiphysics tasks, including multi-phase flows into the VLM. As there were available licenses for ANSYS products and the university computer cluster was set up to work with it, ANSYS was used to simulate hydrodynamics and heat transfer into the VLM.

During simulation, ANSYS products were used: Design Modeler to create high-quality 3D geometry; Meshing to create high-quality mesh; CFX that is the CFD code; CFD Post is the CFD postprocessor; Workbench was used to connect all ANSYS products in one single project. ANSYS has some different CFD codes. Currently, the most universal is CFX and FLUENT. CFX was used because it is more user-friendly and very stable during simulation. It has multi-phase support with boiling models. ANSYS 17.0 version was used in this project simulations.

3.6.3 Computational Resources

The simulations were done at the Central High-Performance Computing (HPC) resource at the University of Sheffield. In this computation, 48 inlet xeon computer cores. This centre can handle the intensive computing requirements of this project, and all the results of this thesis were performed in three months.

4 Numerical Implementation and Simulation Setup

4.1 Methodology of the VLM Simulation

The numerical simulation of the VLM was conducted by dividing the computational domain into two regions. First, is the simulation and optimization of the VLM outlet region, where the dry steam flows through the chamber and outlet nozzle using single-phase supersonic models.

Second, is the simulation and optimization of the VLM inlet part, which has four different zones: inlet, distributor, microchannels and a chamber using subsonic multi-phase models. The results of the numerical simulation of both the supersonic and subsonic regions are discussed in chapter (5).

4.2 Supersonic Region Simulation

4.2.1 Governing Equations

The governing equations of the supersonic flow are the mass, momentum, and energy conservation equations which are presented in expressions below:

Mass conservation:

$$\frac{\partial \rho}{\partial t} + \nabla \cdot (\rho \mathbf{U}_{tp}) = 0 \quad (4.1)$$

Momentum equation:

$$X - axis : \frac{\partial \rho u}{\partial t} + \nabla \cdot (\rho \mathbf{U}_{tp} u) = -\frac{\partial p}{\partial x} + \nabla \cdot (\mu \nabla u) \quad (4.2)$$

$$Y - axis : \frac{\partial \rho v}{\partial t} + \nabla \cdot (\rho \mathbf{U}_{tp} v) = -\frac{\partial p}{\partial y} + \nabla \cdot (\mu \nabla v) \quad (4.3)$$

$$Z - axis : \frac{\partial \rho w}{\partial t} + \nabla \cdot (\rho \mathbf{U}_{tp} w) = -\frac{\partial p}{\partial z} + \nabla \cdot (\mu \nabla w) \quad (4.4)$$

where:

- t is the time.
- $\mathbf{U} = \hat{u} + \hat{j}v + \hat{k}w$ is the velocity.
- tp is the subscript denotes mixture quantities
- ρ is the fluid density.
- P is the pressure.
- μ is the dynamic viscosity.

Energy conservation:

$$\frac{\partial(\rho h_0)}{\partial t} + \nabla \cdot (\rho \mathbf{U}_{tp} h_0) = \nabla \cdot (K \nabla T) + \frac{\partial p}{\partial t} \quad (4.5)$$

$$\begin{aligned}
 & + \left[\frac{\partial(u\tau_{xx})}{\partial x} + \frac{\partial(u\tau_{yx})}{\partial y} + \frac{\partial(u\tau_{zx})}{\partial z} \right] \\
 & + \left[\frac{\partial(u\tau_{xy})}{\partial x} + \frac{\partial(u\tau_{yy})}{\partial y} + \frac{\partial(u\tau_{zy})}{\partial z} \right] \\
 & + \left[\frac{\partial(u\tau_{xz})}{\partial x} + \frac{\partial(u\tau_{yz})}{\partial y} + \frac{\partial(u\tau_{zz})}{\partial z} \right]
 \end{aligned}$$

where:

- h_0 is the total enthalpy.
- K is the thermal conductivity of the material.
- T is the temperature.
- τ_{ij} is the viscous stress tensor.

Equation of State from the ideal gas law flow is:

$$p = \rho RT \tag{4.6}$$

where:

- R is gas constant (kJ/kg.K)

The major modelling assumptions for the supersonic simulation are summarized as follows:

- Steady-state simulation.

- Turbulent flow k- ω SST model.
- No-slip boundary condition.
- Gravity effect is neglected.
- Convective heat transfer.
- Ideal gas.
- Water and dry steam thermophysical properties were obtained from the IAWPS-CFX library.
- Initial conditions were set: Flow velocity 10 ($m.s^{-1}$); ambient pressure level 2500 Pa, temperature 383 K.

The k- ω SST turbulence model:

$$\frac{\partial}{\partial t}(\rho k) + \frac{\partial}{\partial x_i}(\rho k u_i) = \frac{\partial}{\partial x_j} \left(\Gamma_k \frac{\partial k}{\partial x_j} \right) + \tilde{G}_k - Y_k + S_k \quad (4.7)$$

$$\frac{\partial}{\partial t}(\rho \omega) + \frac{\partial}{\partial x_i}(\rho \omega u_i) = \frac{\partial}{\partial x_j} \left(\Gamma_\omega \frac{\partial \omega}{\partial x_j} \right) + G_\omega - Y_\omega + D_\omega + S_\omega \quad (4.8)$$

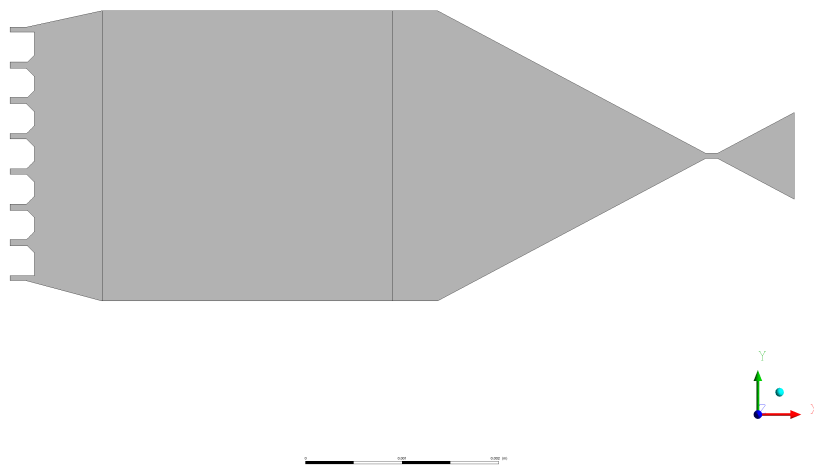
where:

- Γ_k is the effective diffusivity of k .
- \tilde{G}_k is the generation of turbulence kinetic energy due to mean velocity gradients.
- Y_k is the dissipation of k .
- S_k is user-defined source term.
- ω is the specific dissipation rate.
- Γ_ω is the effective diffusivity of ω .
- G_ω is the generation of ω .

- Y_ω is the dissipation of ω .
- D_ω is the cross-diffusion term.
- S_ω is user-defined source term.

4.2.2 Modification of the Geometry of the VLM Supersonic Region

Using numerical simulation for efficiency optimisation, Several vital parameters were investigated using numerical simulation to optimise output performance. The original geometry nozzle shape is optimised to maximise the thrust force and efficiency considering the viscous and thermal conduction effects in the gas and structure [15], [58]. Several possible geometries have been studied through an analysis performed using ANSYS-CFX to model the nozzle's flow. An image of the original 3D CAD model of a supersonic model is presented in Figure 4.1 below.



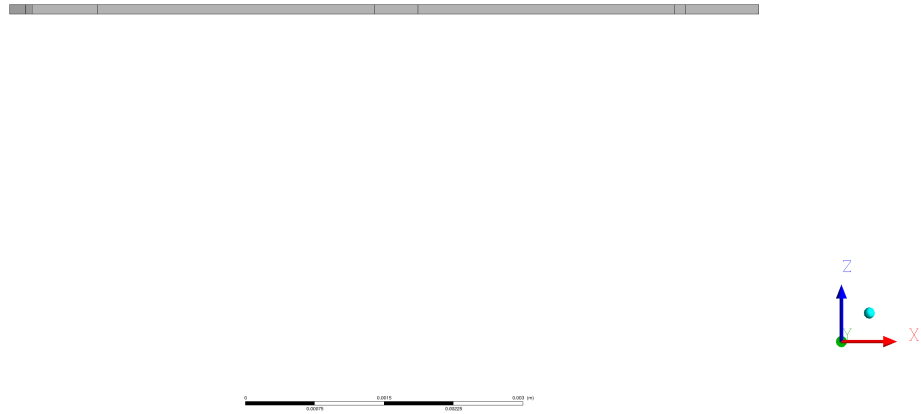


Figure 4.1: Top and side view image of the original CAD model of supersonic nozzle (V1).

The geometry of the original model of VLM was taken based on results in the literature data from [15]. It occurred that the microscale nozzle with a semi-divergence angle of 28° worked better compared to the macroscale configuration with a narrower angle of 15° to 20° according to [30]. In the present configuration, the semi-divergence angle of the microthruster exit nozzle was thus taken to be 28° as a starting design.

4.2.3 Mesh of the VLM Supersonic Region

The spatial domain of the supersonic region (VLM outlet part) is discretized by implementing unstructured tetrahedron elements. The mesh generation is subjected to several iterations to produce proper mesh. The quality of the mesh is examined based on the orthogonality, skewness factor, and aspect ratio. The computational domain of the single-

phase is divided into 1.36 million elements with 4.58 million nodes. Five prism boundary layers near the side-wall were constructed, the first layer height equal to 1.0×10^{-6} with an exponential growth rate coefficient equal to 1.35.

Since the tests would include extreme conditions such as supersonic speeds and strong shock waves, the mesh is required to handle the regions where the effects of high gradients of the primitive variables are expected. Consequently, the mesh is more refined in these regions.

A grid independence study was successfully performed on the mesh by doubling the number of grid points in each direction. The results show a negligible difference for the outlet thrust and for all the primitive variables (v , P , and T). Figure (4.2) below show the external mesh fragments and the internal cross-sections of the discretized domain.

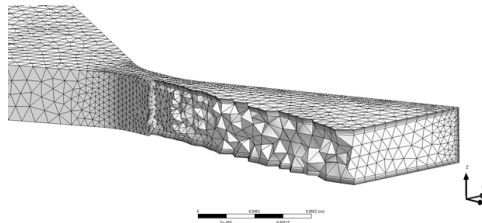


Figure 4.2: Lateral view of mesh fragment of supersonic region.

4.2.4 CFD Model Setup of the VLM Supersonic Region

The results of the numerical solutions were obtained by solving the equations of mass, momentum and energy conservation. Because the Knudsen number was less than 0.01 in all cases, the flow obeyed the no-slip boundary condition in this regard. The flow regime is turbulent, with Re approximately equal to 3000. The $k-\omega$ SST turbulence model was

implemented in this study to model turbulent flows where a significant proportion of the domain is laminar. The $k-\omega$ SST turbulence model is a two-equation eddy-viscosity model that is used for many industrial applications. It is a combining between the $k-\omega$ and the $k-\epsilon$ models. A blending function, $F1$, controls the activations of each model ($k-\omega$ or $k-\epsilon$). The blending function activates the $k-\omega$ model in the near wall region and $k-\epsilon$ for the free stream region [77], [78]. This ensures that the appropriate model is utilized throughout the flow field. The $k-\omega$ model performing well for simulating flow in the viscous sub-layer, especially in microchannels [79]. The $k-\epsilon$ model was proven to be perfect for predicting flow behaviour in regions away from the wall.

The flow was simulated as dry steam through the chamber and outlet nozzle. After the simulation of the outlet region had been completed, a pressure level inside the chamber was obtained. This pressure level was used to set the outlet pressure for multi-phase simulation of the inlet part of the VLM (the subsonic part).

Boundary conditions for these simulations are presented in Figure 4.3 below. Mass flow rate of the steam on the inlet part (1) was $2.0 \text{ mg}\cdot\text{s}^{-1}$. The temperature of the dry steam on the inlet part (1) of the chamber was set to 426 K. The ambient pressure level on the outlet part (2) of the thruster was set equal to 2500 Pa. The silicon side-wall heat flux was set equal to zero (adiabatic boundary conditions).

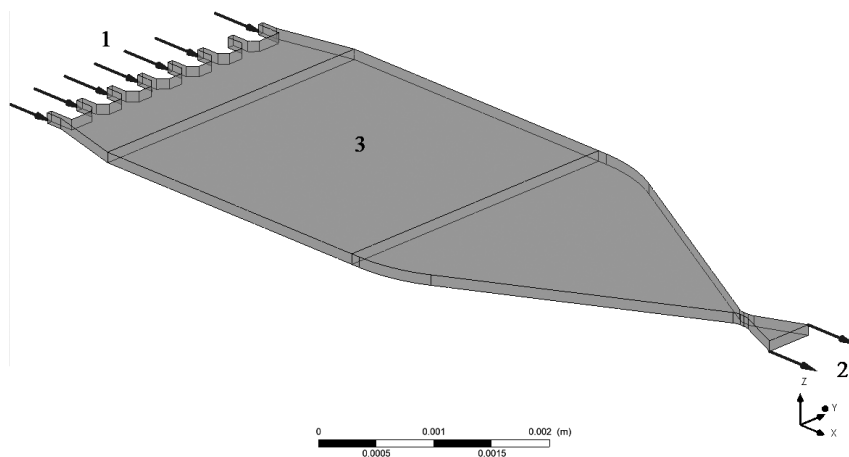


Figure 4.3: Boundary conditions for simulation of supersonic part of VLM.

4.3 Subsonic Region Simulation

4.3.1 Governing Equations

The multi-phase flow in the subsonic section is mathematically governed by the conservation equations of mass, momentum and energy of the mixture flow in addition to the void fraction equation.

The density of a homogeneous mixture (liquid-vapour) flow can be calculated by using the following equation.

$$\rho_{tp} = \sum_{i=1}^{i=n} x_i \rho_i = x \rho_g + (1 - x) \rho_f \quad (4.9)$$

While the viscosity of the mixture is considered as an empirical equation and it is a function of dryness fraction (x).

$$\mu_{tp} = \sum_{i=1}^{i=n} x_i \mu_i = x \mu_g + (1 - x) \mu_f \quad (4.10)$$

The mass conservation equation is given by the following expression

$$\frac{\partial}{\partial t}(\rho_{tp}) + \nabla \cdot (\rho_{tp} \mathbf{U}_{tp}) = 0 \quad (4.11)$$

The momentum conservation equation is given by the following expression

$$\frac{\partial}{\partial t}(\rho_{tp} \mathbf{U}_{tp}) + \nabla \cdot (\rho_{tp} \mathbf{U}_{tp} \cdot \mathbf{U}_{tp}) = -\nabla p + \nabla \cdot [\mu_{tp}(\nabla \mathbf{U}_{tp} + \nabla^T \mathbf{U}_{tp})] + S_M \quad (4.12)$$

where

S_m is the surface tension at the interface of two phase flow

The energy conservation equation is given by the following expression

$$\frac{\partial}{\partial t}(\rho_{tp} \cdot E_{tp}) + \nabla \cdot [\mathbf{U}_{tp}(\rho_{tp} \cdot E_{tp} + p)] = \nabla \cdot (k_{eff} \nabla T) + S_h \quad (4.13)$$

where

k_{eff} is the effective conductivity and can be defined by the equation

$$k_{eff} = \sum_{i=1}^{i=n} x_i k_i = x k_g + (1 - x) k_f \quad (4.14)$$

The mixture energy E_{tp} takes the form:

$$E_{tp} = \frac{x \rho_g E_g + (1 - x) \rho E_f}{\rho_{tp}} \quad (4.15)$$

The conservation equation of the volume fraction is given by the following expression

$$\sum_{i=1}^{i=n} x_i = 1 \quad (4.16)$$

$$\frac{\partial}{\partial t}(x_v \rho_v) + \nabla \cdot (x_v \rho_v \mathbf{U}_{tp}) = \sum_{\alpha=1}^{N_p} \Gamma_{fv} \quad (4.17)$$

where Γ_{fv} is the source term of mass transfer from one phase to another.

The numerical solution of the volume fraction equation (4.17) as well as the exact form of the source term in equation (4.13), S_h , containing contributions from volumetric heat sources, used the standard CFX implementation.

4.3.2 Modification of the Geometry of the VLM Subsonic Region

The subsonic region is split into four different zones: inlet, distributor, microchannels and chamber. This chapter is presented different geometries of the VLM subsonic part that were used during the optimization process with an explanation of modification reasons.

The main aim of VLM subsonic part optimization is to improve the overall efficiency of VLM thruster: reducing energy losses into the device and increasing boiling process efficiency. The original VLM model was created similar to those presented in other works [15], [58], and [80] . The geometry presented in Figure 4.4 below was used as a base model.

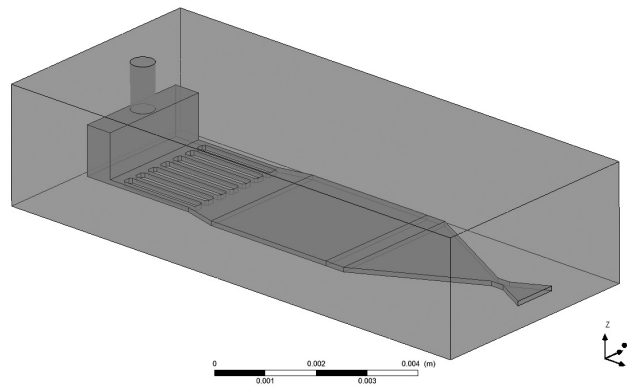


Figure 4.4: First concept model of the VLM subsonic region.

As a result of the first series of simulations with this model, an unstable flow into the chamber was observed with substantial under-heated water with lower than saturation temperature at the outlet region. Furthermore, there was a non-uniform mass flow rate through the parallel microchannels. In addition, the Silicon model temperature in the inlet part of VLM was very high, which may boil the water within the inlet part, giving rise to the inlet propellant pump functional failures.

To solve these problems, the geometry was modified. First, the thickness of the silicon model decreased to reduce the temperature of the silicon at the inlet region. The

second modification was to increase the length of the microchannel to enable boiling of the water at the desired temperature and more uniformly. Third, the distributor section volume decreased. The resulting geometry of the second model is presented in Figure 4.5 below.

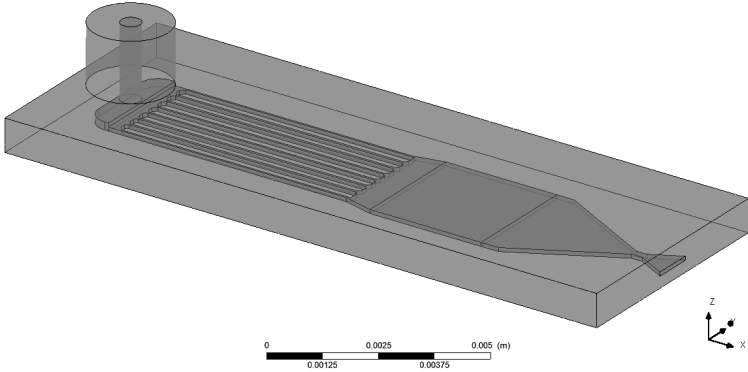


Figure 4.5: Second concept model of the VLM subsonic region.

Thus, the simulation results of the second model were much better, in that the temperature of the distributor section was decreased, and the volume fraction of the steam at the chamber outlet was increased. However, there was still much water in the chamber; also, it was observed boiling within the distributor section. Given this, the next modification was to increase the VLM length and decreased the distributor section volume. The resulting geometry is presented in Figure 4.6 below.

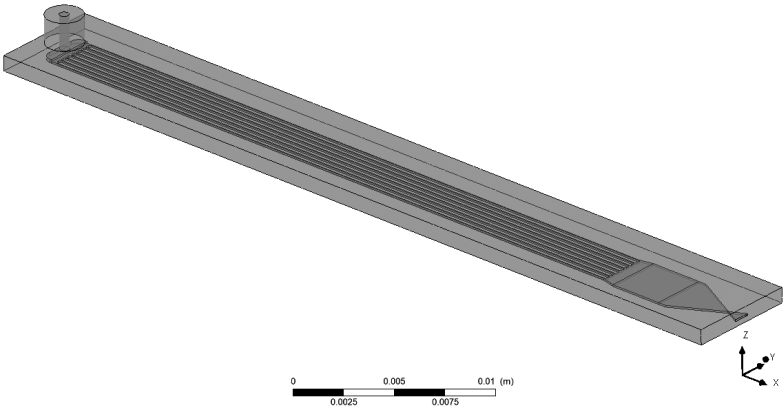


Figure 4.6: Third concept model of the VLM subsonic region.

In the third model, the temperature field in the silicon was close to the requirement, and the boiling started at the inlet of the microchannels. However, these were unstable conditions because the economizer region was in the distributor section. Additionally, the distribution of heat carrier mass flow rate in the microchannels was nonuniform. The boiling process started in different locations along the x-axis in the microchannels. For this reason, it was decided to slightly increase the length of the microchannels, adjust the microchannels inlet and outlet bevel and adjust the width of the microchannels to make the flow of water much more uniform and stable. The resulting model was highly optimized and is presented in Figure 4.7 below.

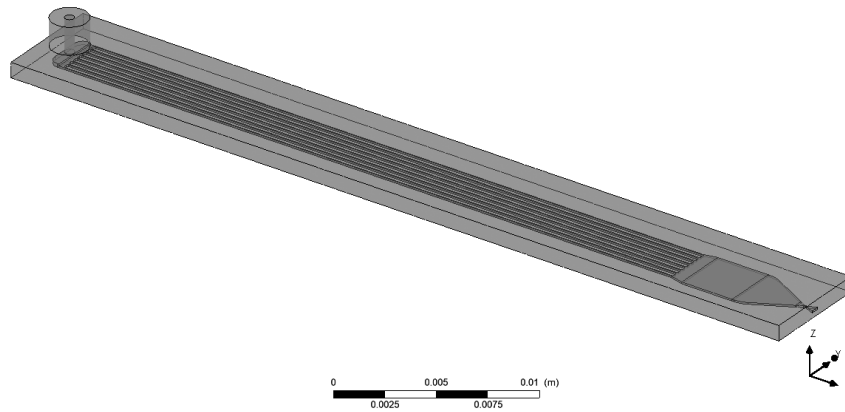


Figure 4.7: Forth concept model of the VLM subsonic region.

The subsonic part of the model's geometry was optimised. Consonantly, the proper temperatures of silicon were achieved as a result of the optimisation process. Furthermore, boiling of water in the VLMs inlet and distributor sections were avoided. In addition, the boiling of water inside microchannels was stabilised. Moreover, a near-uniform distribution of mass flow rate between microchannels was achieved. Additionally, the volume fraction of water on the nozzle inlet was found to be close to zero. A schematic diagram of the optimised VLM thruster (subsonic and supersonic parts are united) is illustrated in Figure 4.8 as well, as the dimensions of the different components of the optimised VLM values are summarised in Table 4.1 below.

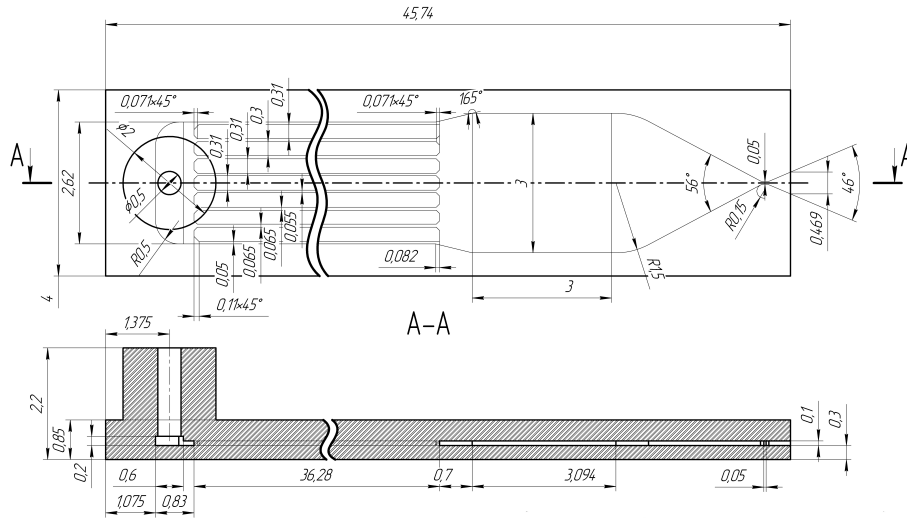


Figure 4.8: Top and side view of schematic diagram of the optimized VLM thruster (dimension in mm).

Table 4.1: The geometrical dimensions of the thruster subsonic region.

Components	Dimensions (μm)		
	l	w	h
Inlet channel		500	1700
Distributor	830	2620	200
8 Microchannels and 7 separators	36280	50-65 300-310	100
Vaporizing chamber	3000	3000	100

4.3.3 Mesh of the VLM Subsonic Region

For the subsonic model, the computational domain is subdivided into two domains. The first domain, which contains the silicon, is discretized to 3.8 million nodes. The second domain, which contains the water, is discretized to 3.4 million nodes. In total, the subsonic region is divided into 30 million elements with 7.2 million nodes. The refinement of the mesh is applied according to the Re with a y^+ value less than unity for all cases. Near

the wall, refinement is applied by implementing five prism boundary layers with first layer height equal to a 2.0×10^{-6} m and exponential growth rate with coefficient equal to 1.25. Figures (4.9), (4.10) and (4.11) below show the external mesh fragments and the internal cross-sections of this simulation model. Similar to the supersonic regions, the independent mesh study was performed by doubling the grid points in each direction, and the results showed no significant changes in the values of the primitive variables.

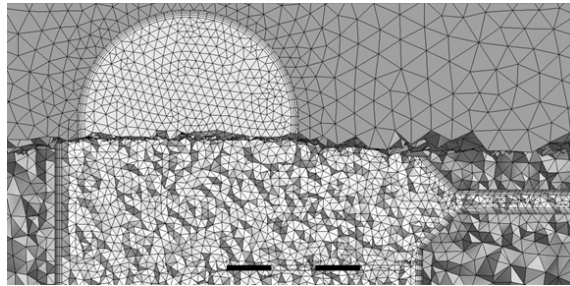


Figure 4.9: Top view of mesh fragment of subsonic region at the inlet.

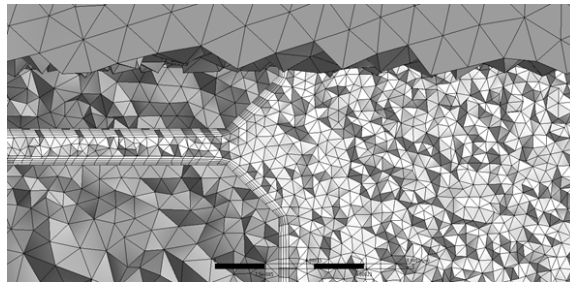


Figure 4.10: Top view of mesh fragment of subsonic region at microchannels outlet.

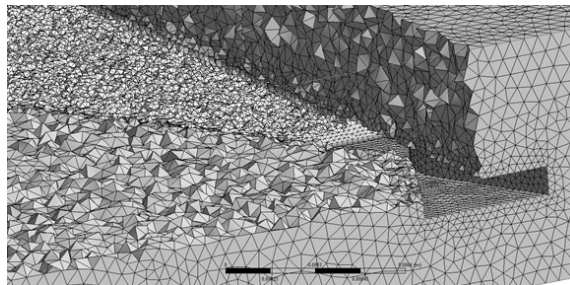


Figure 4.11: Lateral view of mesh fragment of subsonic region at nozzle exit.

4.3.4 CFD model Setup of the VLM Subsonic Region

The results of the numerical solutions were obtained by solving the equations of mass, momentum and energy conservation. In this respect, the flow followed the no-slip boundary condition on the side-walls since the Knudsen number was less than 0.01 for all cases. During simulation in the subsonic region, the flow will be in laminar flow mode. The flow was simulated as a multi-phase simulation through the subsonic part of the VLM thruster.

Boundary conditions of the numerical simulations are presented in Figure 4.12 below. The mass flow rate of the water on the inlet part (1) was $2.0 \text{ mg}\cdot\text{s}^{-1}$. The temperature of the water on the inlet section was equal to 293 K. The pressure level at the outlet (2) was set to 0.26 MPa to match the input of the supersonic simulations. On the internal side-walls of the chamber (4), the wall heat flux was set constant with different heating power 3.6 W, 2.3 W and 2.0 W applied to the heater section. The silicon side-wall (3) wall heat flux was set equal to zero (adiabatic boundary conditions).

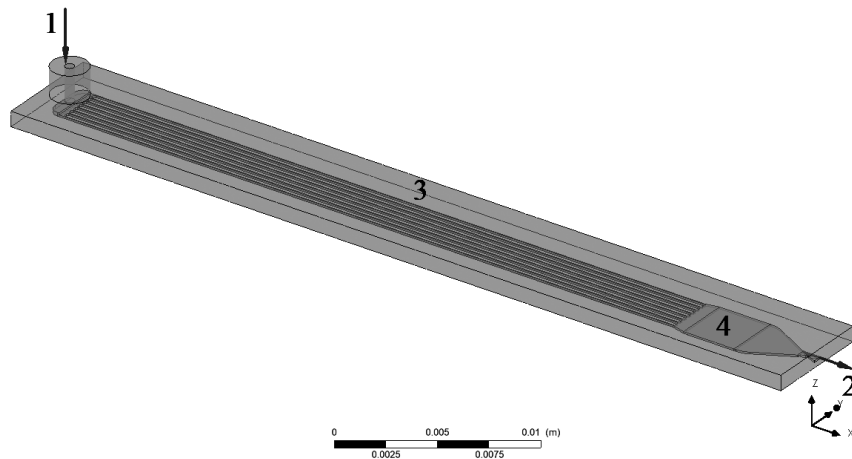


Figure 4.12: Boundary conditions locations for subsonic simulation.

The major modelling assumptions for the subsonic simulation are summarized as follows:

- Steady-state simulation;
- Turbulent flow $k-\omega$ SST model.
- Convective heat transfer.
- Conductive heat transfer into the silicon.
- Zero thermal contact resistance between liquid and solid.
- No-slip boundary condition.
- Ideal gas.
- Gravity effect is neglected.
- Water and dry steam thermophysical properties were obtained from the IAWPS-CFX library.
- Initial conditions were set:
Flow velocity $0.1 \text{ (}m.s^{-1}\text{)}$; ambient pressure level 2500 Pa, temperature 293 K, steam volume fraction (0-Inlet part and microchannels; 1-chamber and outlet nozzle).

5 Results and Discussions

5.1 Results of the VLM Supersonic Region Simulation

The original geometry model (V1) was not the best possible design, and for this reason, the shape of the nozzle divergent part has been changed. During the optimization process, the divergence angle, the shape of the divergence part side-wall, length of the divergence part nozzle were altered. So in series of numerical simulations and optimization processes, were used geometries that are shown in Figures (5.1) to (5.10) below.

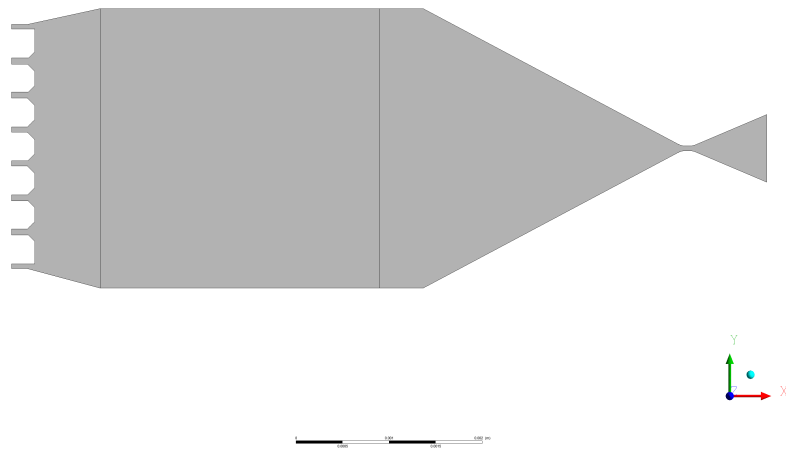


Figure 5.1: Top view image of 1st modification model of supersonic nozzle (V2).

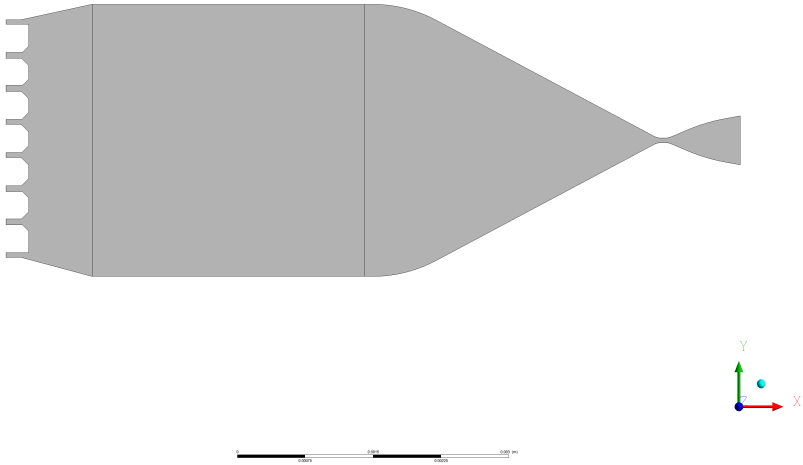


Figure 5.2: Top view image of 2nd modification model of supersonic nozzle (V3).

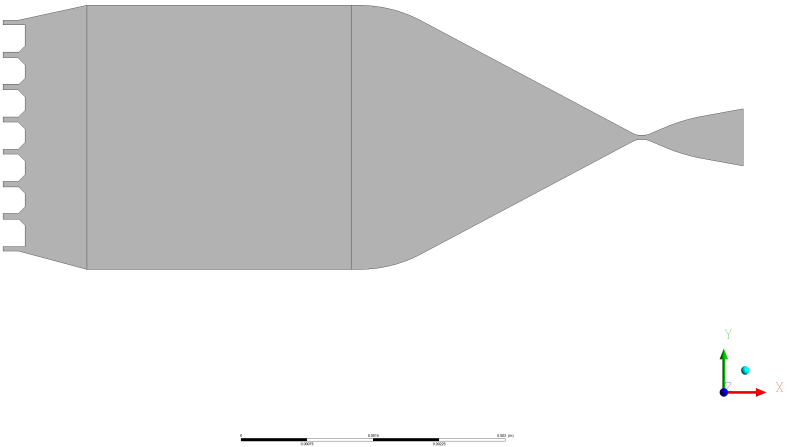


Figure 5.3: Top view image of 3rd modification model of supersonic nozzle (V4).

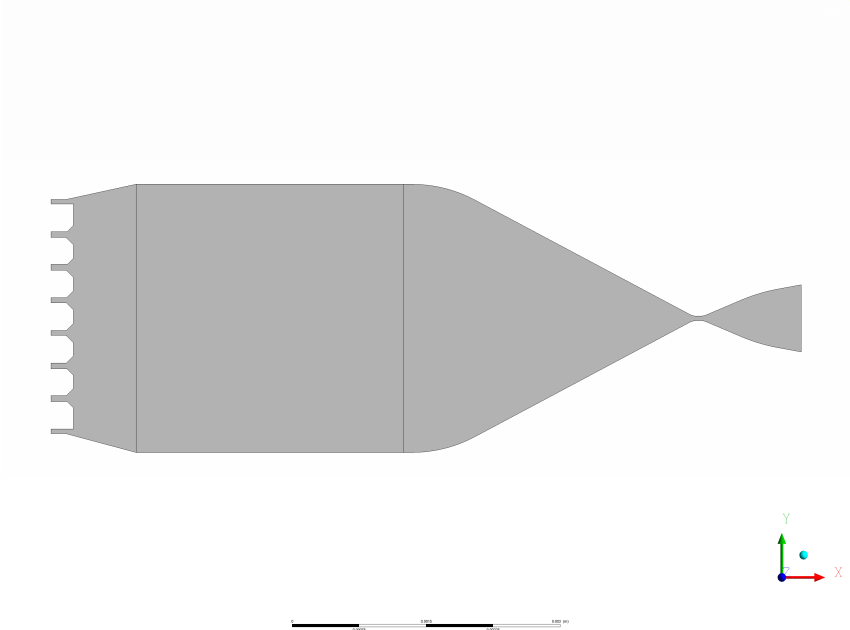


Figure 5.4: Top view image of 4th modification model of supersonic nozzle (V5).

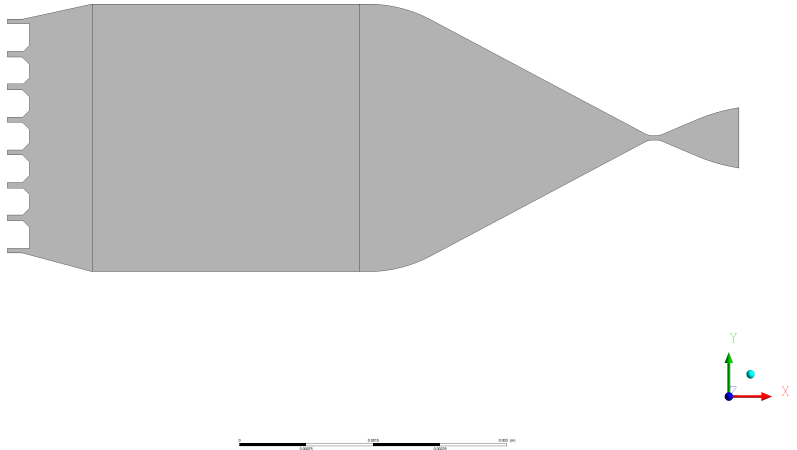


Figure 5.5: Top view image of 5th modification model of supersonic nozzle (V6).

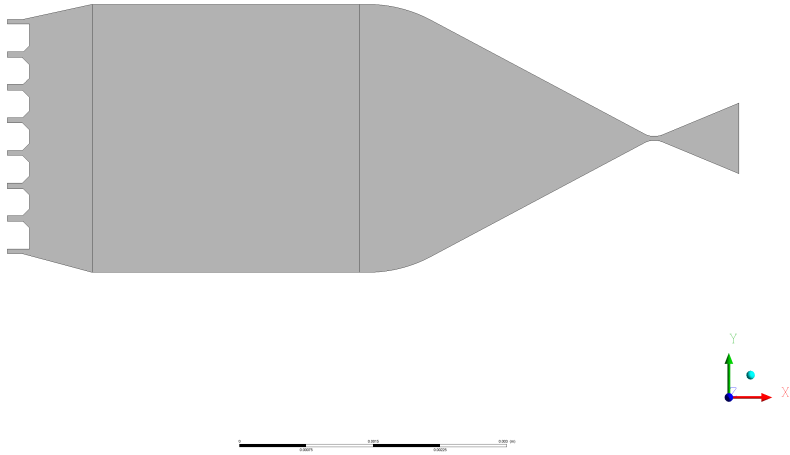


Figure 5.6: Top view image of 6th modification model of supersonic nozzle (V7).

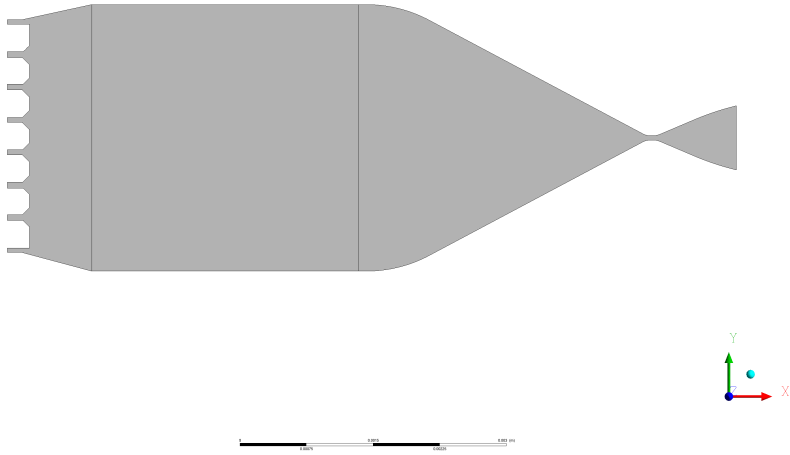


Figure 5.7: Top view image of 7th modification model of supersonic nozzle (V8).

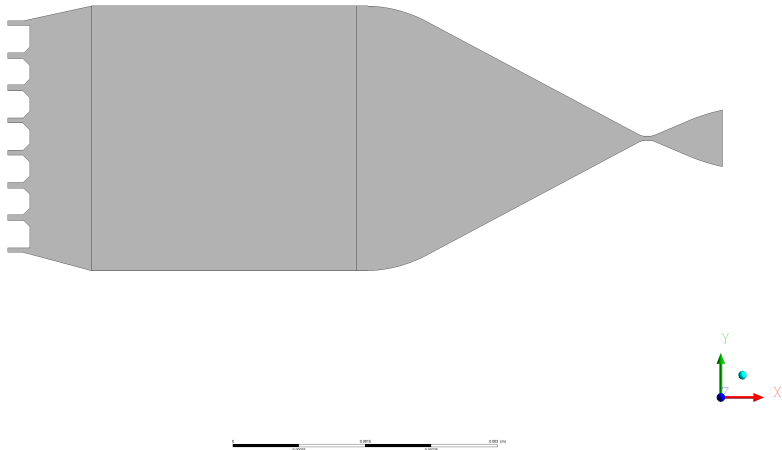


Figure 5.8: Top view image of 8th modification model of supersonic nozzle (V9).

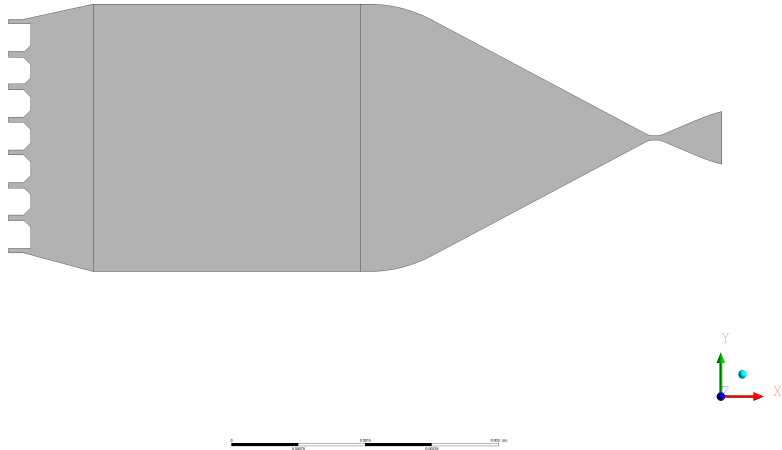


Figure 5.9: Top view image of 9th modification model of supersonic nozzle (V10).

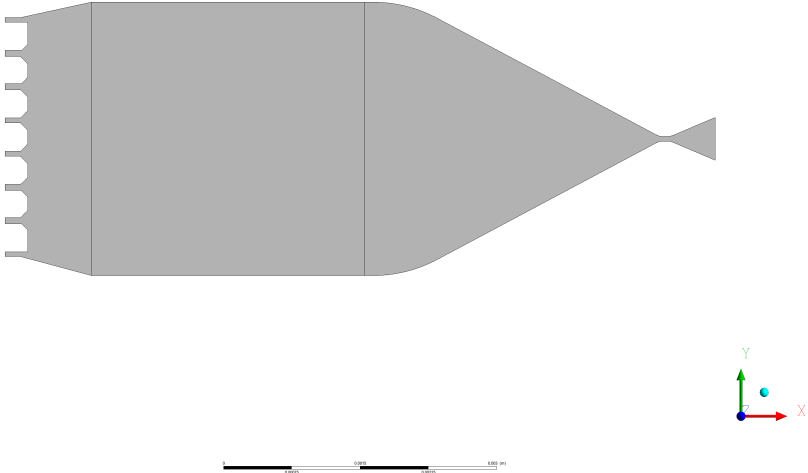


Figure 5.10: Top view image of 10th modification model, the most optimal geometry of supersonic nozzle (V11).

During optimization, simulations tested geometries with the curved side-wall shape that might reduce flow separation at the nozzle, as seen in Figures (5.2) to (5.5). As a result of these simulations, the flow separation disappeared, but the total thrust force decreased. Given this, final optimization calculations used a straight side-wall, and only the length of the diverged part of the nozzle was changed. The balance between the acceleration of the flow, energy loss of the side-wall and sufficient outlet cross-section area (to increase total thrust force) resulted in optimized VLM geometry. The optimized VLM supersonic regions dimensions is summarized in table 5.1 below.

Table 5.1: The VLM supersonic regions geometrical dimensions.

Components	Dimensions (μm)		
	l	w	h
Inlet area	550	550	100
throat area	50	50	100
Exit area	525	469	100 for $A_r = 9.3$
Semi-convergent angle	28°		
Semi-divergent angle	23°		

The most optimal simulation results model of the VLM supersonic region is geometry code (V11.2), and the rest of the model results can be found in Appendix A of this thesis. The numerical simulation was conducted under the following parameters:

- Constant mass flow rate through the nozzle equal to 2.0 mg.s^{-1} .
- Inlet area of the nozzle (cross-section area of the chamber) was constant and equal to 0.3 mm^2 .
- Total angle of the subsonic confuser was constant in all simulations and equal to 56° .
- Cross-section area of the sonic part of the nozzle was constant and equal to 0.005 mm^2 .

Dimensions of the nozzle, characteristic data and numerical results of the simulation are presented in Tables (5.2), (5.3), (5.4) and Figures (5.11) to (5.18) below.

Table 5.2: Numerical data of the nozzle simulation.

Geometry code No.	Nozzle outlet area, (mm^2)	Nozzle outlet ratio, A_r	Supersonic divergent total angle, (degree)	Supersonic divergent, length, (mm)	Subsonic/supersonic convergent transition curve radius, (mm)	Subsonic convergent inlet curve radius, (mm)
V11.2	0.0469	9.3	46 °	0.50	0.1	1.0

Table 5.3: Numerical data of the nozzle simulation at chamber inlet.

Geometry code No.	Bulk temperature, (K)	Average velocity, ($m.s^{-1}$)	Average Mach number	Static pressure, (Pa)	Total pressure, (Pa)	Density, ($kg.m^{-3}$)
V11.2	426	31.3	0.06	262869	263535	1.337

Table 5.4: Numerical data of the nozzle simulation at nozzle outlet.

Geometry code No.	Bulk temperature, (K)	Average velocity, ($m.s^{-1}$)	Average Mach number	Static pressure, (Pa)	Total pressure, (Pa)	Density, ($kg.m^{-3}$)	Thrust, (mN)
V11.2	238	751	2	5542	117331	0.047	1.38

As illustrated in Figures (5.11) to (5.18) below, contours of pressure, velocity, Mach no., temperature and density fields in longitudinal cross section between two boundaries of the most optimised model researched, geometries code V11.2.

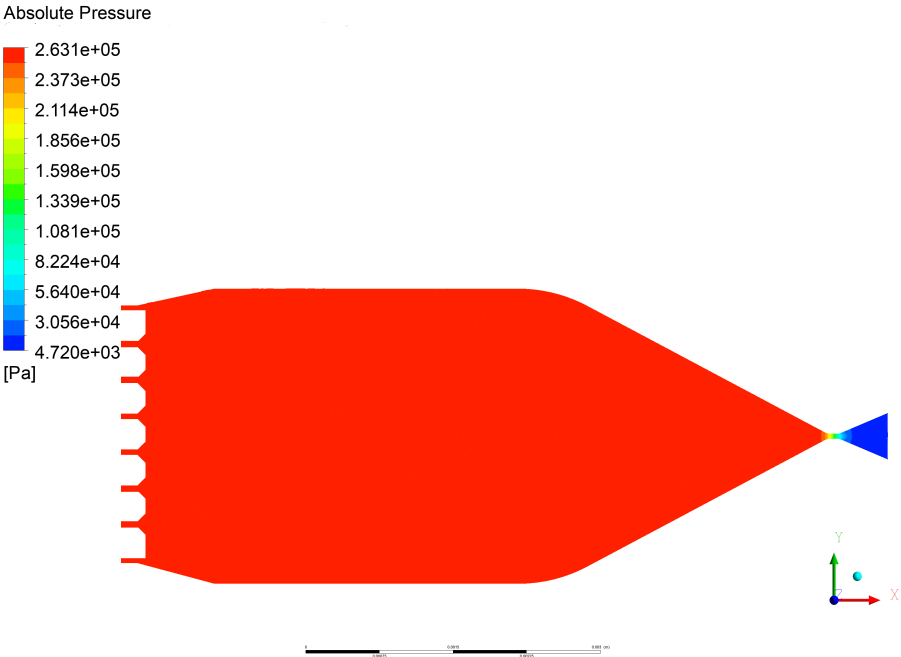


Figure 5.11: Absolute pressure distribution into thruster of supersonic model.

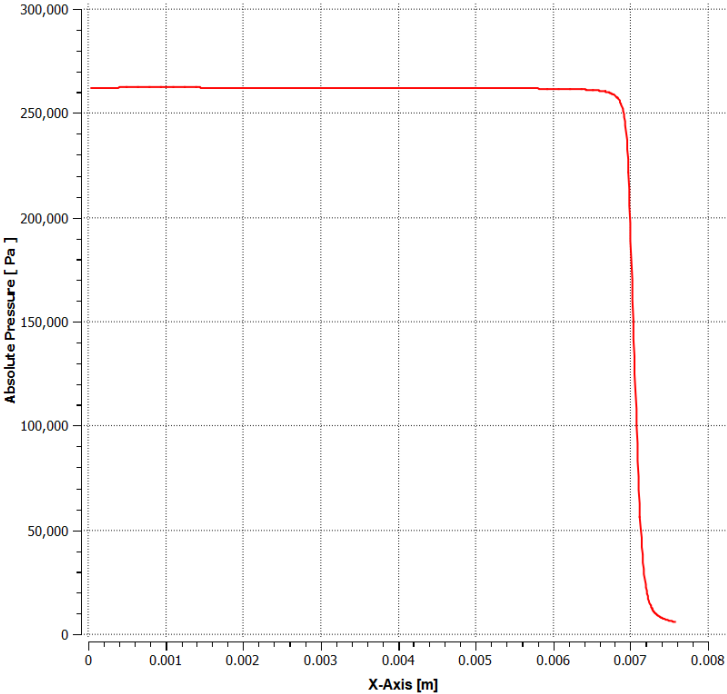


Figure 5.12: Absolute pressure distribution along thruster x-axis.

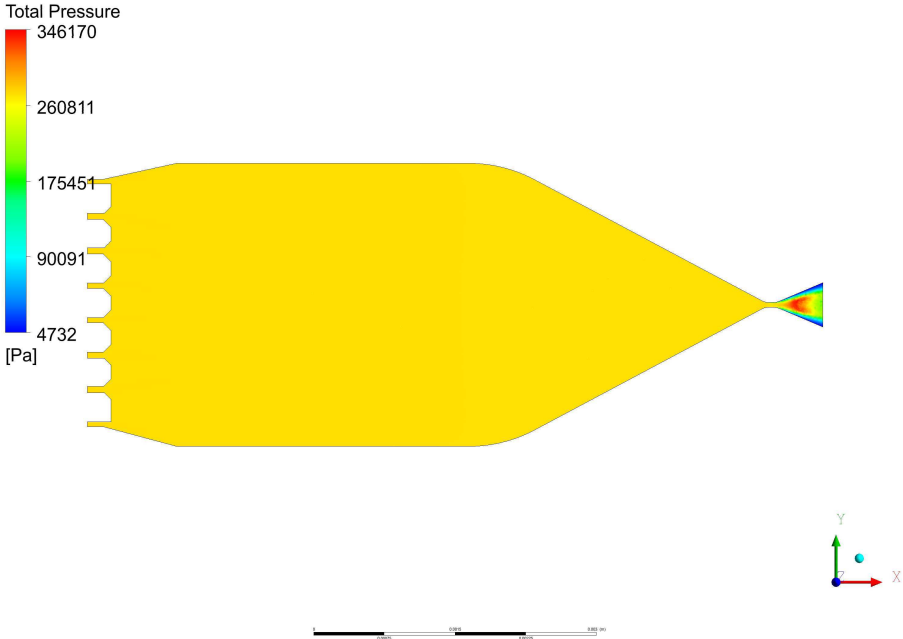


Figure 5.13: Total pressure distribution into thruster of supersonic model.

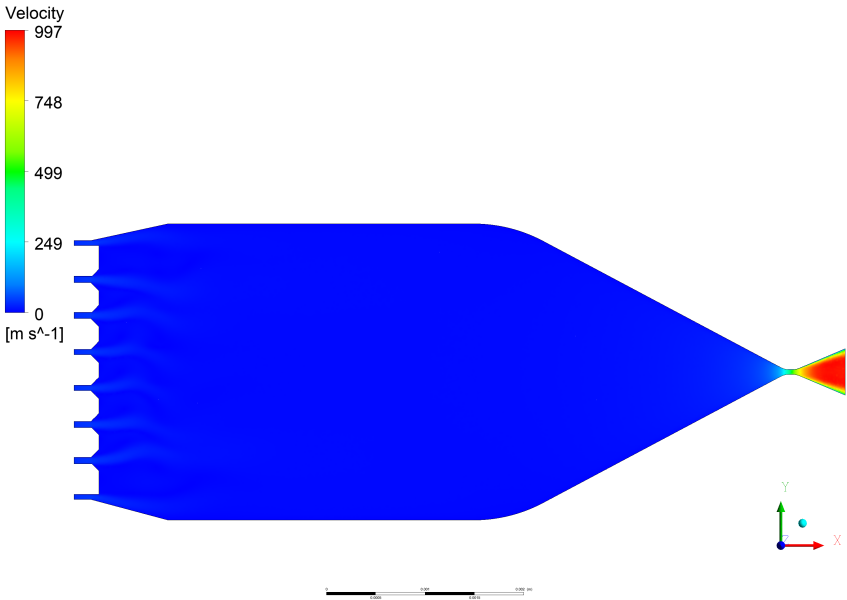


Figure 5.14: Fluid velocity distribution into thruster of supersonic model.

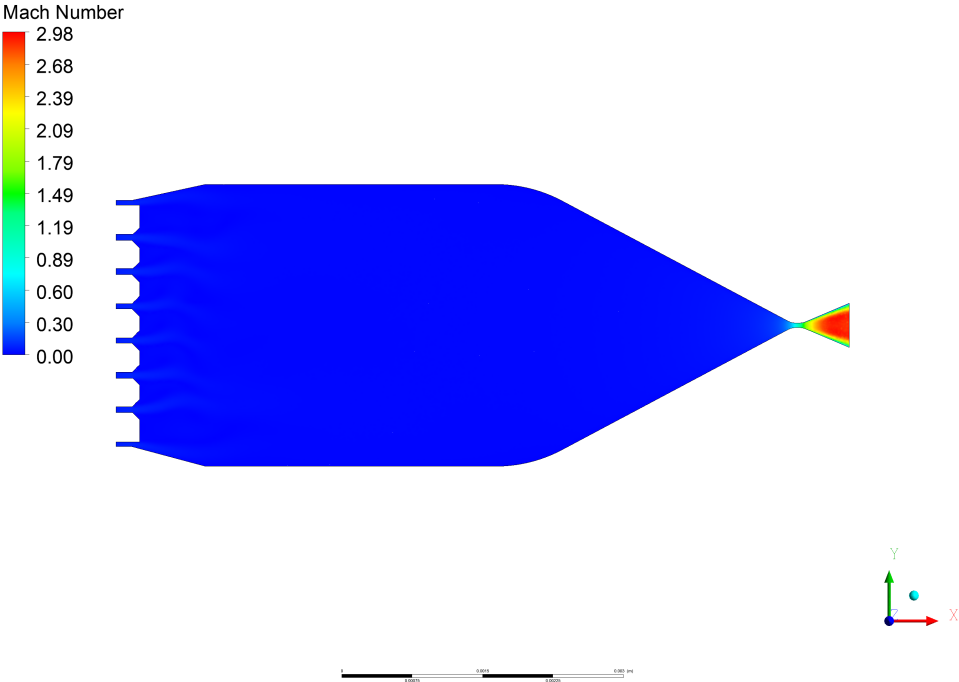


Figure 5.15: Fluid Mach number distribution into thruster of supersonic model.

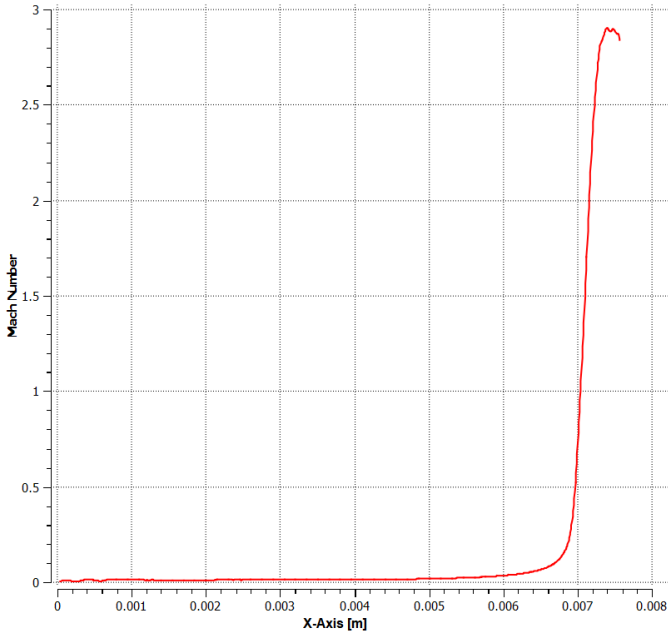


Figure 5.16: Mach number along nozzle x-axis.

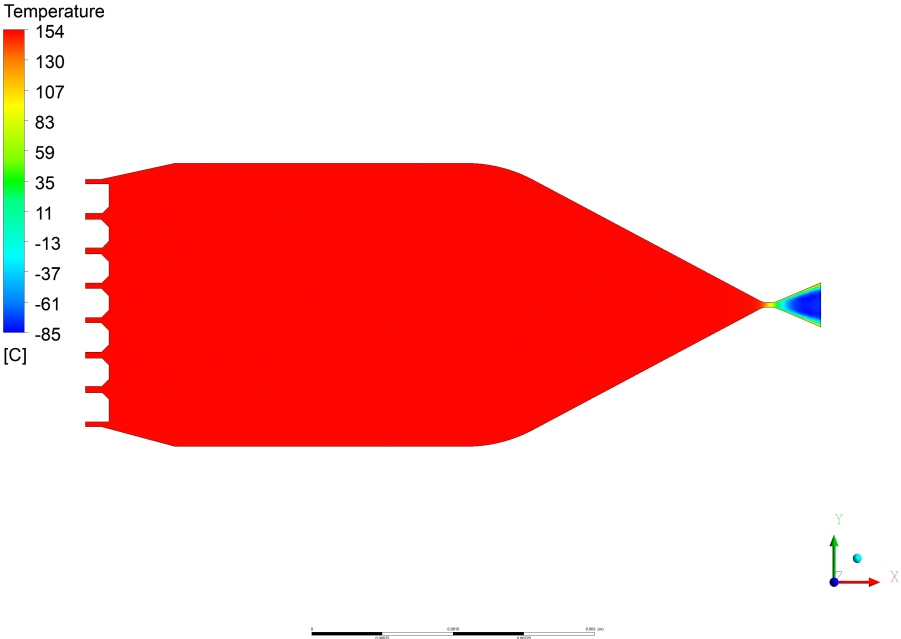


Figure 5.17: Temperature distribution into thruster of supersonic model.

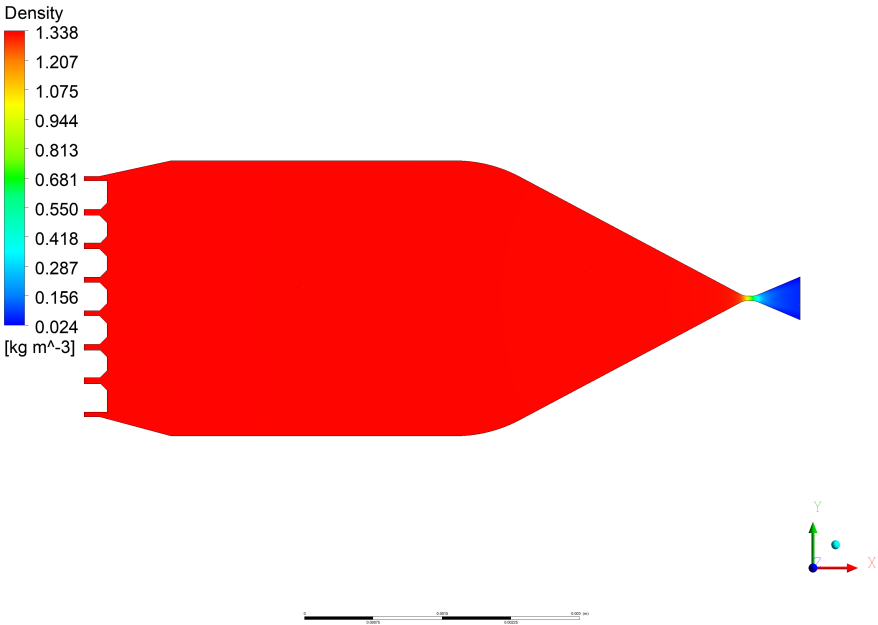


Figure 5.18: Density distribution into thruster of supersonic model.

5.2 Analyzing of the VLM Supersonic Region Simulation

An array of simulations of the VLM supersonic region has been computed with different geometries and constant mass flow rate, as shown in Appendix A. The aim of these simulations was an optimization of the in-plane supersonic nozzle shape. As a result of simulations, the nozzle's optimal shape (geometry code V11.2) was obtained with maximum thrust force and efficiency.

During the optimization process, the first parameter optimized is the balance of total enthalpy loss by friction on the side-wall of the nozzle and acceleration of the flow into the nozzle by adjusting the nozzle length. The second parameter is connected with removing the flow separation zones that lead to kinetic energy dissipation. For this reason, the nozzles side-wall shape and angle were optimized.

For the optimal shape of the outlet nozzle, the convergent angle of the nozzles subsonic region is equal to 56° , and the divergent angle for the supersonic region is equal to 46° . A portion of the nozzle throat, with a length of $50 \mu\text{m}$, was added for smooth flow transition from the subsonic to the supersonic region to stabilize the flow. The length of the supersonic nozzle region was 0.5 mm , with a total height of 0.1 mm .

Distribution of the absolute and total pressure into the fluid inside the chamber and outlet nozzle is seen in Figures (5.11), (5.12) and (5.13). The flow into the chamber is close to constant pressure between the inlet part of the chamber and the boundary of the converging part of the nozzle. After that, at the nozzle throat area, the pressure is decreased. The absolute pressure decreases sharply up to the exit point afterwards.

Figure (5.14) illustrates the distribution of fluid velocity in the nozzle region. The vapour velocity tends to rise at the converging side of the nozzle and reaching a value of 480 m.s^{-1} at the throat region. At the nozzle exit area, the overall flow velocity was $1.0e^3 \text{ m.s}^{-1}$. The Mach number variance in the nozzle region is illustrated in Figure (5.15).

The Mach number at the throat region was 1.0 as expected, and the maximum simulated Mach number was 3 at the nozzle exit location as illustrated in Figures (5.15) and (5.16).

The temperature distribution in the nozzle region is shown in Figure (5.17). Notably, the temperature in the nozzle exhaust drops to 190 K. As the multi-phase flow is not taken into account, the CFD solver still considers it as gas, but solid ice particles are likely to form, meaning it is still a problem to further examine the condensation and even solidification of the water in the exhaust during the test phase. Density is close to constant throughout the subsonic part of the chamber and reduced at the nozzle throat, as shown in Figure (5.18).

The thrust value determined by CFD analysis was 1.38 mN with a 70 s specific impulse. As a result of optimization compared with the original geometry was achieved. Resulted thrust force being 1.38 mN at 426 K and a constant flow rate of $2.0 \text{ mg}\cdot\text{s}^{-1}$.

5.3 Results of the VLM Subsonic Region Simulation

The simulations of the VLM supersonic part maximum thrust were obtained in geometry code (V11.2). Those results were set as the boundary conditions for the simulation of the VLM subsonic part. The pressure level on the inlet boundary of the nozzle was used as the inlet pressure level for the subsonic part. The pressure was set for the inlet part of the subsonic model instead of the outlet part for the following reasons. The first is connected with the fact that the simulation is more stable with a pressure boundary condition on the inlet part and a mass flow boundary condition on the outlet part.

The second reason is connected with the fact that the relative pressure drops on the subsonic part of the VLM by about 5%. The pressure level affects steam-water properties and saturation temperature. Furthermore, the pressure drop is only 5% which does not have a sufficient impact on the liquid thermal physical properties.

The simulation of the subsonic part was iterative. The aim of the iterative

simulation was connected with the requirements to obtain a temperature on the outlet of the microchannel, similar to the inlet of the supersonic part model simulation close to 426 K, and the requirements to achieve a stable solution. Three modes of heat power were used: 3.6 W, 2.3 W and 2 W. As a result of the VLM subsonic part simulations, the optimal heat power to obtain conditions similar to (V11.2) supersonic part simulations is 2.0 W mode. The 2.8 W and 3.6 W modes simulations results are presented in Appendix B of this thesis.

The temperature distribution in the nozzle region is shown in Figure (5.17). Notably, the temperature in the nozzle exhaust drops to 190 K. As the multi-phase flow is not taken into account, the CFD analysis still considers it gas. However, solid ice particles are likely to form, which is still a problem to further examine the condensation and even solidification of the water in the exhaust during the test phase. Density is close to constant throughout the subsonic part of the chamber and reduced at the nozzle throat, as shown in Figure (5.18).

The thrust value determined by CFD analysis was 1.38 mN with a 70 s specific impulse. As a result of optimization compared with the original geometry was achieved. Resulted thrust force being 1.38 mN at 426 K and a constant flow rate of $2.0 \text{ mg}\cdot\text{s}^{-1}$.

In Table (5.5) and contours, Figures (5.26), (5.20), (5.21), (5.22), (5.29), (5.27), (5.28), (5.25), (5.19) and (5.23) below were presented results of numerical simulation of the multi-phase subsonic part of the VLM with 2 W heat power like pressure, steam volume fraction, water volume fraction, silicon temperature, thruster inlet and outlet pressure, thruster steam volume fraction and outlet area-averaged steam volume fraction.

Table 5.5: Numerical data of the VLM subsonic model simulation at heat power 2 W.

Location	Modle inlet	Microchannels inlet	Microchannels cross-section average plane	microchannels outlet	Model outlet
Steam bulk temperature, (K)	405	405	404	426	423
Water bulk temperature,(K)	294	342	373	413	419
Velocity, ($m.s^{-1}$)	2×10^{-16}	3×10^{-9}	2×10^{-8}	1.3	2.0
Static pressure,(Pa)	252500	252382	246559	243095	243037
Total pressure, (Pa)	252505	254979	246670	243226	243140
Density, ($kg.m^{-3}$)	998	978	959	17	21
Steam volume fraction	2×10^{-15}	1×10^{-8}	3×10^{-8}	0.983	0.978

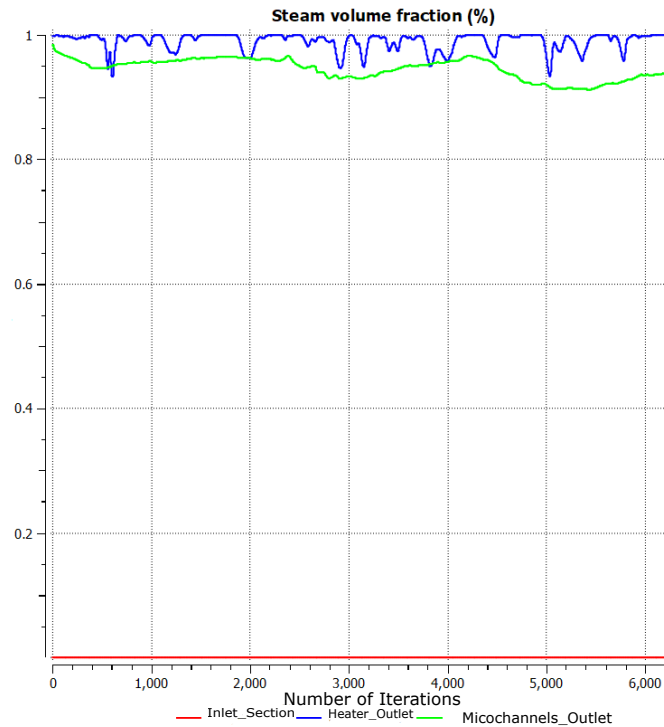


Figure 5.19: Thruster, steam volume fraction of subsonic model.

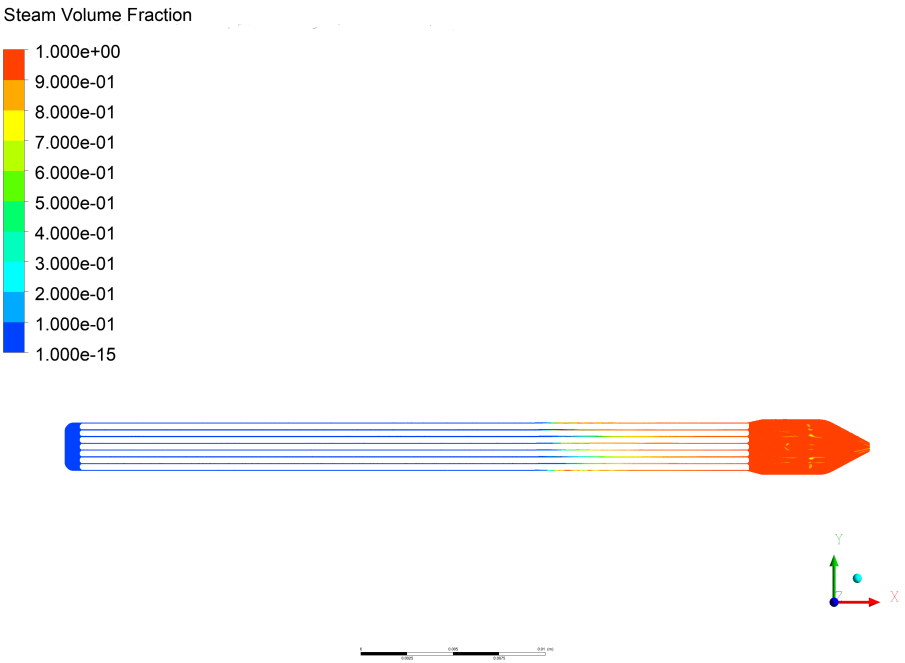


Figure 5.20: Steam volume fraction into thruster of subsonic model.

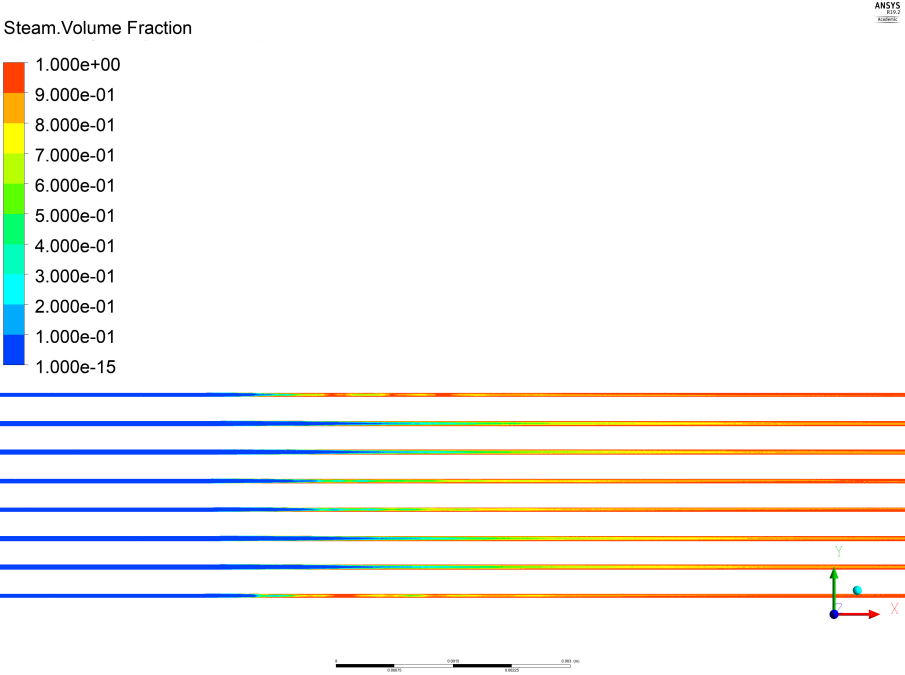


Figure 5.21: Steam volume fraction, zoom-in into the middle of microchannel region.

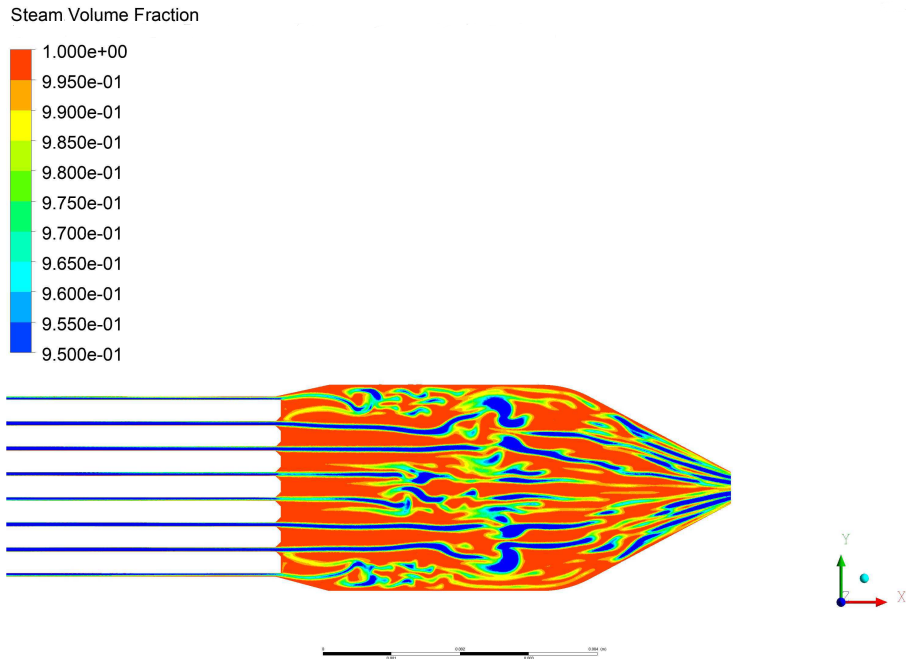


Figure 5.22: Steam volume fraction, into the chamber region.

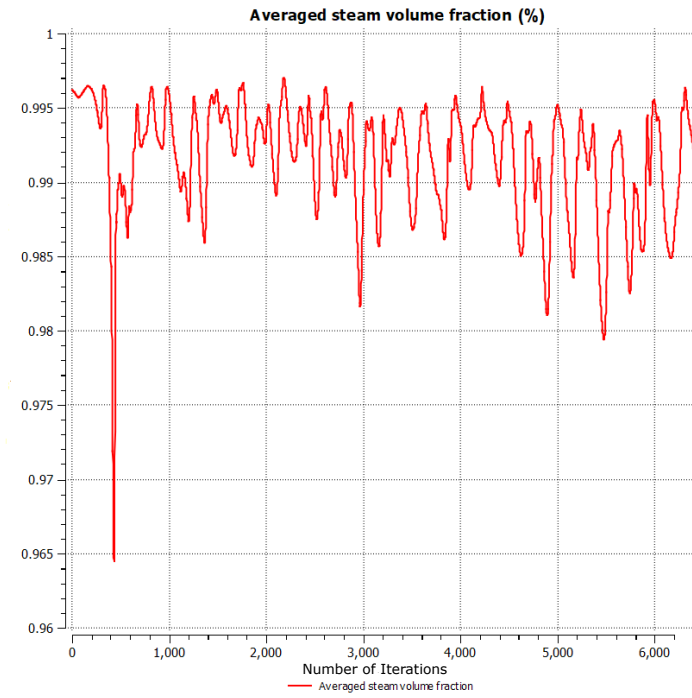


Figure 5.23: Chamber outlet area, averaged steam volume fraction .

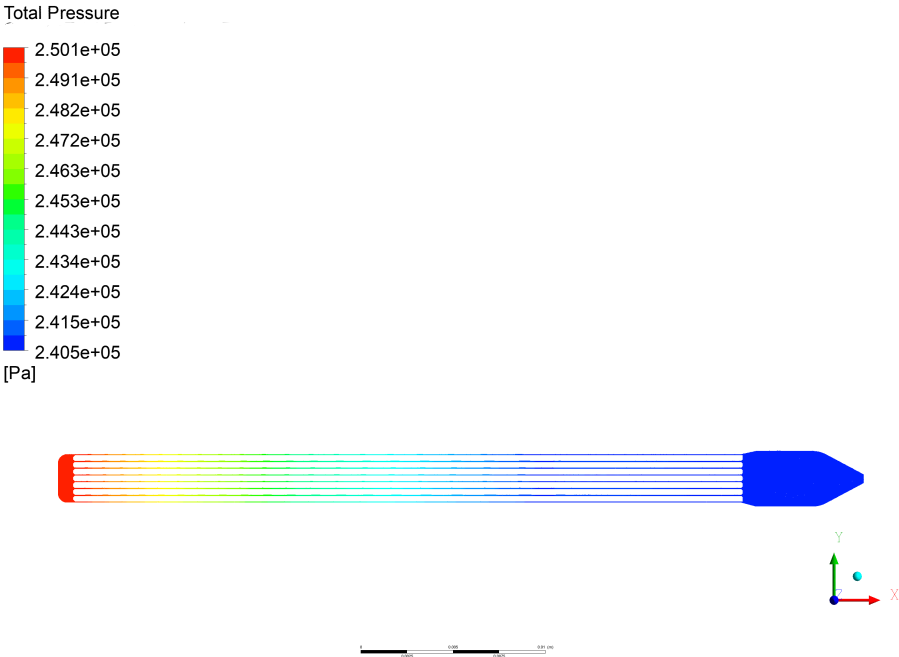


Figure 5.24: Total pressure distribution into thruster of subsonic model.

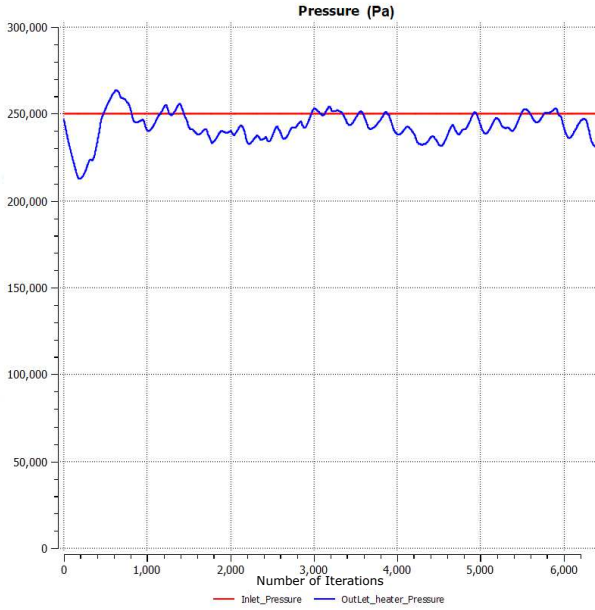


Figure 5.25: Thruster, inlet and outlet average total pressure.

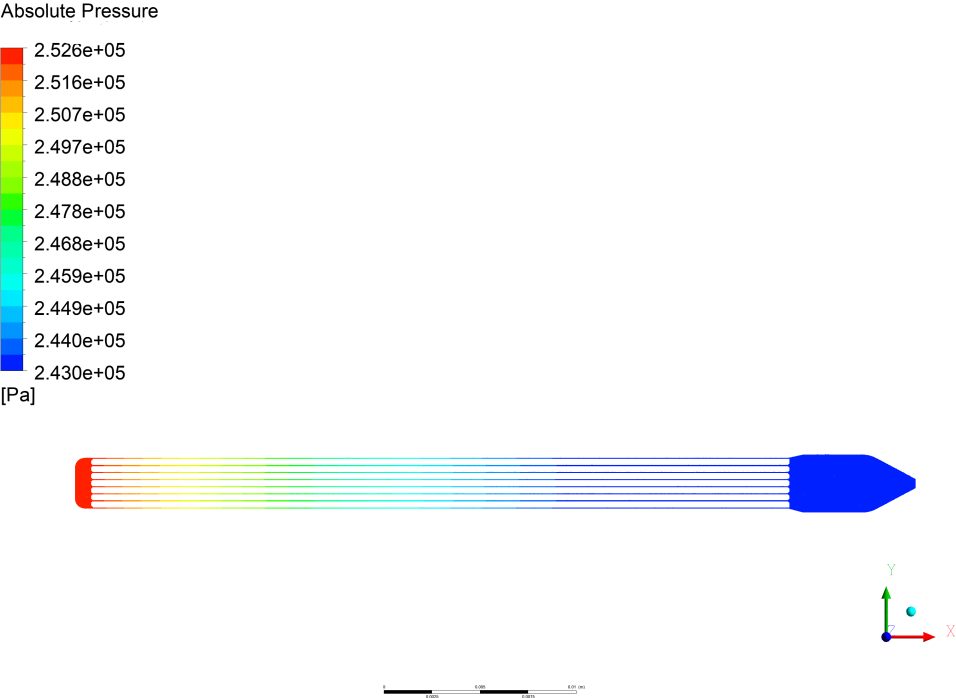


Figure 5.26: Absolute pressure distribution into thruster of subsonic model.

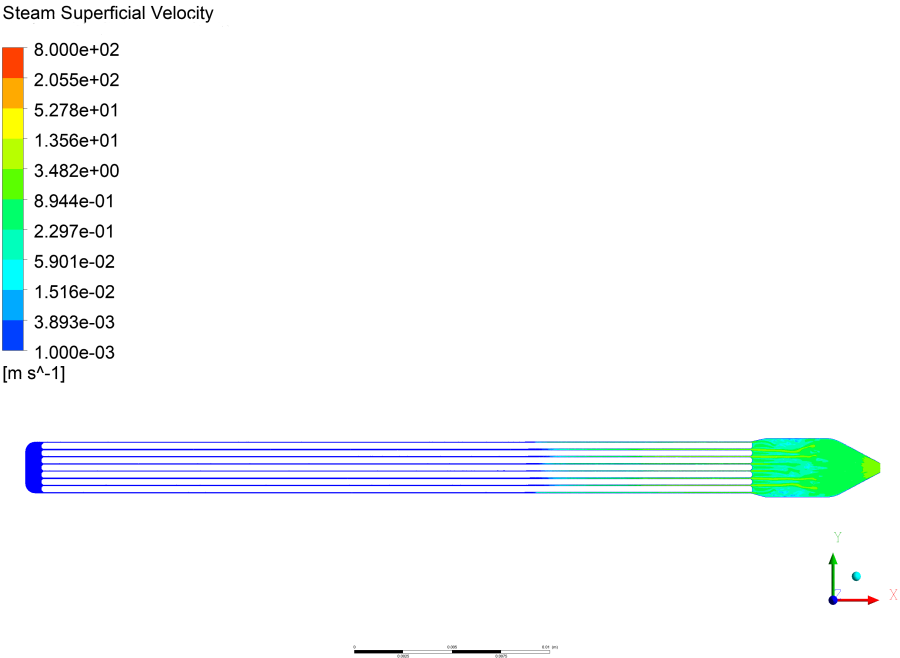


Figure 5.27: Velocity distribution into thruster of subsonic model.

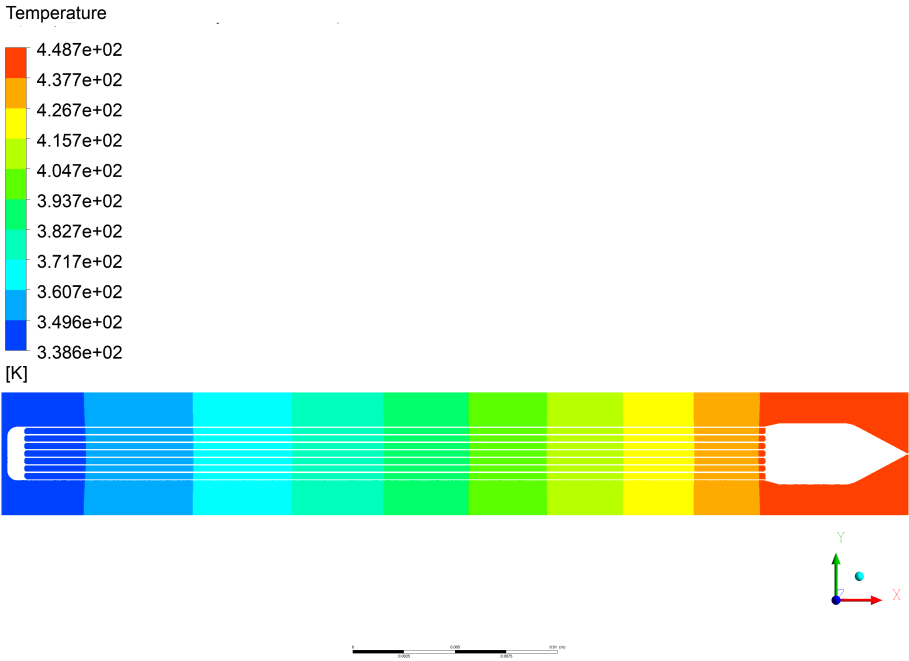


Figure 5.28: Silicon temperature of subsonic model.

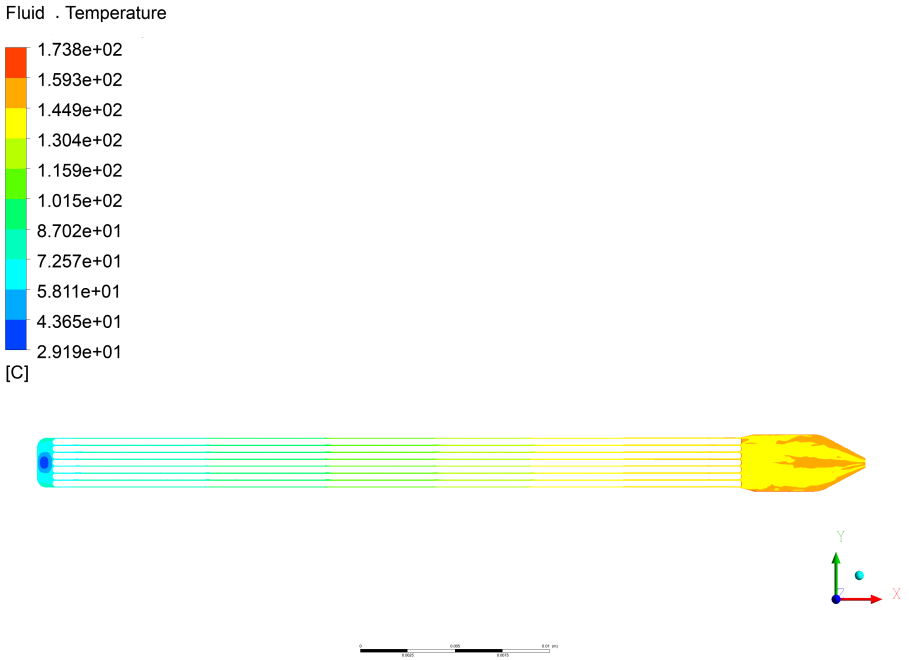


Figure 5.29: Water temperature distribution into thruster of subsonic model.

5.4 Analyzing of the VLM Subsonic Region Simulation

After the optimal shape of the nozzle and pressure level on the inlet region of the supersonic nozzle were obtained, the simulations of the subsonic part of the VLM were conducted. The main aims of the subsonic part simulation were to dock supersonic and subsonic parts of the VLM, optimise the subsonic part of the VLM and obtain the required amount of heat power that should be added to the liquid to produce the required thrust. A series of simulations with different geometries were conducted, but only the optimised geometry results are presented in this document.

The optimisation of the geometry was conducted to achieve highly effective steam generation with the smallest possible size of the VLM. Furthermore, the aim was to prevent steam generation in the inlet region and to produce steam within the microchannels. As a result of the series of numerical simulations, the geometry that is presented in this document was obtained.

By observing the thruster steam volume fraction results as in the Figure (5.19), it was concluded that the most optimal heat power obtained for the heater was equal to 2.0 W. At this heating power, it was observed that the economiser region is in the middle of the microchannels, as shown in Figure (5.20) and zoomed out at Figure (5.21). There, the water boils fast, achieving saturation temperature, and it overheated before leaving the microchannel, reaching overheated steam in the chamber region as noticed in Figure (5.22). At the outlet of the chamber, Figure (5.23), it can be noticed that the average steam volume fraction is reaching 99%, which indicates a high-efficiency chamber.

Distribution of the total pressure and absolute pressure throughout the thruster region (inlet-distributor-microchannels-chamber) are illustrated in Figures (5.24) and Figure (5.25). It shows the total pressure drops linearly up to 5% of its inlet value to the neighbouring zone of the converging part of the nozzle because of the shear force against

the flow acting on the walls. The absolute pressure decreases linearly up to the exit point afterwards, as showing in the Figure (5.26).

Figure (5.27) shows the velocity distribution of the fluid inside the entire thruster subsonic region (inlet-distributor-microchannels-chamber). The results indicate that the velocity of fluid starts increasing linearly, reaching a value of 13 m.s^{-1} at the chamber region.

The temperature field in the silicon was reasonable at the inlet section and distributor section of the VLM thruster, as illustrated in Figure (5.28). There the water temperature has a low temperature too, as illustrated in Figure (5.29). As such, no boiling water started at the inlet section and distributor. Instead, the boiling started to form uniformly at the middle of the microchannels.

During the steady-state iterative simulation process, pressure fluctuations were observed inside the model, as shown in Figure (5.25) with an approximate average frequency of 500 Hz. Aside from pressure fluctuations, steam volume fraction fluctuations occurred on the outlet region, as illustrated in Figures (5.19) and (5.23). However, those fluctuations were small enough, having an amplitude of about 0.005.

Pressure fluctuations, according to the simulation results, as illustrated in Figures (5.21) and (5.22) were obtained due to slug flow into the microchannels. This flow regime was not stable and transformed fast to the film flow, but the pressure fluctuations were produced despite this. The average steam volume fraction of the flow on the outlet part of the VLM model (nozzle inlet) was about 0.992 at a heat power of 2.0 W.

5.5 Comparison of the Various Microthruster Parameters with Optimized VLM

The performance of the VLM system is strongly influenced by the geometry of the in-plane C-D nozzle, the location of the heating chamber, the flow rate of the propellant, power input and microchannels configurations. The variations could result in a difference of micro to milliNewtons of thrust force depending on the flow rate of the propellant, the input power and the exit nozzle configuration. These variations are highlighted in Table 5.6 below. It also shows the performance in terms of thrust, specific impulse and input power. In addition, it shows a comparison of the microthruster device developed in this study with the other references found in the literature. The amount of thrust is equivalent to other instruments in a spectrum but needs to be tested experimentally.

Table 5.6: Comparison of the various microthruster parameters.

Ref.	Thruster type	Nozzle type	Input flow rate ($mg.s^{-1}$)	Input power (W)	Thrust (mN)	Specific impulse(s)
[4]	VLM	In-plane divergent	90	5	0.15-0.46	5 ^a
[12]	VLM	Out-of-plane convergent	0.038	30	0.0029	76.32 ^a
[61]	VLM	Out-of-plane C-D	1.16	2.4	0.005-0.120	75 ^a
[14]	VLM	In-plane convergent	2.083-16.6 simulation data	Hot plate as the external heater	1 -6 simulation data	-
[58]	VLM	In-plane C-D	100-500	-	2-6.5	65 – 105 ^b
[81]	Bi-propellant	In-plane C-D	14	37	0.2-1.97	140
[15]	VLM	In-plane C-D	0.2-2.04	3.6	0.15-1.014	50 – 105 ^b
This work	VLM	In-plane C-D	2	2	1.38	70

(a) Since I_{sp} result was not reported in the refereed publication, the value was calculated by dividing maximum thrust with the maximum flow rate. (b) The value was experimentally achieved.

6 Conclusion and Future Work

In summary, the use of the CubeSats platform is expected to increase in the following decades due to its low risk, environmentally friendly platform and low-cost spacecraft, predominantly amongst university groups, using propulsion systems that have become a primary mobility device. The inclusion of micro green propulsion systems has necessitated growing interest in CubeSats, such as water-based VLM thrusters, to expand their application area, as the VLM thrusters assist with orbit manoeuvres and attitude control of a CubeSat.

This thesis has introduced the optimization of a VLM silicon MEMS thruster micromachined silicon simulation based on [15] by CFD methods. It has shown the method of the shape and working modes optimization. As a result of a series of simulations, the physics of the VLM processes have been understood. The geometry and working modes of the thruster were optimized. The resulting geometry of the VLM is based on the assembly of the best research by other authors [15], [58], and [80], solving the concept errors of their devices so that the resulting geometry is optimized.

As a result of the optimization, there is a 38% higher thrust in comparison to the existing research [15]. This optimization configuration yields 1.38 mN of thrust power and a specific impulse of 70 s using basic analytical equations available in the literature. Furthermore, geometric dimensions of different components, such as the inlet, the distributor, the microchannel, the heater chamber and the outlet nozzle, have been designed to achieve higher efficiency of the system. A 3D CFD analysis of the thruster was

conducted to assess thermodynamic behaviour, such as pressure, velocity, Mach number, the temperature distribution in the inlet dispenser, microchannels, heater chamber and the exit location of the nozzle.

Future work will focus on extending the model to tackle the highlighted aspects and enhancing the paradigms' accuracy by considering a broader scope of parameters. Nevertheless, a study testing the model data may further promote its validity since it was previously accomplished numerically. A more developed application analogy will further be targeted for experimentation of other elements of thrust accruing to the micropropulsion applications.

Bibliography

- [1] J. Chin, R. Coelho, J. Foley, A. Johnstone, R. Nugent, S. Pignatelli, D. Pignatelli, N. Powell, and J. Puig-Suari, “Basic concepts and processes for first-time cubestars developers,” *NASA CubeSats Launch Initiative*, vol. 2470, no. 1–96, 2017.
- [2] “Market analysis and insights : Global nanosatellite and microsatellite market,” <http://https://www.databridgemarketresearch.com/reports/global-nanosatellite-and-microsatellite-market>, Sep. 2020.
- [3] J. Lee and T. Kim, “Mems solid propellant thruster array with micro membrane igniter,” *Sensors and Actuators A: Physical*, vol. 190, pp. 52–60, 2013.
- [4] E. Mukerjee, A. Wallace, K. Yan, D. Howard, R. Smith, and S. Collins, “Vaporizing liquid microthruster,” *Sensors and Actuators A: Physical*, vol. 83, no. 1-3, pp. 231–236, 2000.
- [5] M. C. Louwerse, “Cold gas micro propulsion,” Ph.D. dissertation, University of Twente, 2009.
- [6] T. Takahashi, Y. Takao, K. Eriguchi, and K. Ono, “Numerical and experimental study of microwave-excited microplasma and micronozzle flow for a microplasma thruster,” *Physics of plasmas*, vol. 16, no. 8, p. 083505, 2009.
- [7] J. Aoyagi, M. Mukai, Y. Kamishima, T. Sasaki, K. Shintani, H. Takegahara, T. Wakizono, and M. Sugiki, “Total impulse improvement of coaxial pulsed plasma thruster for small satellite,” *Vacuum*, vol. 83, no. 1, pp. 72–76, 2008.

-
- [8] J. Xiong, Z. Zhou, D. Sun, and X. Ye, “Development of a mems based colloid thruster with sandwich structure,” *Sensors and Actuators A: Physical*, vol. 117, no. 1, pp. 168–172, 2005.
- [9] Z. You, *Space Microsystems and Micro/Nano Satellites*. Butterworth-Heinemann, 2017.
- [10] V. Pallichadath, L. Turmaine, A. Melaika, S. Gelmi, M. V. Ramisa, D. Rijlaarsdam, M. Silva, D. Guerrieri, M. Uludag, B. Zandbergen *et al.*, “In-orbit micro-propulsion demonstrator for pico-satellite applications,” *Acta Astronautica*, vol. 165, pp. 414–423, 2019.
- [11] J. Mueller, J. Ziemer, A. Green, and D. Bame, “Performance characterization of the vaporizing liquid micro thruster ((vlm)),” in *28th International Electric Propulsion Conference, Toulouse, France, 2003*.
- [12] X. Ye, F. Tang, H. Ding, and Z. Zhou, “Study of a vaporizing water micro-thruster,” *Sensors and Actuators A: Physical*, vol. 89, no. 1-2, pp. 159–165, 2001.
- [13] D. K. Maurya, S. Das, and S. Lahiri, “An analytical model of a silicon mems vaporizing liquid microthruster and some experimental studies,” *Sensors and Actuators A: Physical*, vol. 122, no. 1, pp. 159–166, 2005.
- [14] C. C. Chen, C. W. Liu, H. C. Kan, L. H. Hu, G. S. Chang, M. C. Cheng, and B. T. Dai, “Simulation and experiment research on vaporizing liquid micro-thruster,” *Sensors and Actuators A: Physical*, vol. 157, no. 1, pp. 140–149, 2010.
- [15] P. Kundu, T. K. Bhattacharyya, and S. Das, “Design, fabrication and performance evaluation of a vaporizing liquid microthruster,” *Journal of Micromechanics and Microengineering*, vol. 22, no. 2, p. 025016, 2012.
- [16] M. A. Silva, D. C. Guerrieri, H. van Zeijl, A. Cervone, and E. Gill, “Vaporizing liquid microthrusters with integrated heaters and temperature measurement,” *Sensors and Actuators A: Physical*, vol. 265, pp. 261–274, 2017.

-
- [17] B. Liu, X. Yang, Y. Wang, D. Li, G. Gao, J. Yang, and R. Zhou, “A tubular vaporizing liquid micro-thruster with induction heating,” *Heat and Mass Transfer*, pp. 1–9, 2020.
- [18] A. Hoskins, “Resistojets and arcjets,” *Encyclopedia of Aerospace Engineering*, 2010.
- [19] A. M. Pérez, M. Coletti, and S. Gabriel, “Development of a microthruster module for nanosatellite applications,” in *Proc. 32nd Int. Electr. Propuls. Conf.*, 2011.
- [20] Y. Gao, Y. Ma, and J. T. Liu, “A review of the vaporizing liquid microthruster technology,” in *2014 ISFMFE - 6th International Symposium on Fluid Machinery and Fluid Engineering*, 2014, pp. 1–3.
- [21] J. Mueller, “A review and applicability assessment of mems-based microvalve technologies for microspacecraft propulsion,” in *35th Joint Propulsion Conference and Exhibit*, 2000, p. 2725.
- [22] J. Mueller, E.-H. Yang, A. A. Green, V. White, I. Chakraborty, and R. H. Reinicke, “Design and fabrication of mems-based micropropulsion devices at jpl,” in *Reliability, Testing, and Characterization of MEMS/MOEMS*, vol. 4558. International Society for Optics and Photonics, 2001, pp. 57–71.
- [23] J. W. Judy, “Microelectromechanical systems (mems): fabrication, design and applications,” *Smart materials and Structures*, vol. 10, no. 6, p. 1115, 2001.
- [24] J. P. Seymour, F. Wu, K. D. Wise, and E. Yoon, “State-of-the-art mems and microsystem tools for brain research,” *Microsystems & Nanoengineering*, vol. 3, p. 16066, 2017.
- [25] D. Rankin, D. D. Kekez, R. E. Zee, F. M. Pranajaya, D. G. Foisy, and A. M. Beattie, “The canx-2 nanosatellite: expanding the science abilities of nanosatellites,” *Acta Astronautica*, vol. 57, no. 2-8, pp. 167–174, 2005.
- [26] E. Gill, P. Sundaramoorthy, J. Bouwmeester, B. Zandbergen, and R. Reinhard, “Formation flying within a constellation of nano-satellites: The qb50 mission,” *Acta Astronautica*, vol. 82, no. 1, pp. 110–117, 2013.

-
- [27] J. Mueller and J. Mueller, “Thruster options for microspacecraft—a review and evaluation of existing hardware and emerging technologies,” in *33rd joint propulsion conference and exhibit*, 1997, p. 3058.
- [28] A. London, A. Epstein, and J. Kerrebrock, “High-pressure bipropellant microrocket engine,” *Journal of Propulsion and Power*, vol. 17, no. 4, pp. 780–787, 2001.
- [29] K. D. Patel, M. S. Bartsch, M. H. McCrink, J. S. Olsen, B. P. Mosier, and R. W. Crocker, “Electrokinetic pumping of liquid propellants for small satellite microthruster applications,” *Sensors and Actuators B: Chemical*, vol. 132, no. 2, pp. 461–470, 2008.
- [30] D. L. Hitt, C. M. Zakrzewski, and M. A. Thomas, “Mems-based satellite micropropulsion via catalyzed hydrogen peroxide decomposition,” *Smart Materials and Structures*, vol. 10, no. 6, p. 1163, 2001.
- [31] P. Kundu, A. K. Sinha, T. K. Bhattacharyya, and S. Das, “Nanowire embedded hydrogen peroxide monopropellant mems thruster,” *Journal of Microelectromechanical Systems*, vol. 22, no. 2, pp. 406–417, 2012.
- [32] J. Köhler, J. Bejhed, H. Kratz, F. Bruhn, U. Lindberg, K. Hjort, and L. Stenmark, “A hybrid cold gas microthruster system for spacecraft,” *Sensors and Actuators A: Physical*, vol. 97, pp. 587–598, 2002.
- [33] L. Stenmark and A. Eriksson, “Cold gas micro thrusters-final edition,” in *American Institute of Aeronautics and Astronautics*. Uppsala University, Department of Materials Science, 2002, pp. 5765–.
- [34] M. Martinez-Sanchez and J. E. Pollard, “Spacecraft electric propulsion—an overview,” *Journal of propulsion and power*, vol. 14, no. 5, pp. 688–699, 1998.
- [35] A. Greig, C. Charles, N. Paulin, and R. Boswell, “Volume and surface propellant heating in an electrothermal radio-frequency plasma micro-thruster,” *Applied Physics Letters*, vol. 105, no. 5, p. 054102, 2014.

-
- [36] C. Charles, R. Boswell, and A. Bish, “Low-weight fixed ceramic capacitor impedance matching system for an electrothermal plasma microthruster,” *Journal of Propulsion and Power*, vol. 30, no. 4, pp. 1117–1121, 2014.
- [37] W. J. Guman and P. E. Peko, “Solid-propellant pulsed plasma microthruster studies.” *Journal of Spacecraft and Rockets*, vol. 5, no. 6, pp. 732–733, 1968.
- [38] C. Charles, A. Bish, R. Boswell, J. Dedrick, A. Greig, R. Hawkins, and T. S. Ho, “A short review of experimental and computational diagnostics for radiofrequency plasma micro-thrusters,” *Plasma Chemistry and Plasma Processing*, vol. 36, no. 1, pp. 29–44, 2016.
- [39] F. Pranajaya and M. Cappelli, “Development of a colloid micro-thruster for flight demonstration on the emerald nanosatellite,” in *37th Joint propulsion conference and exhibit*, 2001, p. 3330.
- [40] B. Liu, X. Li, J. Yang, and G. Gao, “Recent advances in mems-based microthrusters,” *Micromachines*, vol. 10, no. 12, p. 818, 2019.
- [41] J. Xiong, Z. Zhou, X. Ye, X. Wang, Y. Feng, and Y. Li, “A colloid micro-thruster system,” *Microelectronic Engineering*, vol. 61, pp. 1031–1037, 2002.
- [42] G. I. Taylor, “Disintegration of water drops in an electric field,” *Proceedings of the Royal Society of London. Series A. Mathematical and Physical Sciences*, vol. 280, no. 1382, pp. 383–397, 1964.
- [43] D. G. Courtney, S. Dandavino, and H. Shea, “Comparing direct and indirect thrust measurements from passively fed ionic electrospray thrusters,” *Journal of Propulsion and Power*, vol. 32, no. 2, pp. 392–407, 2016.
- [44] D. Courtney, S. Dandavino, and H. Shea, “Performance and applications of ionic electrospray micro-propulsion prototypes,” in *AIAA SPACE 2015 Conference and Exposition*, 2015, p. 4672.

-
- [45] D. Cordeiro Guerrieri, M. de Athayde Costa e Silva, B. Zandbergen, A. Cervone, D. Cordeiro Guerrieri, B. Zandbergen, and A. Cervone, “Heater chip with different microchannels geometries for a low pressure free molecular micro-resistojet,” *Space propulsion 2016*, 2016.
- [46] S. P. Berg and J. Rovey, “Decomposition of a double salt ionic liquid monopropellant on heated metallic surfaces,” in *52nd AIAA/SAE/ASEE Joint Propulsion Conference*, 2016, p. 4578.
- [47] S. P. Berg, J. Rovey, B. Prince, S. Miller, and R. Bemish, “Electrospray of an energetic ionic liquid monopropellant for multi-mode micropropulsion applications,” in *51st AIAA/SAE/ASEE Joint Propulsion Conference*, 2015, p. 4011.
- [48] M. Ivanov, G. Markelov, A. Ketsdever, and D. Wadsworth, “Numerical study of cold gas micronozzle flows,” in *37th Aerospace Sciences Meeting and Exhibit*, 1999, p. 166.
- [49] R. H. Lee, A. Bauer, M. D. Killingsworth, T. Lilly, J. Duncan, and A. Ketsdever, “Free-molecule-microresistojet performance using water propellant for nanosatellite applications,” *Journal of Spacecraft and Rockets*, vol. 45, no. 2, pp. 264–269, 2008.
- [50] Z. Ahmed, S. F. Gimelshein, and A. D. Ketsdever, “Numerical analysis of free-molecule microresistojet performance,” *Journal of propulsion and power*, vol. 22, no. 4, pp. 749–756, 2006.
- [51] A. Ketsdever, D. Wadsworth, S. Vargo, and E. Muntz, “The free molecule micro-resistojet-an interesting alternative to nozzle expansion,” in *34th AIAA/ASME/SAE/ASEE Joint Propulsion Conference and Exhibit*, 1998, p. 3918.
- [52] D. C. Guerrieri, A. Cervone, and E. Gill, “Analysis of nonisothermal rarefied gas flow in diverging microchannels for low-pressure microresistojets,” *Journal of Heat Transfer*, vol. 138, no. 11, 2016.
- [53] D. C. Guerrieri, M. A. Silva, H. van Zeijl, A. Cervone, and E. Gill, “Fabrication and characterization of low pressure micro-resistojets with integrated heater and

-
- temperature measurement,” *Journal of Micromechanics and Microengineering*, vol. 27, no. 12, p. 125005, 2017.
- [54] A. Blanco and S. Roy, “Numerical simulation of a free molecular electro jet (fmej) for in-space propulsion,” in *51st AIAA Aerospace Sciences Meeting including the New Horizons Forum and Aerospace Exposition*, 2013, p. 208.
- [55] K. Palmer, H. Nguyen, and G. Thornell, “Fabrication and evaluation of a free molecule micro-resistojet with thick silicon dioxide insulation and suspension,” *Journal of Micromechanics and Microengineering*, vol. 23, no. 6, p. 065006, 2013.
- [56] K. H. Cheah and J. Chin, “Performance improvement on mems micropropulsion system through a novel two-depth micronozzle design,” *Acta Astronautica*, vol. 69, no. 1-2, pp. 59–70, 2011.
- [57] P. Haris and T. Ramesh, “Numerical simulation of superheated steam flow in a micronozzle,” in *Applied Mechanics and Materials*, vol. 592. Trans Tech Publ, 2014, pp. 1677–1681.
- [58] J. Cen and J. Xu, “Performance evaluation and flow visualization of a mems based vaporizing liquid micro-thruster,” *Acta Astronautica*, vol. 67, no. 3-4, pp. 468–482, 2010.
- [59] P. Kundu, T. K. Bhattacharyya, and S. Das, “Electro-thermal analysis of an embedded boron diffused microheater for thruster applications,” *Microsystem technologies*, vol. 20, no. 1, pp. 23–33, 2014.
- [60] D. C. Guerrieri, M. A. Silva, A. Cervone, and E. Gill, “Selection and characterization of green propellants for micro-resistojets,” *Journal of Heat Transfer*, vol. 139, no. 10, p. 102001, 2017.
- [61] D. K. Maurya, S. Das, and S. Lahiri, “Silicon mems vaporizing liquid microthruster with internal microheater,” *Journal of Micromechanics and Microengineering*, vol. 15, no. 5, p. 966, 2005.

-
- [62] M. Gad-el Hak, *The MEMS handbook*. CRC press, 2001.
- [63] M. Mihailovic, T. Mathew, J. Creemer, B. Zandbergen, and P. Sarro, “Mems silicon-based resistojet micro-thruster for attitude control of nano-satellites,” in *2011 16th International Solid-State Sensors, Actuators and Microsystems Conference*. IEEE, 2011, pp. 262–265.
- [64] K. H. Cheah and K.-S. Low, “Fabrication and performance evaluation of a high temperature co-fired ceramic vaporizing liquid microthruster,” *Journal of Micromechanics and Microengineering*, vol. 25, no. 1, p. 015013, 2014.
- [65] K. Karthikeyan, S. Chou, L. Khoong, Y. Tan, C. Lu, and W. Yang, “Low temperature co-fired ceramic vaporizing liquid microthruster for microspacecraft applications,” *Applied energy*, vol. 97, pp. 577–583, 2012.
- [66] J. Mueller, W. Tang, A. Wallace, R. Lawton, W. Li, D. Bame, I. Chakraborty, J. Mueller, W. Tang, A. Wallace *et al.*, “Design, analysis and fabrication of a vaporizing liquid micro-thruster,” in *33rd Joint Propulsion Conference and Exhibit*, 1997, p. 3054.
- [67] M. R. Gongora-Rubio, P. Espinoza-Vallejos, L. Sola-Laguna, and J. Santiago-Aviles, “Overview of low temperature co-fired ceramics tape technology for meso-system technology (msst),” *Sensors and Actuators A: Physical*, vol. 89, no. 3, pp. 222–241, 2001.
- [68] L. Denies, B. Zandbergen, P. Natale, D. Ricci, M. Invigorito, L. Denies, and B. Zandbergen, “Analysis of supercritical methane in rocket engine cooling channels,” *SP2016, Rome,(SP2016-3124783)*, 2016.
- [69] I. Krusharev, “Micro-thruster development: Propulsion system for the delffi mission,” 2015.
- [70] R. Ferreira, “Development and testing of a water microresistojet,” *TU Delft, Aerospace Engineering, Systems Integration/Space*, 2008.

-
- [71] G. P. Sutton and O. Biblarz, *Rocket propulsion elements*. John Wiley & Sons, 2016.
- [72] P. Kundu, T. Bhattacharyya, and S. Das, “A monopropellant hydrazine mems thruster for attitude control of nanosatellites,” in *2010 IEEE Students Technology Symposium (TechSym)*. IEEE, 2010, pp. 137–141.
- [73] R. Poyck, A. Cervone, B. Zandbergen, H. van Zeijl, I. Krusharev, and Q. Bellini, “A water-fed micro-resistojet for the delfi formation flying mission,” in *IAF 65th International Astronautical Congress, Canada, 2014*.
- [74] R. L. Bayt and K. S. Breuer, “Analysis and testing of a silicon intrinsic-point heater in a micropropulsion application,” *Sensors and Actuators A: Physical*, vol. 91, no. 3, pp. 249–255, 2001.
- [75] M. G. De Giorgi, D. Fontanarosa, and A. Ficarella, “Modeling viscous effects on boundary layer of rarefied gas flows inside micronozzles in the slip regime condition,” *Energy Procedia*, vol. 148, pp. 838–845, 2018.
- [76] J. I. Rojas-Sola, C. García-Baena, and M. J. Hermoso-Orzáez, “A review of the computational fluid dynamics simulation software: Advantages, disadvantages and main applications,” *Journal of Magnetohydrodynamics and Plasma Research*, vol. 21, no. 4, pp. 417–424, 2016.
- [77] Y. H. Alahmadi and A. F. Nowakowski, “Modified shear stress transport model with curvature correction for the prediction of swirling flow in a cyclone separator,” *Chemical Engineering Science*, vol. 147, pp. 150–165, 2016.
- [78] Y. H. Alahmadi, “On the application of an eddy viscosity turbulence model sensitized to rotation/curvature to the cyclone separator,” Ph.D. dissertation, University of Sheffield, 2016.
- [79] P. C. Rocha, H. B. Rocha, F. M. Carneiro, M. V. da Silva, and A. V. Bueno, “ $k-\omega$ sst (shear stress transport) turbulence model calibration: A case study on a small scale horizontal axis wind turbine,” *Energy*, vol. 65, pp. 412–418, 2014.

-
- [80] M. A. Silva, S. Silvestrini, D. C. Guerrieri, A. Cervone, and E. Gill, “A comprehensive model for control of vaporizing liquid microthrusters,” *IEEE Transactions on Control Systems Technology*, 2018.
- [81] M.-H. Wu and P.-S. Lin, “Design, fabrication and characterization of a low-temperature co-fired ceramic gaseous bi-propellant microthruster,” *Journal of Micromechanics and Microengineering*, vol. 20, no. 8, p. 085026, 2010.

7 Appendix A (More Simulation Results of the VLM Supersonic Region)

The simulation of the single-phase supersonic part of VLM was iterative. Thirteen more numerical simulations were made respectively under the flowing parameters:

- Constant mass flow rate through the nozzle equal to 2.0 mg.s^{-1} .
- Inlet area of the nozzle (cross section area of the chamber) was constant and equal to 0.3 mm^2 .
- Total angle of the subsonic confuser was constant in all simulations and equal to 56° .
- Cross section area of the sonic part of the nozzle was constant and equal to 0.005 mm^2 .

Dimensions of the nozzle, statistical data and numerical results of simulations are presented in Tables (7.1), (7.2), (7.3) and Figures (7.1) to (7.13) below.

Table 7.1: Numerical data of the nozzle simulation.

Geometry code No.	Nozzle outlet area, (mm^2)	Nozzle outlet ratio, A_r	Supersonic divergent total angle, (degree)	Supersonic divergent, length, (mm)	Subsonic/supersonic convergent transition curve radius, (mm)	Subsonic convergent inlet curve radius, (mm)
V1	0.0470	9.4	56 °	0.80	0.0	0.0
V2	0.0724	14.48	46 °	0.80	0.1	0.0
V3	0.0724	14.48	Curved, barreled	0.80	0.1	1.0
V4	0.0649	12.98	Curved, barreled	1.10	0.1	1.0
V5	0.0750	15.00	Curved, barreled	1.10	0.1	1.0
V6	0.0677	13.54	Curved, barreled	0.90	0.1	1.0
V7	0.0790	15.80	45 °	0.90	0.1	1.0
V8	0.0639	12.78	Curved, barreled	0.80	0.1	1.0
V9	0.0592	11.84	Curved, barreled	0.70	0.1	1.0
V10	0.0535	10.7	45 °	0.60	0.1	1.0
V11	0.0469	9.38	46 °	0.50	0.1	1.0
V11.1	0.0469	9.38	46 °	0.50	0.1	1.0
V11.2	0.0469	9.3	46 °	0.50	0.1	1.0
V12	0.0426	8.52	45 °	0.45	0.1	1.0

Table 7.2: Numerical data of the nozzle simulation at chamber inlet.

Geometry code No.	Bulk temperature, (K)	Average velocity, $m.s^{-1}$	Average Mach Number	Static Pressure, (Pa)	Total Pressure, (Pa)	Density, ($kg.m^{-3}$)
V1	383	26.1	0.05	283618	284173	1.604
V2	383	27.7	0.06	267616	268204	1.514
V3	383	32.7	0.07	226190	226885	1.279
V4	383	29.2	0.06	253067	253689	1.432
V5	383	28.9	0.06	255779	256394	1.447
V6	383	29.3	0.06	252555	253178	1.429
V7	383	28.1	0.06	263476	264073	1.490
V8	383	29.6	0.06	250284	250913	1.416
V9	383	29.5	0.06	250543	251171	1.417
V10	383	29.7	0.06	249192	249824	1.410
V11	383	29.8	0.06	248689	249322	1.407
V11.1	473	33.3	0.06	274138	274847	1.256
V11.2	426	31.3	0.06	262869	263535	1.337
V12	383	30.5	0.06	242497	243146	1.372

Table 7.3: Numerical data of the nozzle simulation at nozzle outlet.

Geometry code No.	Bulk temperature, (K)	Average velocity, ($m.s^{-1}$)	Average Mach Number	Static Pressure, (Pa)	Total Pressure, (Pa)	Density, ($kg.m^{-3}$)	Thrust, (mN)
V1	269	419	1.06	7663	43426	0.053	0.85
V2	248	602	1.57	5168	51029	0.042	1.17
V3	251	651	1.68	4900	43759	0.041	1.06
V4	287	542	1.31	6649	29339	0.049	1.00
V5	290	531	1.38	6029	25457	0.044	0.99
V6	264	597	1.51	5364	37140	0.042	1.10
V7	260	573	1.46	5092	39429	0.040	1.10
V8	251	624	1.62	5148	46959	0.042	1.13
V9	237	656	1.75	5028	61451	0.043	1.19
V10	226	684	1.87	5087	80903	0.045	1.24
V11	215	713	1.99	5331	109867	0.050	1.29
V11.1	264	795	2.00	5686	122553	0.044	1.42
V11.2	238	751	2	5542	117331	0.047	1.38
V12	213	718	2.01	5552	121051	0.053	1.27

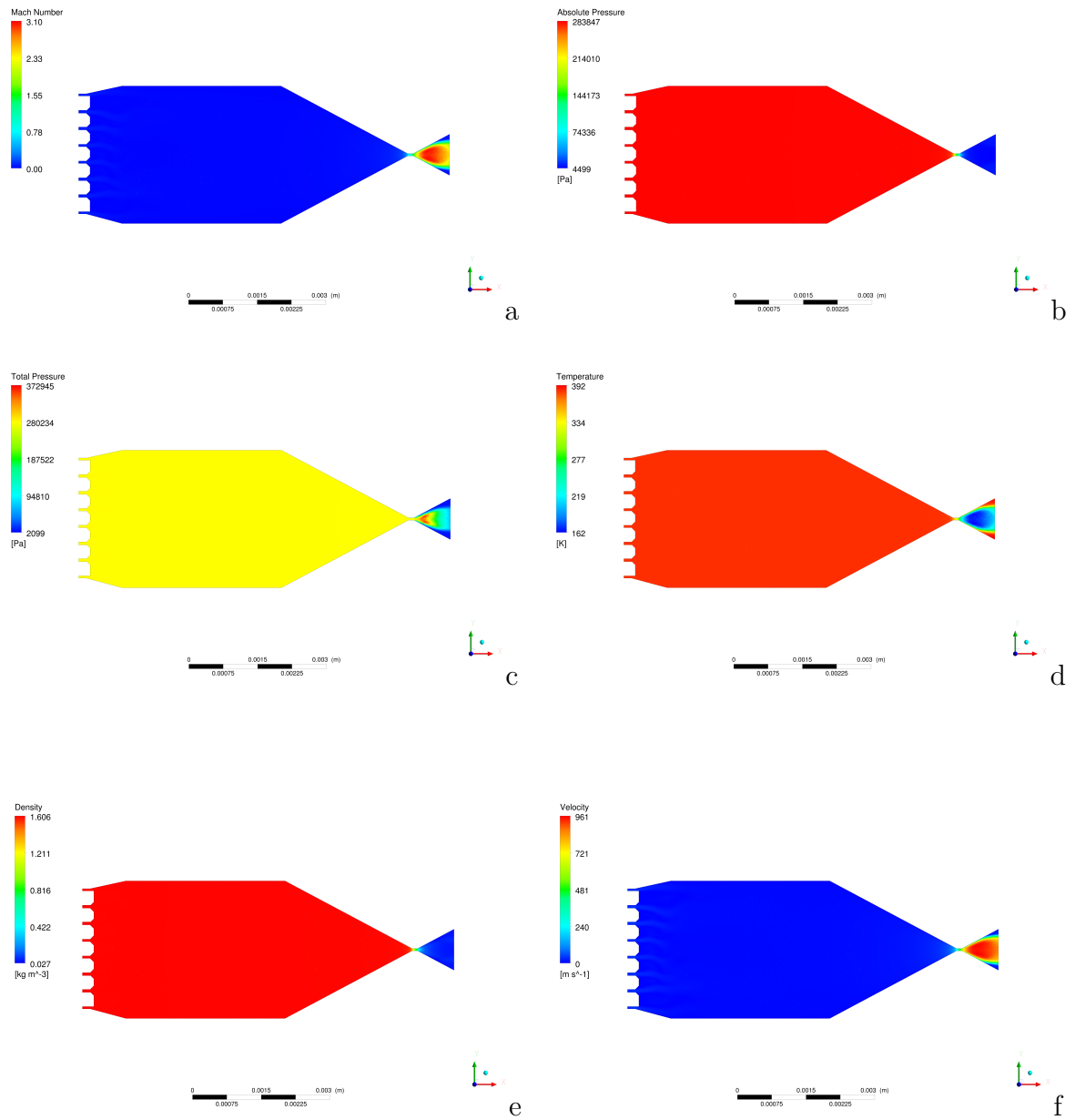


Figure 7.1: Geometry code V1, a. Mach number; b. absolute pressure; c. total pressure; d, temperature; e. density; f. velocity.

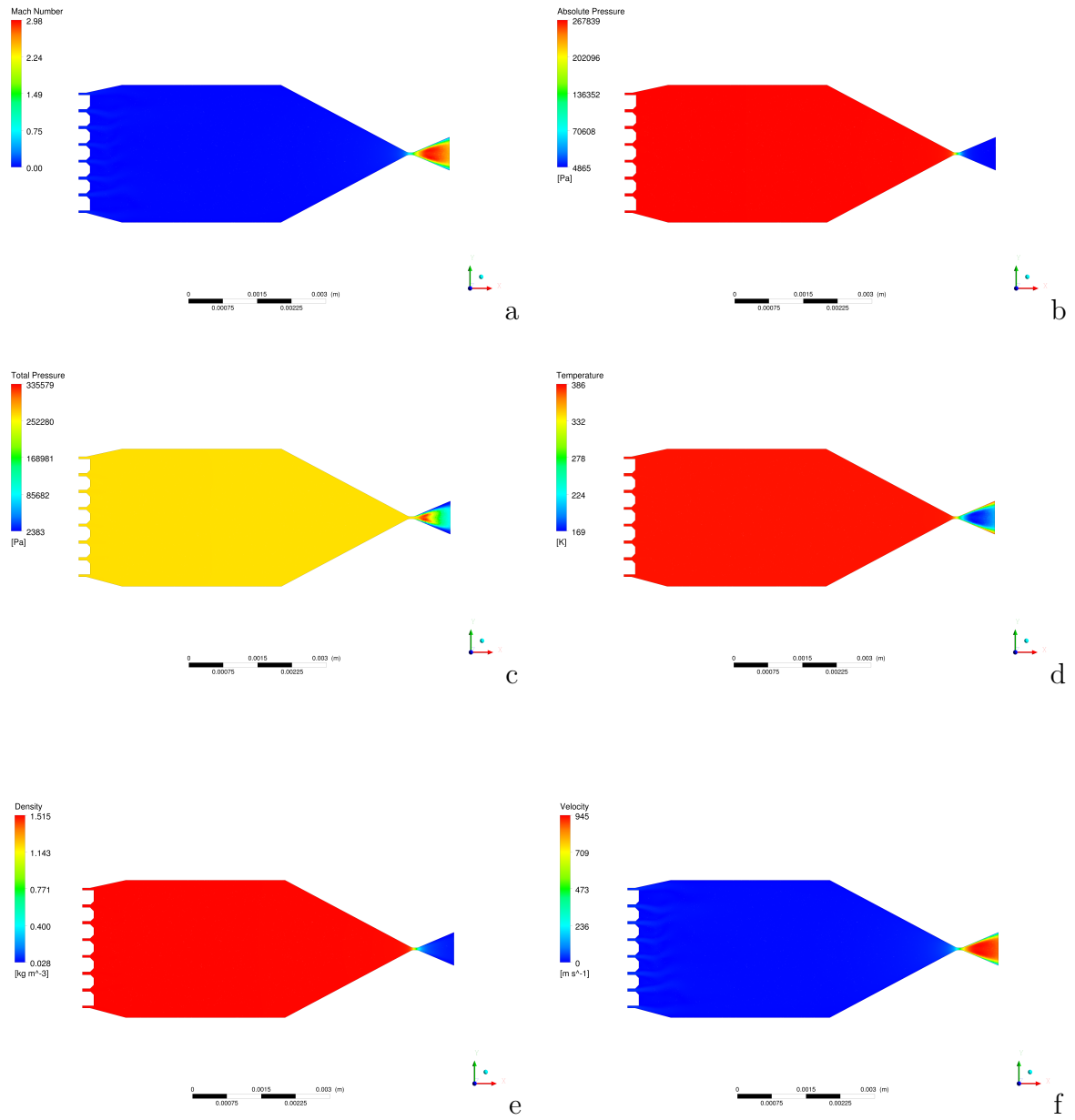


Figure 7.2: Geometry code V2, a. Mach number; b. absolute pressure; c. total pressure; d, temperature; e. density; f. velocity.

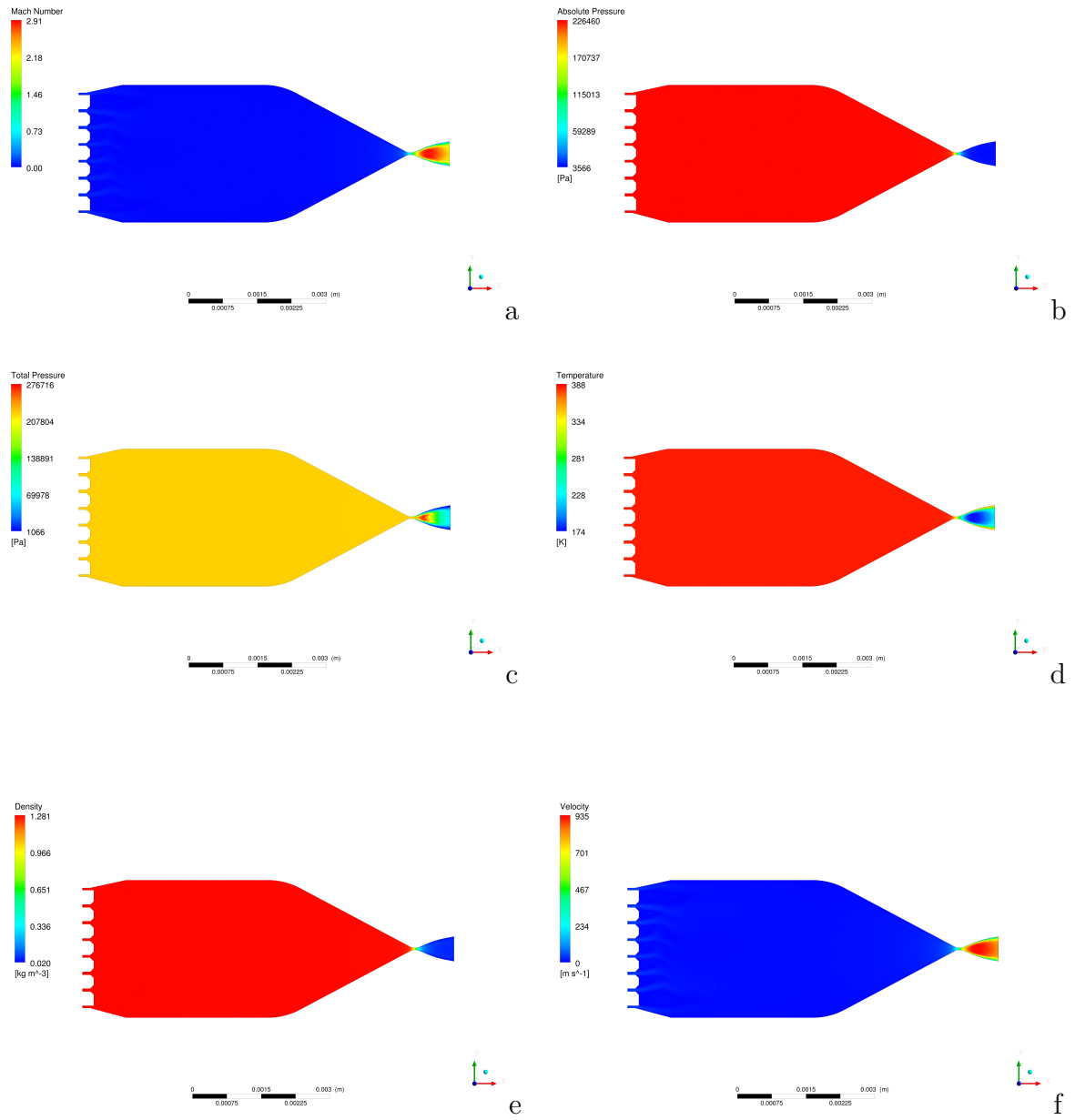


Figure 7.3: Geometry code V3, a. Mach number; b. absolute pressure; c. total pressure; d, temperature; e. density; f. velocity.

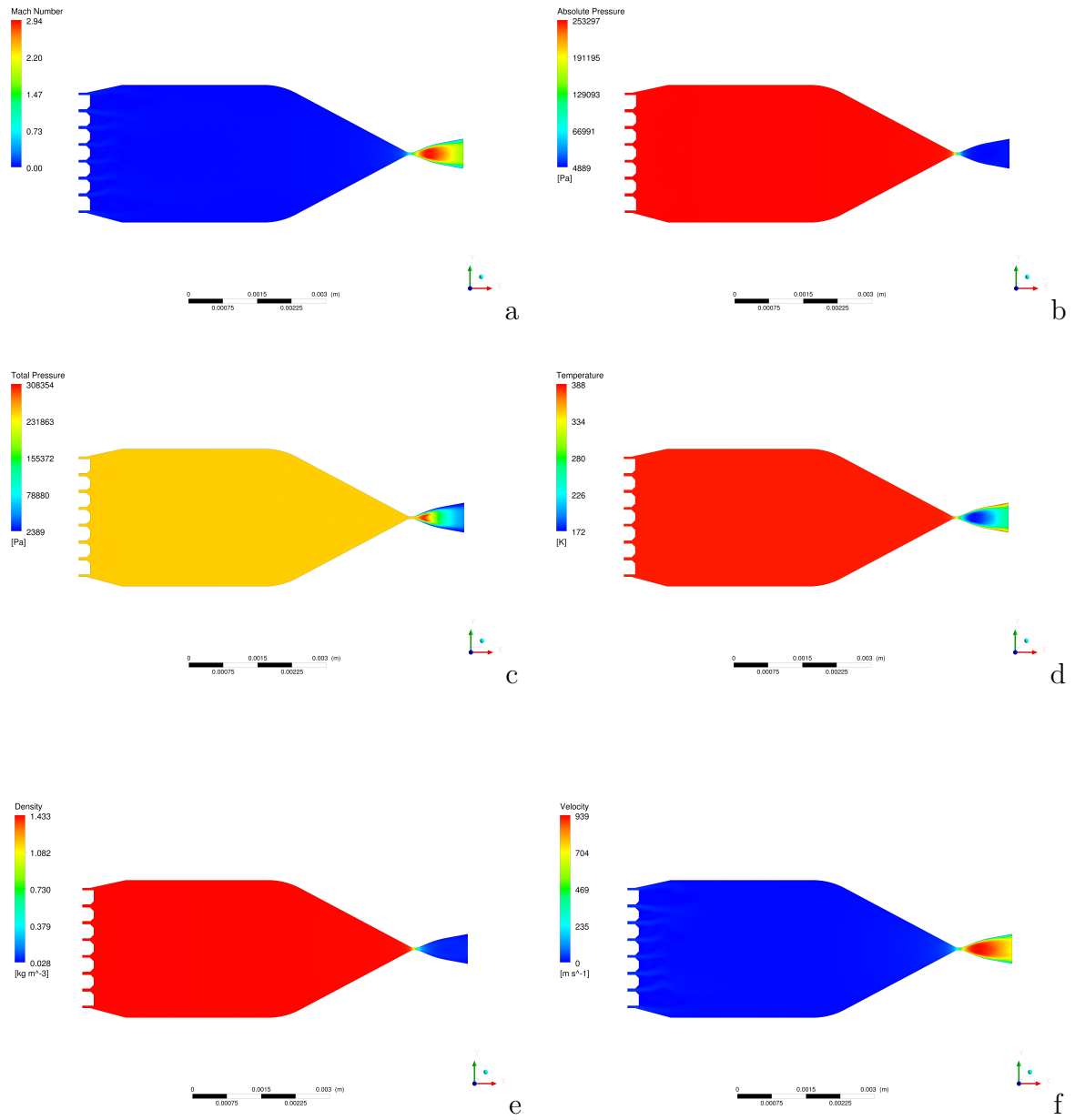


Figure 7.4: Geometry code V4, a. Mach number; b. absolute pressure; c. total pressure; d, temperature; e. density; f. velocity.

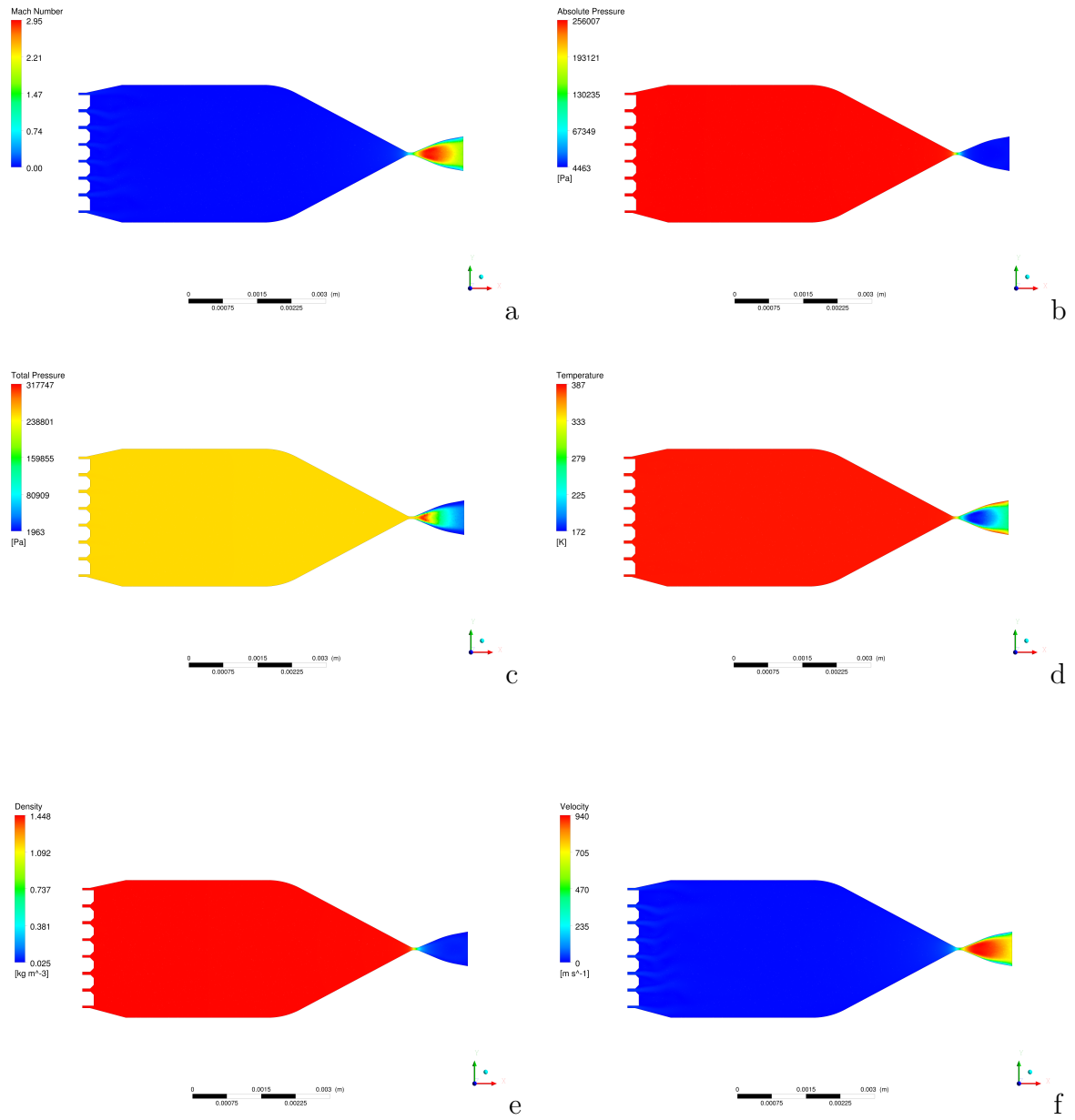


Figure 7.5: Geometry code V5, a. Mach number; b. absolute pressure; c. total pressure; d, temperature; e. density; f. velocity.

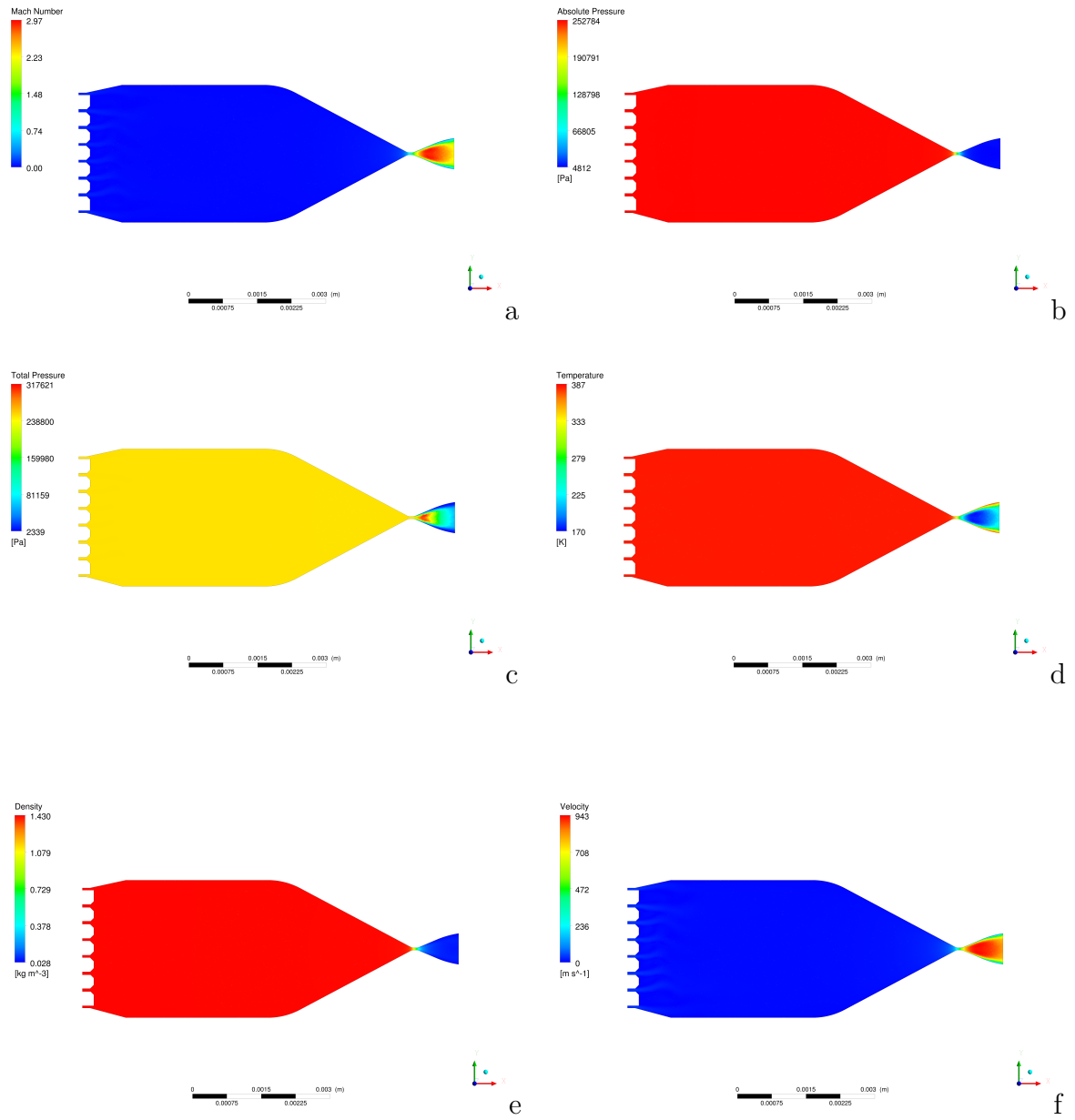


Figure 7.6: Geometry code V6, a. Mach number; b. absolute pressure; c. total pressure; d, temperature; e. density; f. velocity.

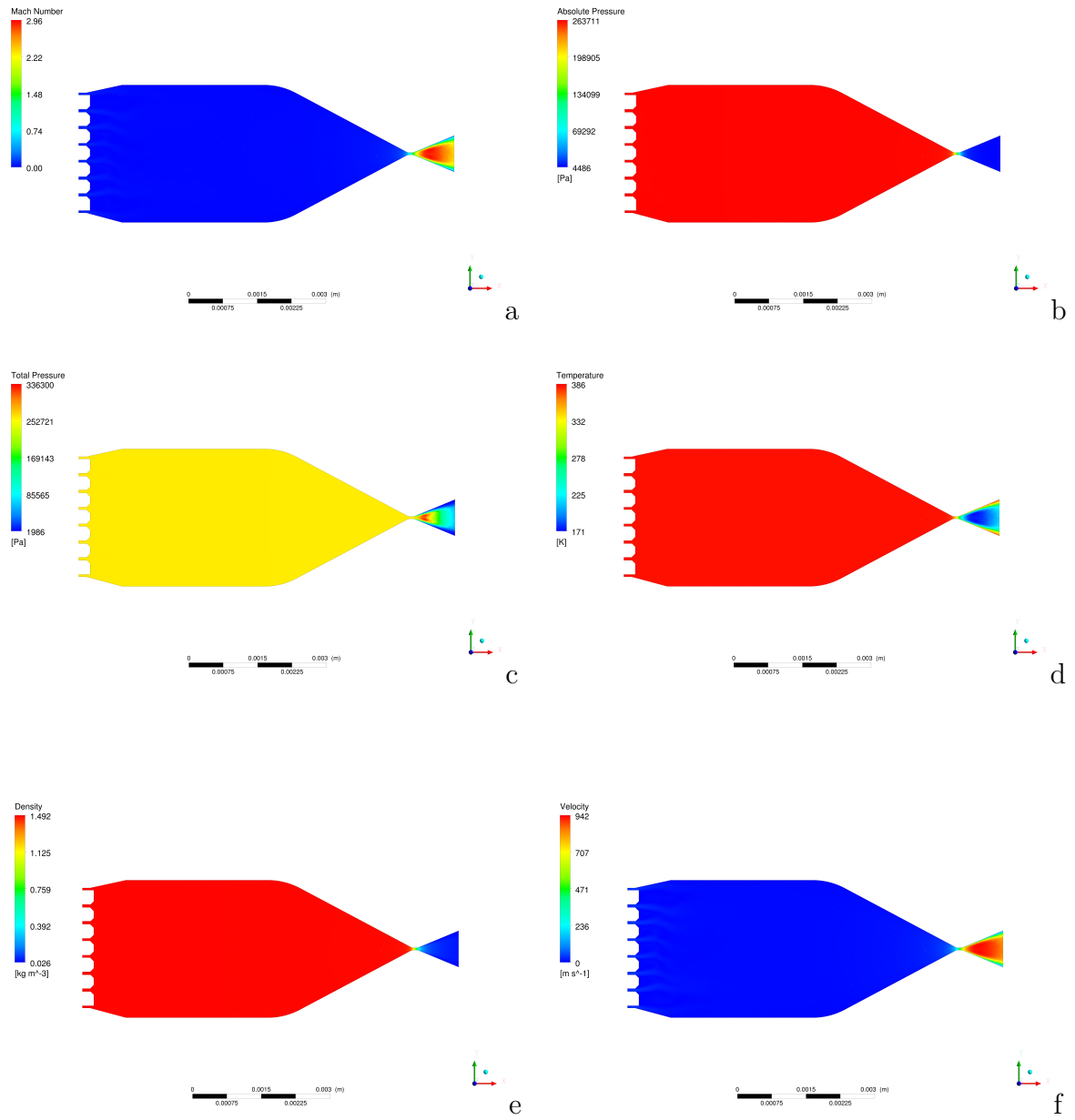


Figure 7.7: Geometry code V7, a. Mach number; b. absolute pressure; c. total pressure; d, temperature; e. density; f. velocity.

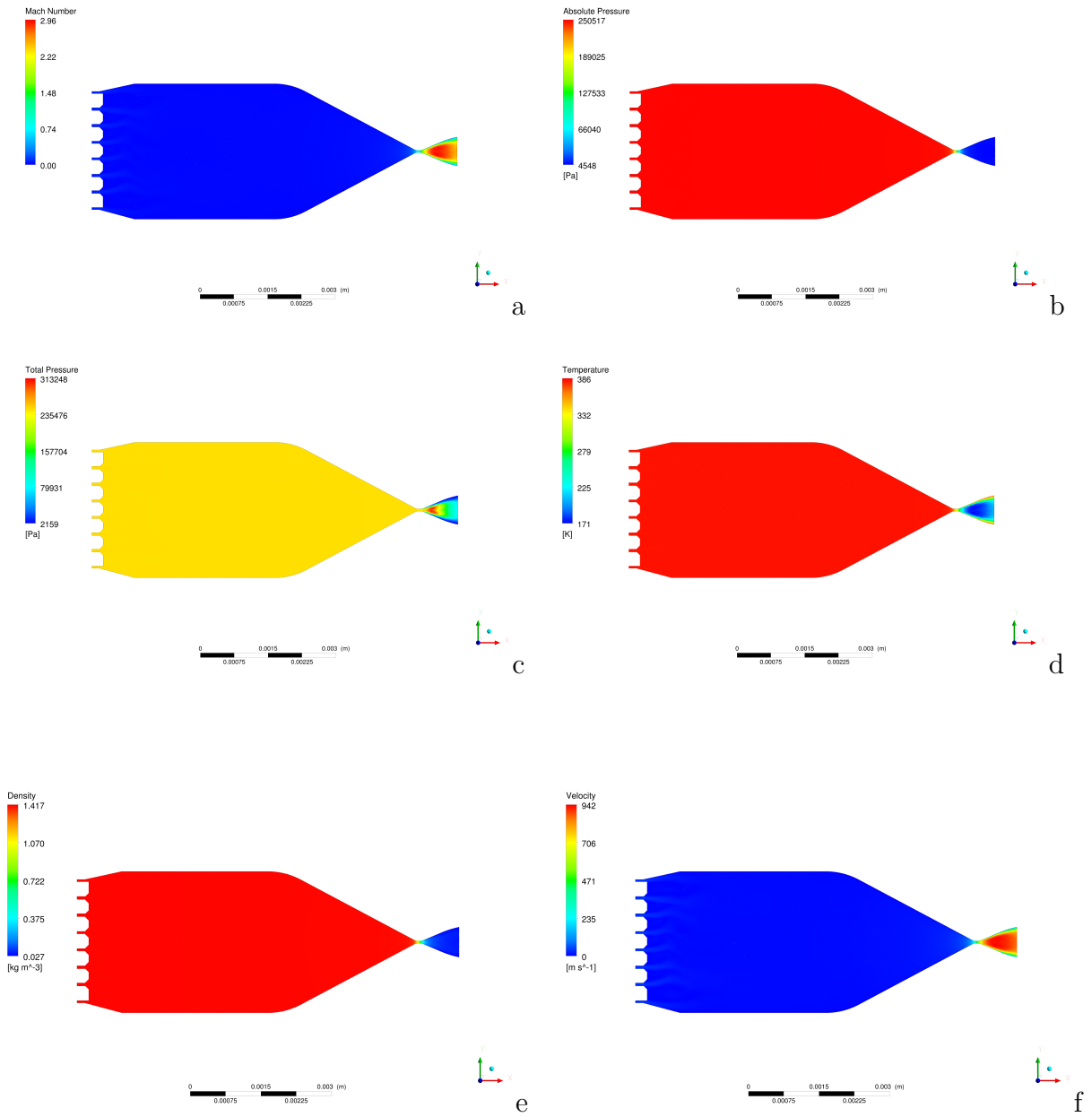


Figure 7.8: Geometry code V8, a. Mach number; b. absolute pressure; c. total pressure; d, temperature; e. density; f. velocity.

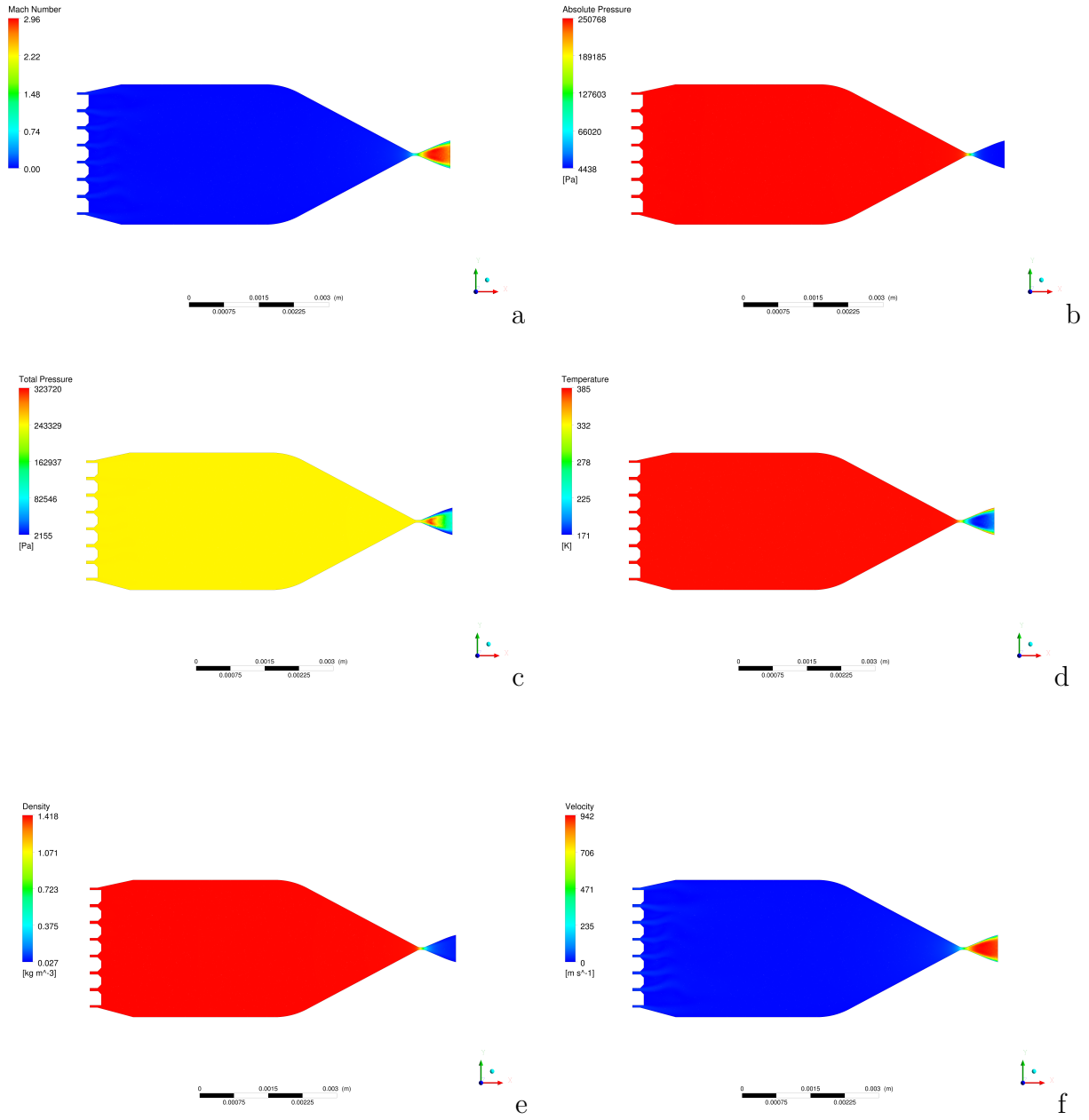


Figure 7.9: Geometry code V9, a. Mach number; b. absolute pressure; c. total pressure; d, temperature; e. density; f. velocity.

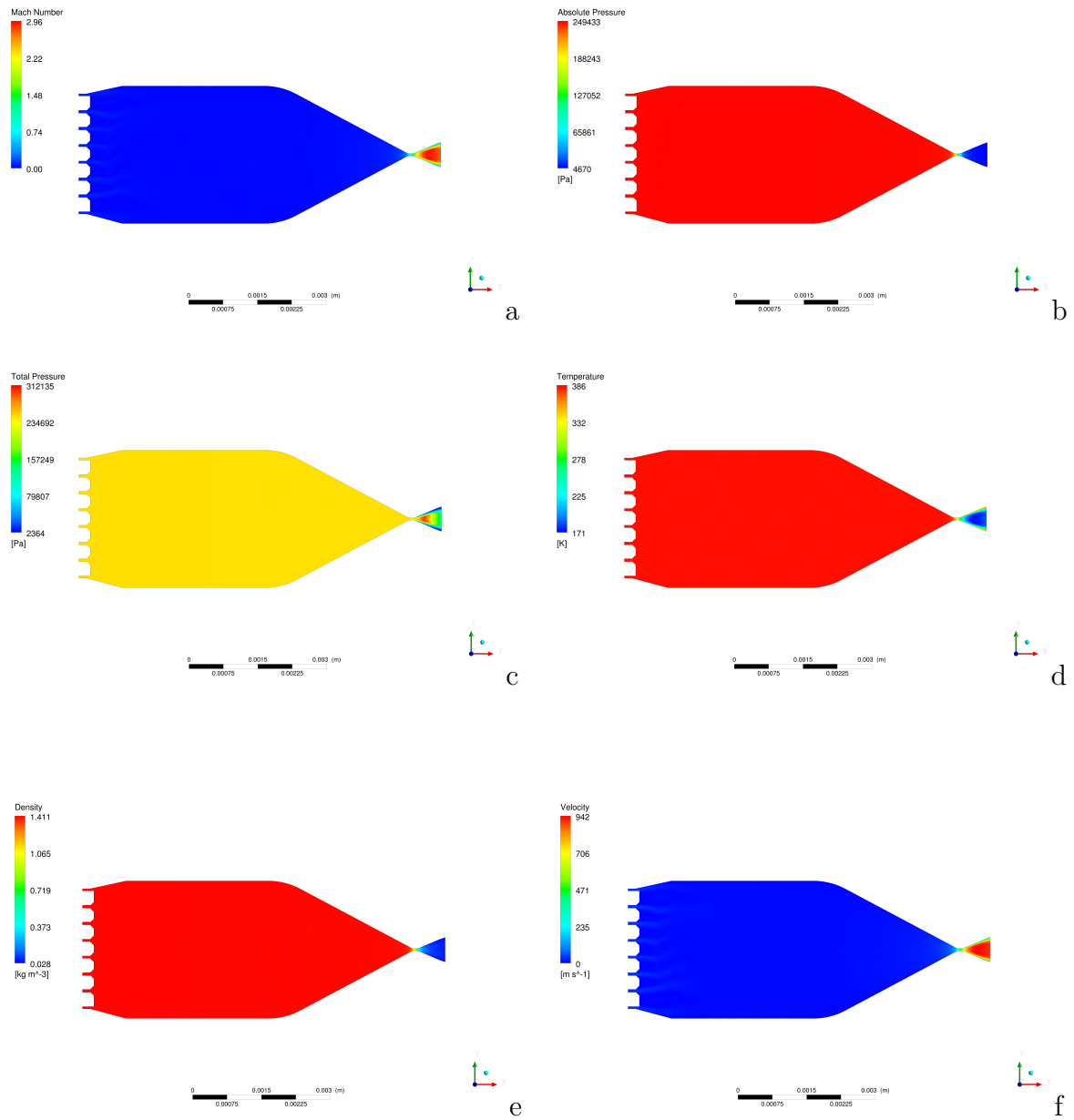


Figure 7.10: Geometry code V10, a. Mach number; b. absolute pressure; c. total pressure; d, temperature; e. density; f. velocity.

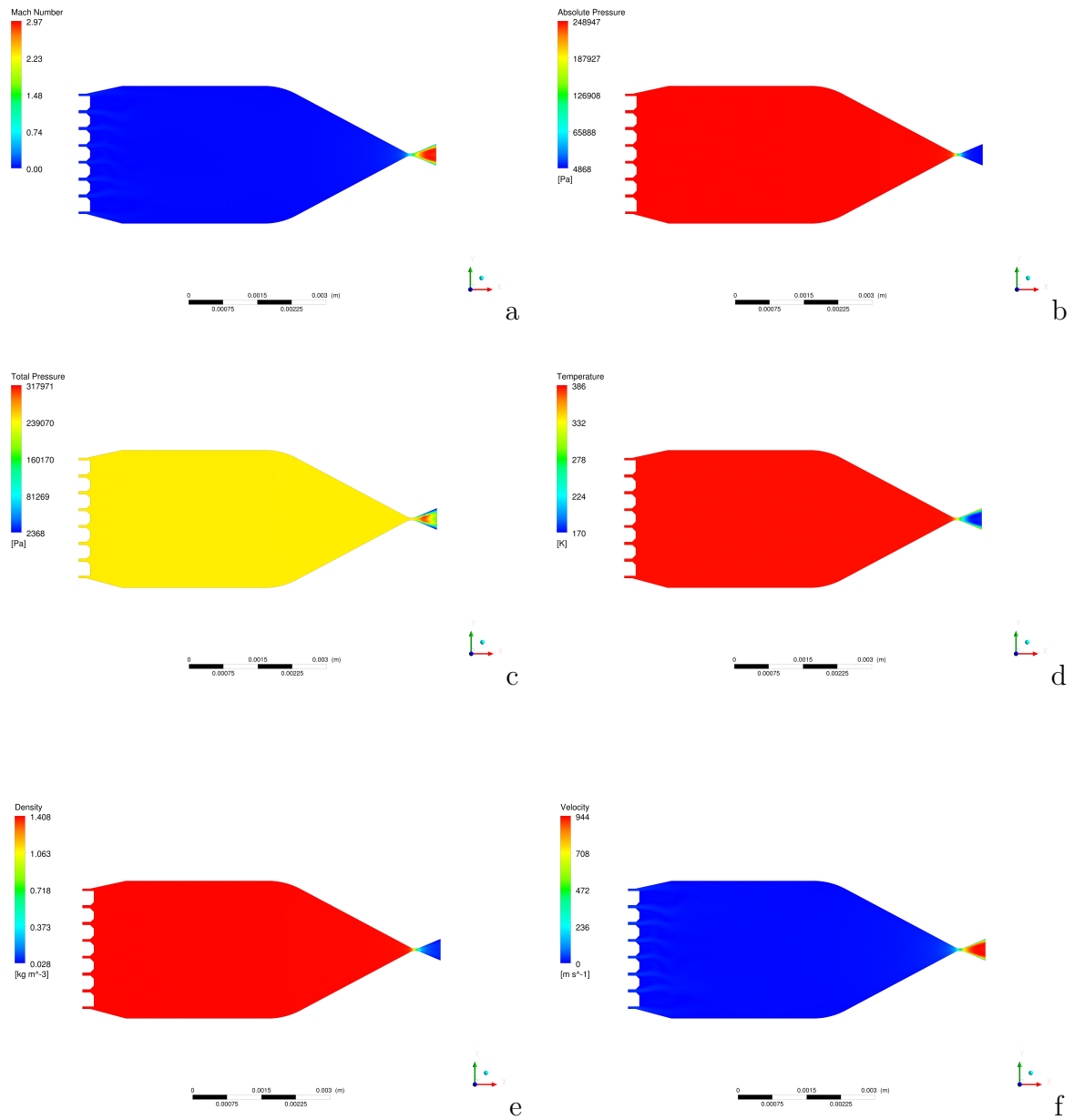


Figure 7.11: Geometry code V11, a. Mach number; b. absolute pressure; c. total pressure; d, temperature; e. density; f. velocity.

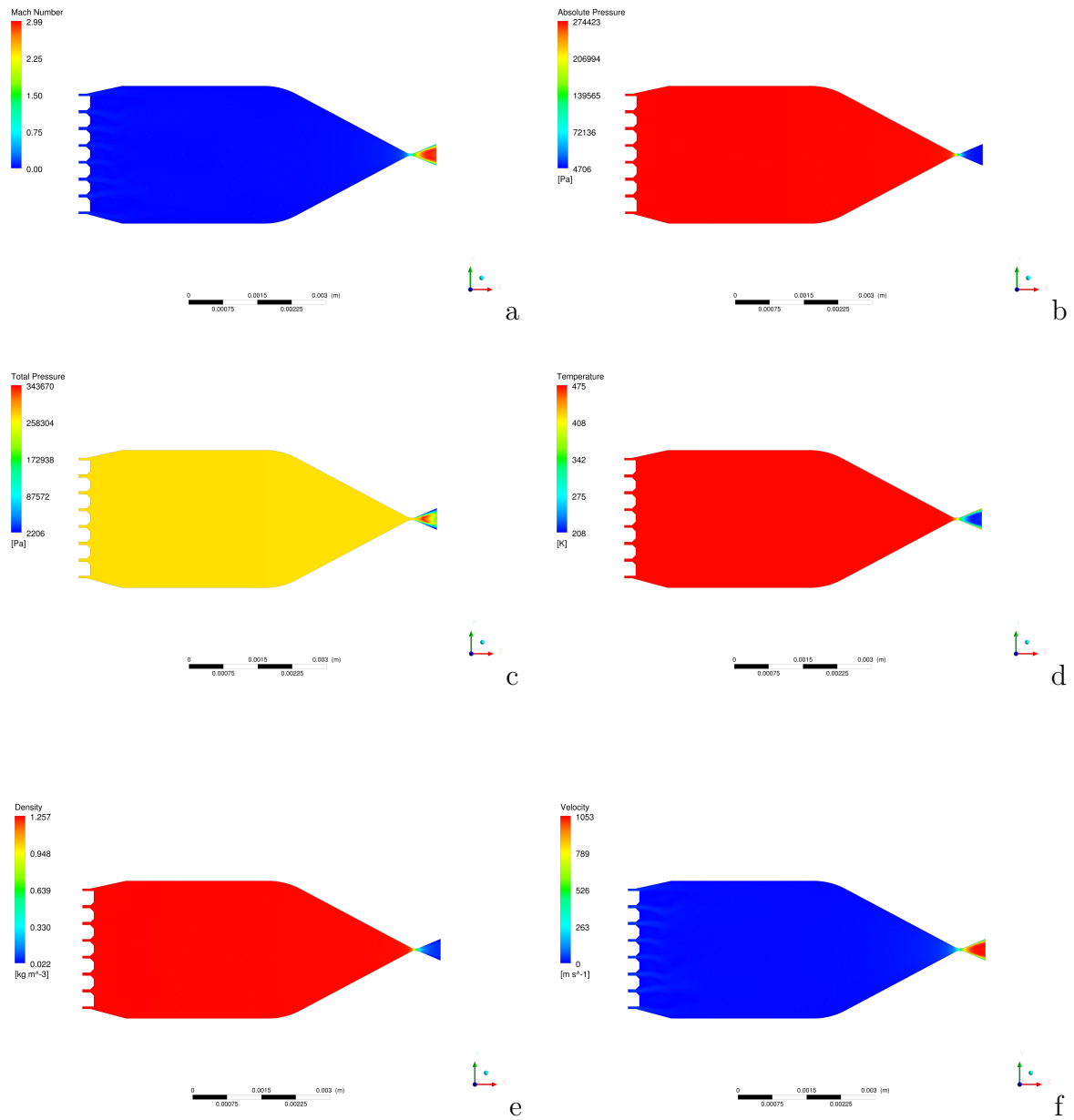


Figure 7.12: Geometry code V11.1, a. Mach number; b. absolute pressure; c. total pressure; d, temperature; e. density; f. velocity.

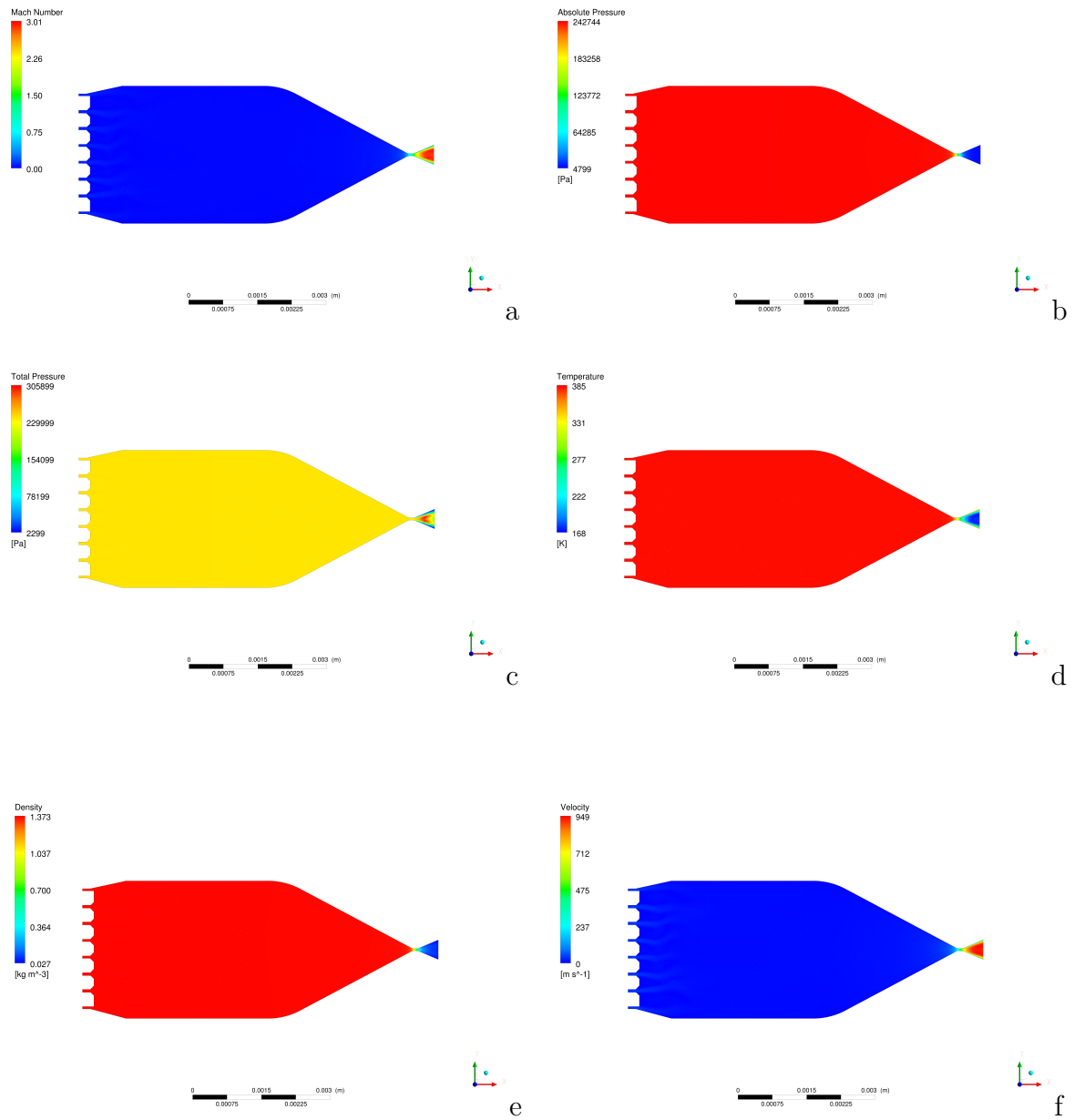


Figure 7.13: Geometry code V12, a. Mach number; b. absolute pressure; c. total pressure; d, temperature; e. density; f. velocity.

8 Appendix B (More Simulation Results of the VLM Subsonic Region)

The simulation of the subsonic part was iterative. Two more modes of the heat power were used: 2.3 W and 3.6 W respectively. The numerical simulation results of the 2.3 W multi-phase subsonic part of the VLM are illustrated in Table (8.1) and Figures (8.1) to (8.10). Moreover, the numerical simulation results of the 3.6 W heating power are presented in Table (8.2) and Figures (8.11) to (8.18) below.

Table 8.1: Numerical data of the VLM subsonic model simulation at heat power 2.3 W.

Location	Modle inlet	Microchannels inlet	Microchannels cross-section average plane	microchannels outlet	Model outlet
Steam bulk temperature, (K)	405	405	406	446	453
Water bulk temperature, (K)	304	360	385	418	423
Velocity, ($m.s^{-1}$)	3×10^{-12}	$6V \times 10^{-10}$	4×10^{-8}	1.9	5.2
Static Pressure, (Pa)	252500	252558	258314	260587	260299
Total Pressure, (Pa)	252502	252612	258363	260711	260506
Density, ($kg.m^{-3}$)	993	967	950	12	7.7
Steam volume fraction	5×10^{-11}	2×10^{-9}	1×10^{-7}	0.989	0.993

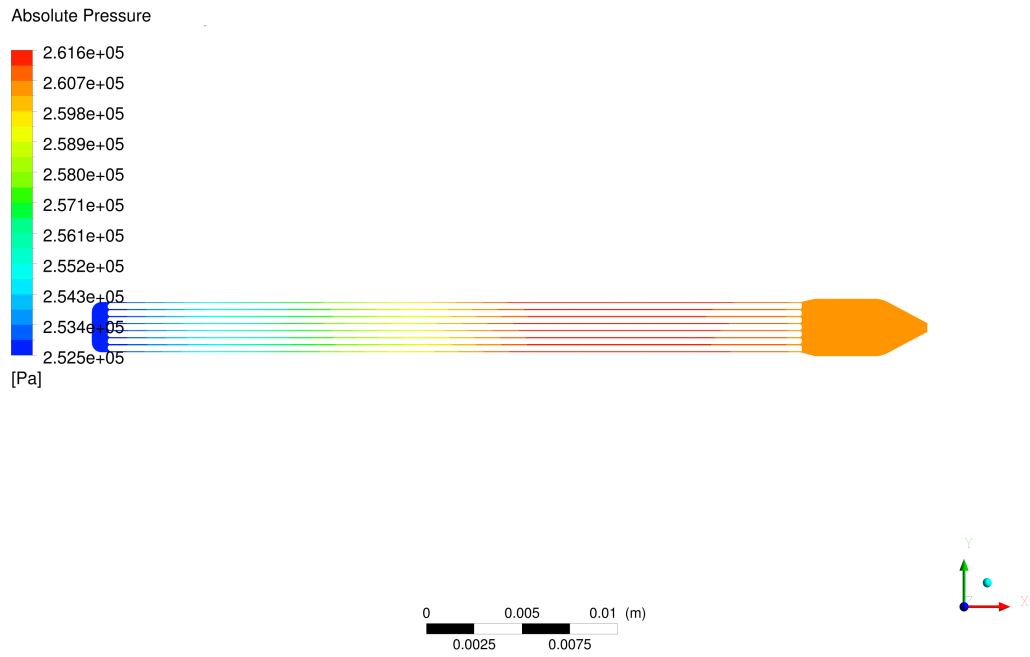


Figure 8.1: Absolute pressure distribution into thruster.

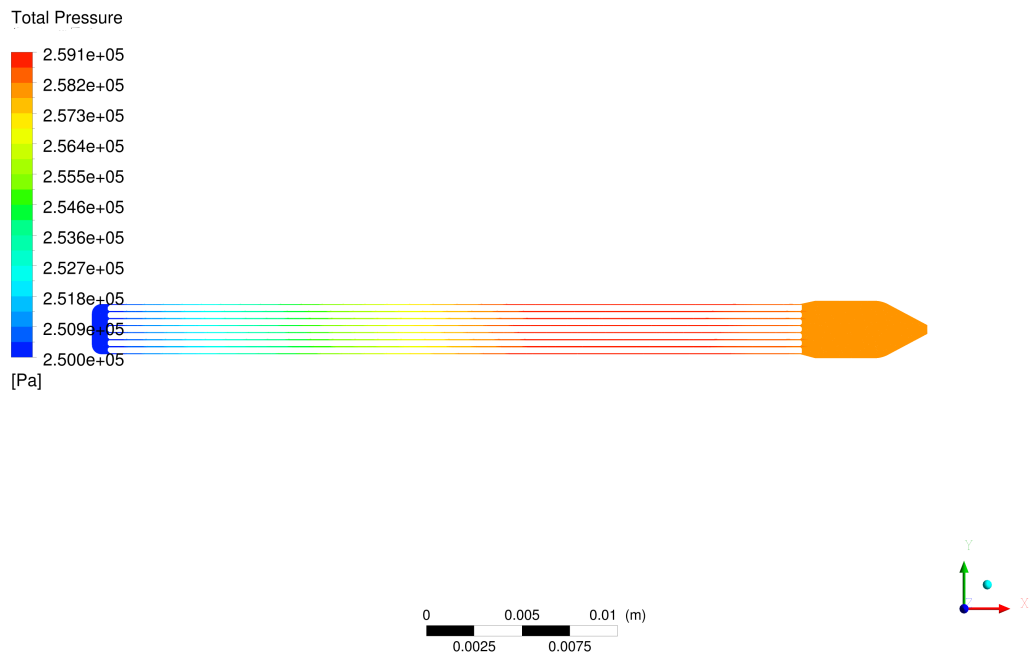


Figure 8.2: Total pressure distribution into thruster.

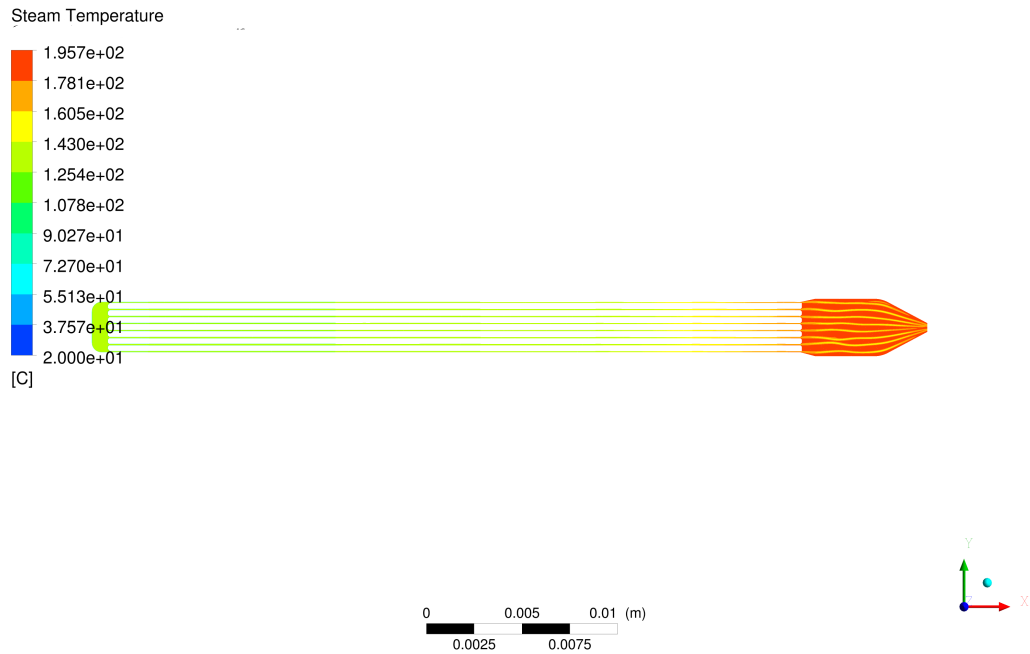


Figure 8.3: Steam temperature distribution into thruster.

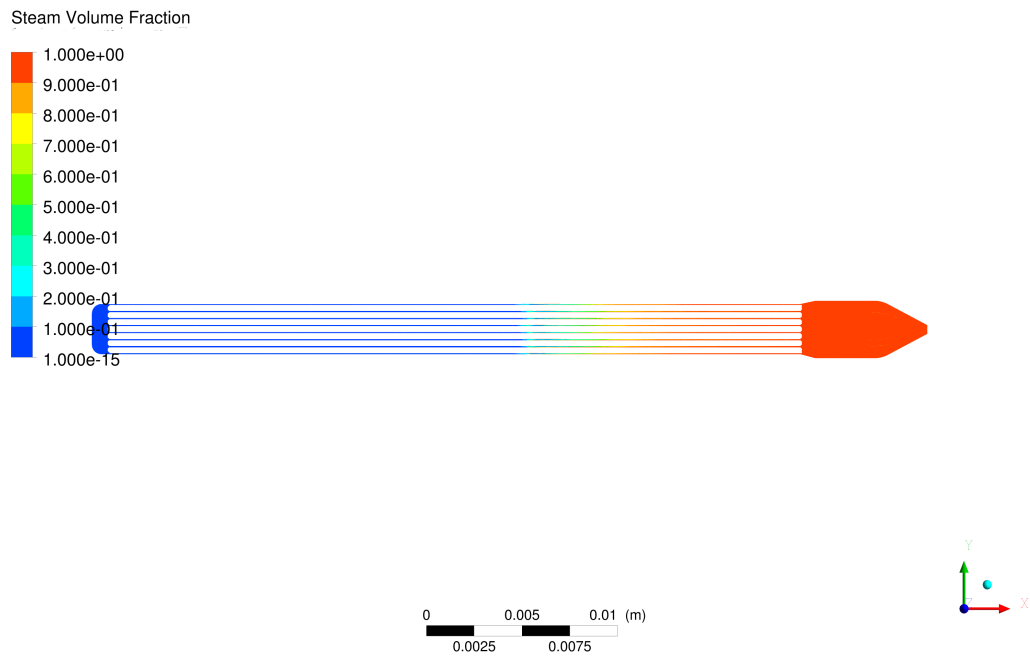


Figure 8.4: Steam volume fraction into thruster.

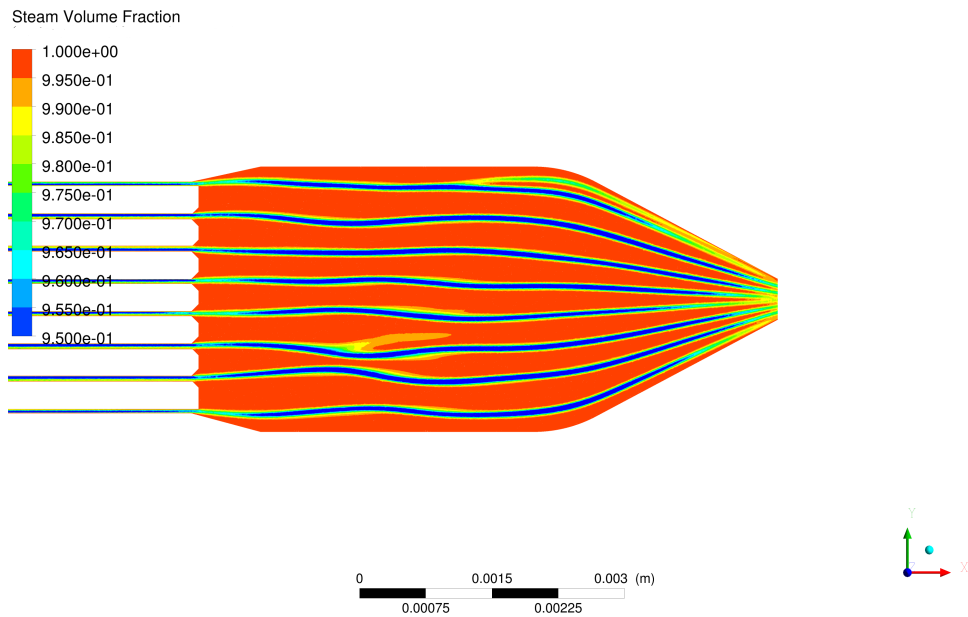


Figure 8.5: Steam volume fraction, into chamber region.

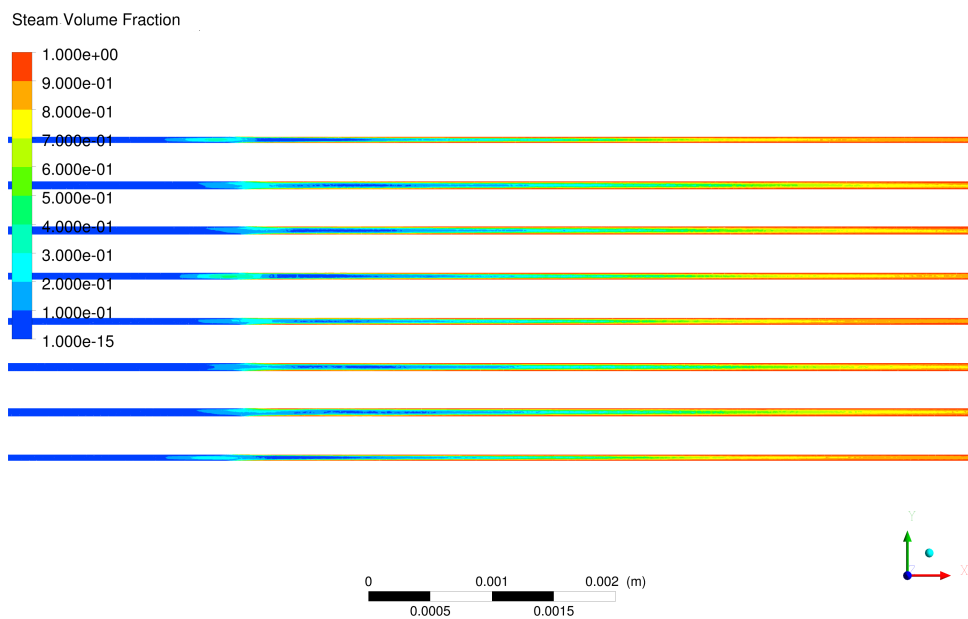


Figure 8.6: Steam volume fraction Zoom in, into the middle of microchannel region.

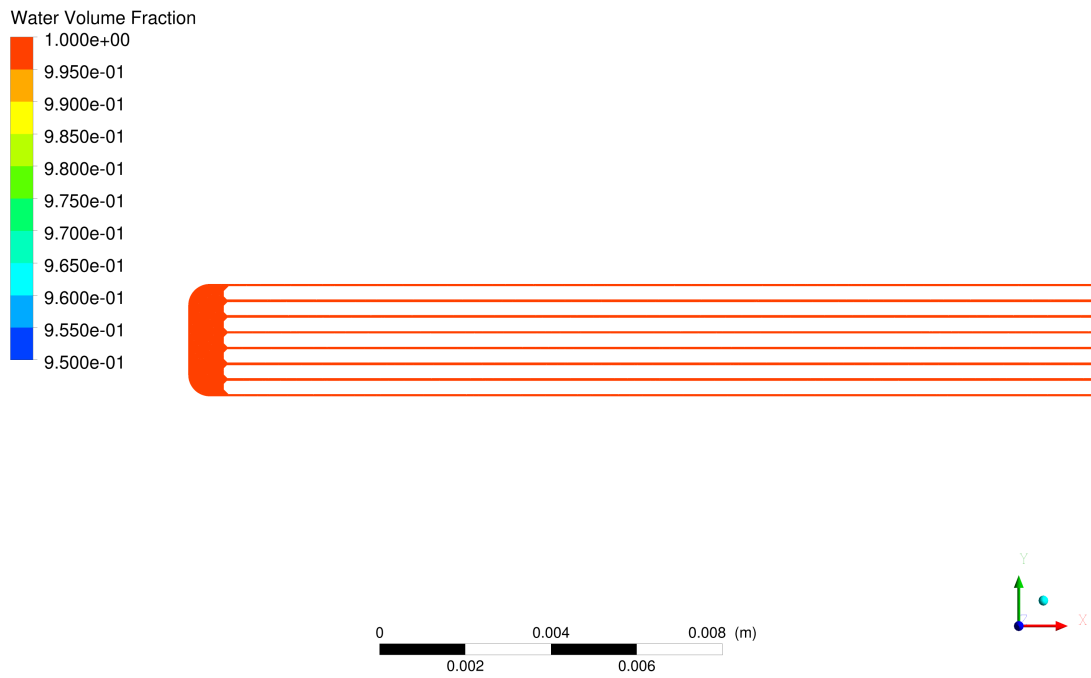


Figure 8.7: Water volume fraction distribution into thruster.

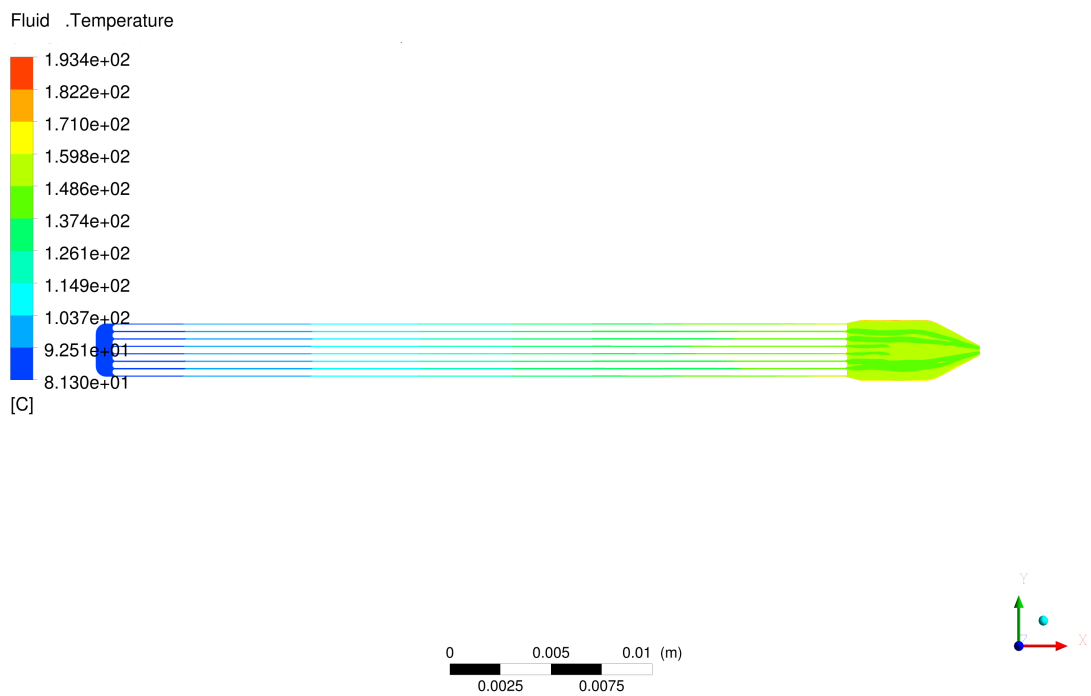


Figure 8.8: Water temperature distribution into thruster.

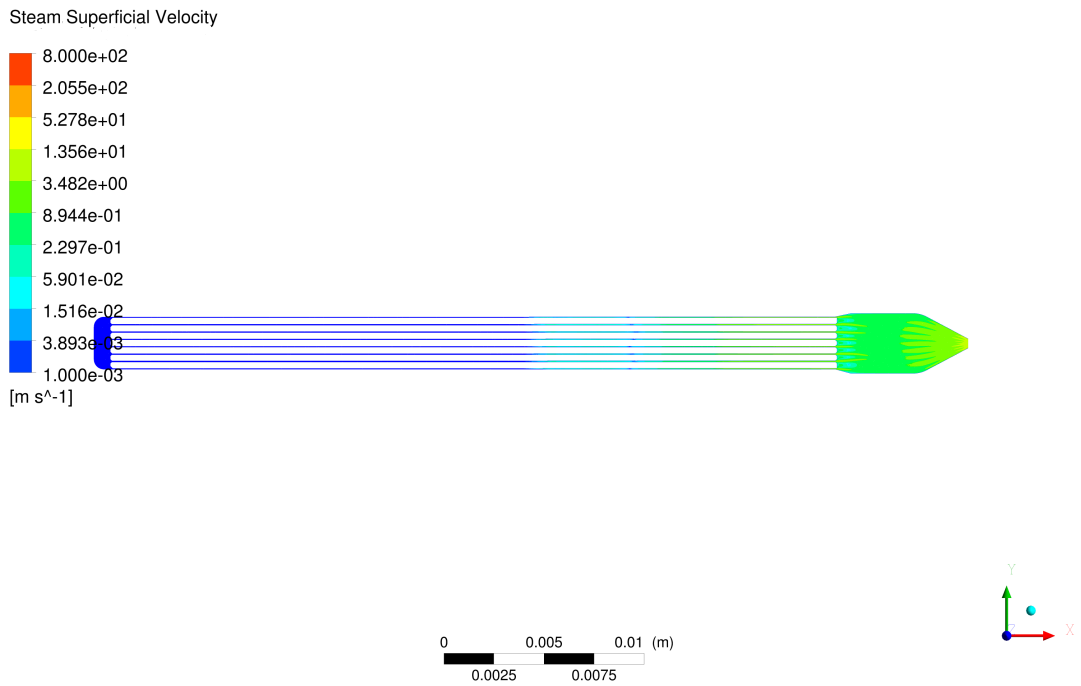


Figure 8.9: Steam velocity distribution into thruster.

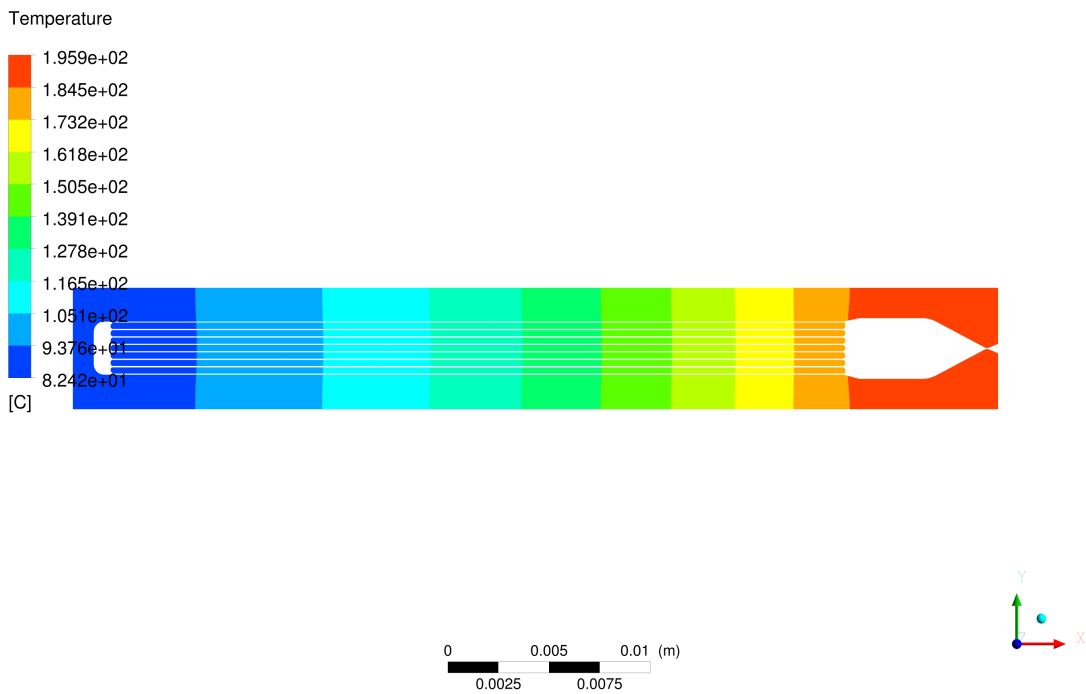


Figure 8.10: Silicon temperature distribution into thruster.

Table 8.2: Numerical data of the VLM subsonic model simulation at heat power 3.6 W.

Location	Modle inlet	Microchannels inlet	Microchannels cross-section average plane	microchannels outlet	Model outlet
Steam bulk temperature, (K)	408	495	563	721	743
Water bulk temperature, (K)	294	371	409	462	523
Velocity, ($m.s^{-1}$)	0.3	2.2	7.5	16	26
Static Pressure, (Pa)	252500	252421	242889	219541	218007
Total Pressure, (Pa)	252502	252511	242889	220590	218883
Density, ($kg.m^{-3}$)	325	20	4.0	2.4	1.7
Steam volume fraction	0.676	0.980	0.997	0.998	0.999

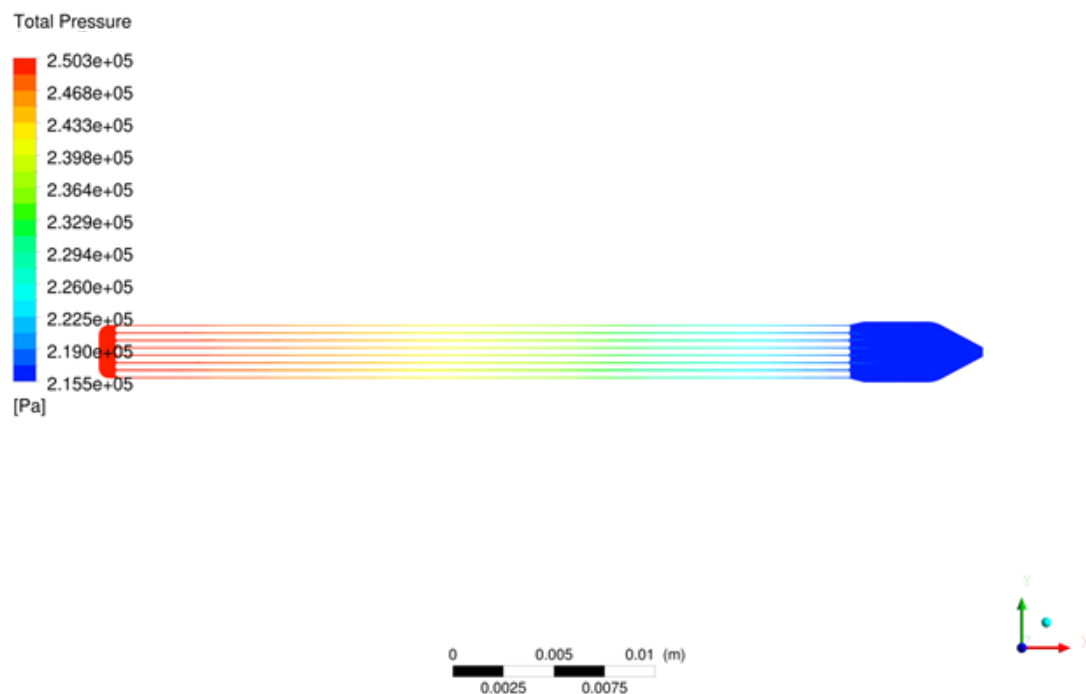


Figure 8.11: Total pressure distribution into thruster.

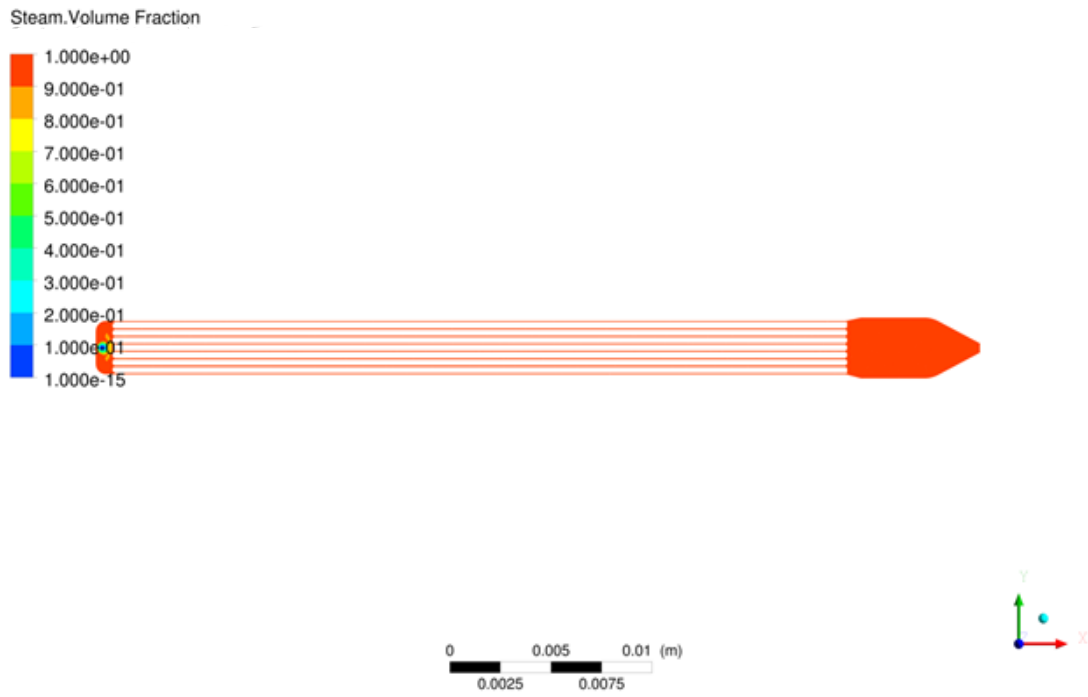


Figure 8.12: Steam volume fraction into thruster.

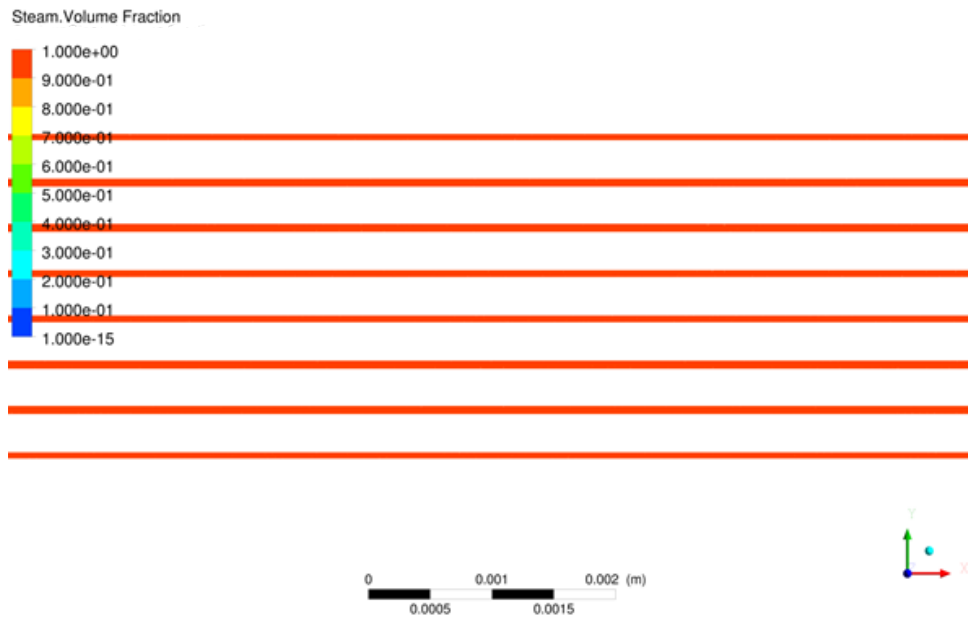


Figure 8.13: Zoon in of Steam volume fraction into middle of microchannels region.

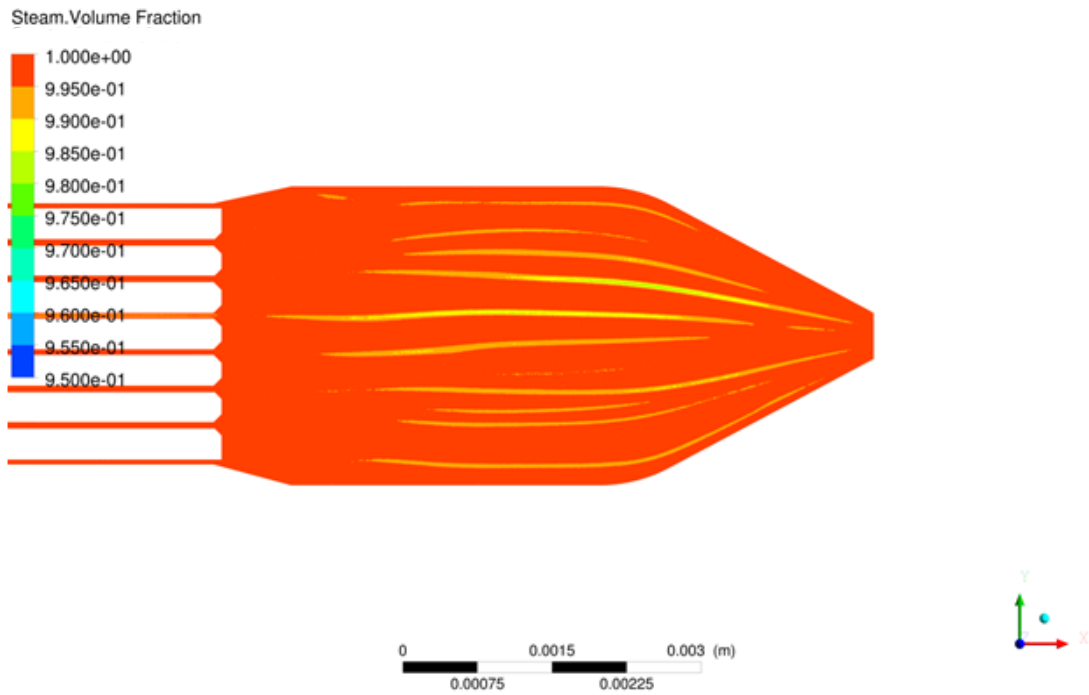


Figure 8.14: Steam volume fraction into the chamber region.

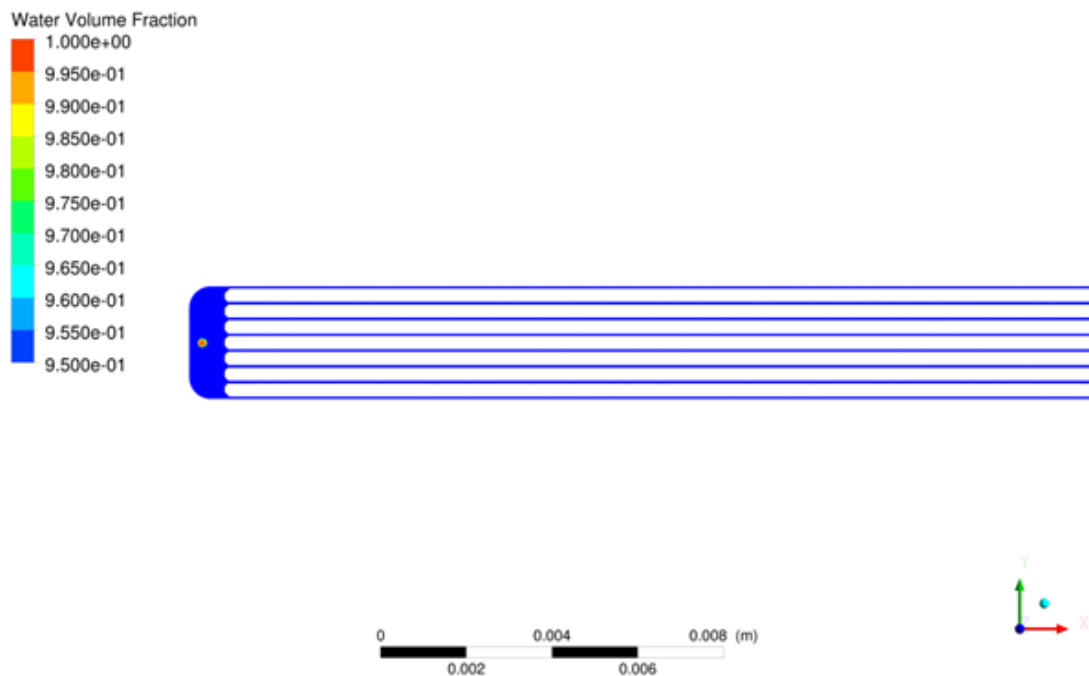


Figure 8.15: Water volume fraction distribution into the thruster.

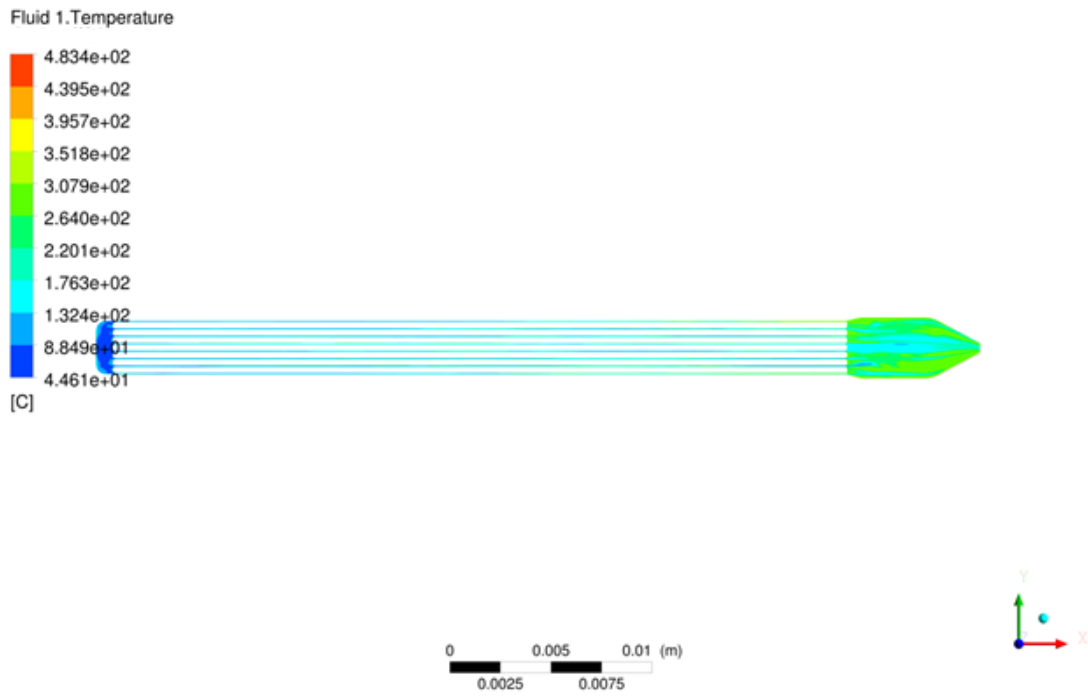


Figure 8.16: Water temperature distribution into thruster.

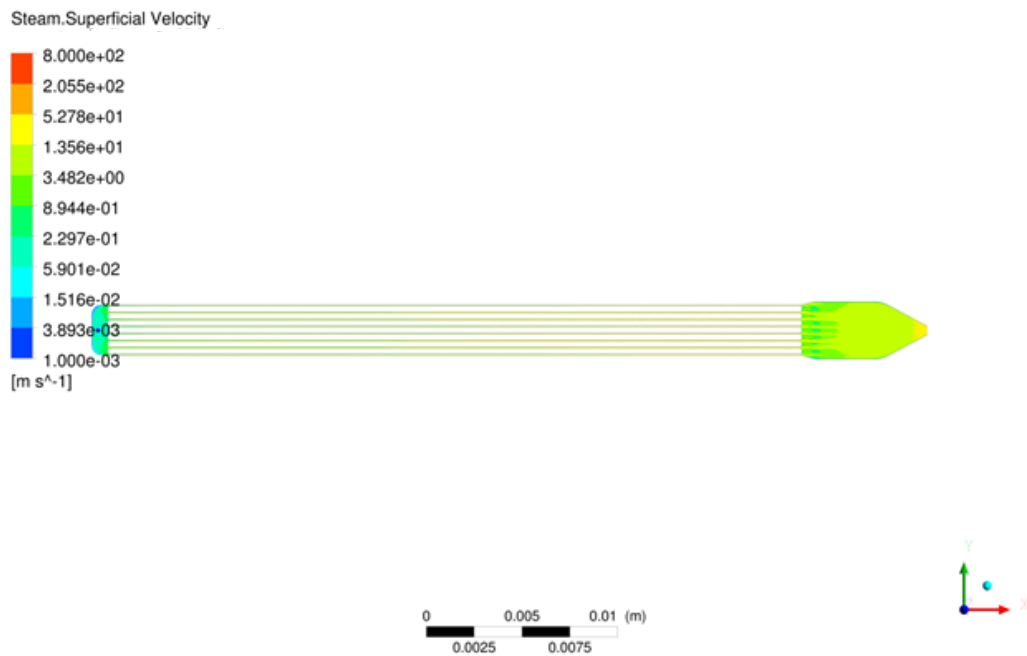


Figure 8.17: Steam velocity distribution into thruster.

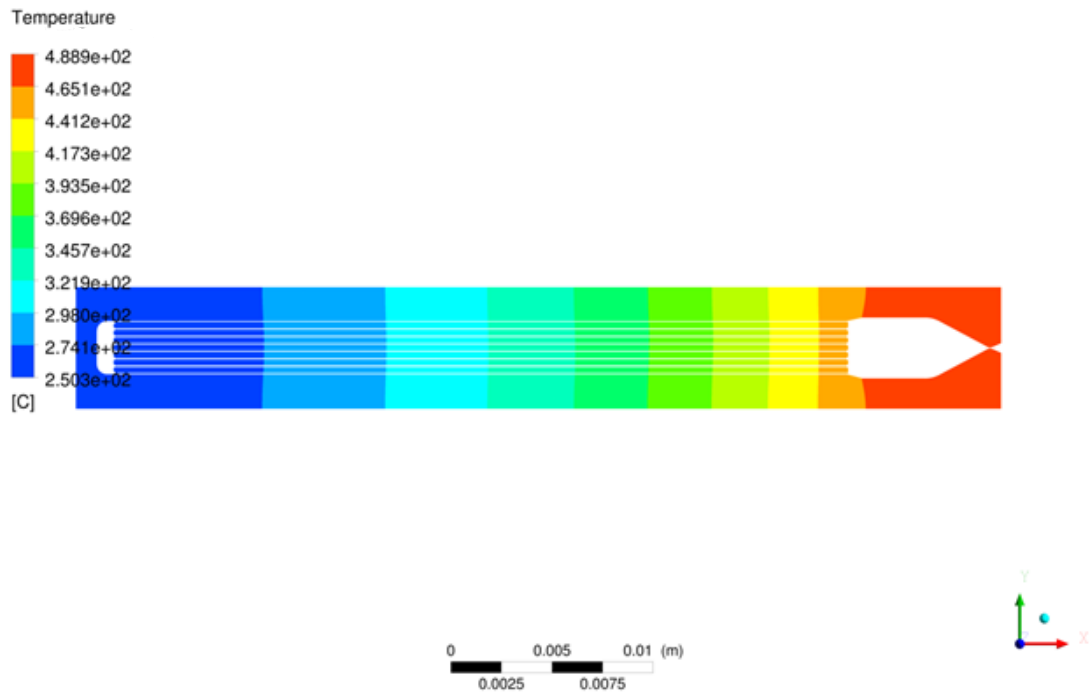


Figure 8.18: Silicon temperature distribution into thruster.